ANL-77-10

LIGHT-WATER-REACTOR SAFETY RESEARCH PROGRAM: QUARTERLY PROGRESS REPORT

October—December 1976

UofC·AUA·USERDA

ARGONNE NATIONAL LABORATORY, ARGONNE, ILLINOIS

Prepared for the U. S. NUCLEAR REGULATORY COMMISSION
Office of Nuclear Regulatory Research

Distribution Categories:
Water Reactor Safety Research—
Fuel Behavior (NRC-3)
Water Reactor Safety Research—
Analysis Development (NRC-4)

ANL-77-10

ARGONNE NATIONAL LABORATORY
9700 South Cass Avenue
Argonne, Illinois 60439

LIGHT-WATER-REACTOR SAFETY RESEARCH PROGRAM: QUARTERLY PROGRESS REPORT

October–December 1976

Robert G. Sachs, Laboratory Director
Jack A. Kyger, Associate Laboratory Director

March 1977

Previous reports in this series:

ANL-76-15	October–December 1975
ANL-76-49	January–March 1976
ANL-76-87	April–June 1976
ANL-76-121	July–September 1976

TABLE OF CONTENTS

Page

ABSTRACT xii

I. LOSS-OF-COOLANT ACCIDENT RESEARCH: HEAT TRANSFER AND FLUID DYNAMICS. 1

A. Transient Critical Heat Flux. 1

1. Installation of Test Section II 1
2. Single-phase Heat-transfer Results 3
3. Steady-state CHF Results. 6
4. Transient CHF Results 8

B. Nitrogen-Water Blowdown Tests 35

C. One-dimensional Drift-flux Modeling: One-dimensional Drift Velocity of Bubbly, Droplet, Annular, and Annular Mist Flows in Confined Channel 38

1. One-dimensional Drift-flux Model 38
2. Dispersed Two-phase Flow. 41
3. Annular Two-phase Flow 53
4. Annular-mist Flow 55
5. Conclusions 58

References 59

II. TRANSIENT FUEL RESPONSE AND FISSION-PRODUCT RELEASE PROGRAM 63

A. Modeling of Fuel-Fission-product Behavior 64

1. Development of Volatile-fission-product Behavior Code . . . 64
2. Transient Fission-gas Release 67
3. Steady-state Sensitivity Analyses. 68
4. FRAP-GRASS Development. 71

B. Experimental Program. 71

1. Transient Heating Tests. 72
2. DEH/PBF Cross-check 74

References 76

III. MECHANICAL PROPERTIES OF ZIRCALOY CONTAINING OXYGEN. 77

A. Summary 77

TABLE OF CONTENTS

Page

B. Effect of Microstructure and Oxygen Concentration on the Uniaxial Tensile Properties of Zircaloy-4 78

1. Scanning-electron-microscopy Investigation of As-received Zircaloy-4 Specimens Deformed at 850°C 78
2. Effect of Cooling Rate through the $\beta \rightarrow \alpha'$ Transformation on the Tensile Properties of As-received Zircaloy-4 79
3. Effect of Oxygen Concentration and Cooling Rate through the $\beta \rightarrow \alpha'$ Transformation on the Tensile Properties of Zircaloy 82

C. Biaxial Deformation and Rupture Characteristics of Zircaloy-4 Cladding in Steam 85

1. Rupture Characteristics of Axially Constrained Cladding at a Heating Rate of 55°C/s 85
2. Rupture Characteristics of Unconstrained Cladding at a Heating Rate of 115°C/s 86
3. Microstructural Evaluation of Localized Thinning of the Cladding Wall after Ballooning Deformation in Steam at High Temperatures 88

D. Kinetics of the $\beta \rightarrow \alpha'$ Phase Transformation in Zircaloy-4. . . . 94

1. Transformation Kinetics of Zircaloy-4 94
2. Correlation of Cooling Rate with the Microstructure of Transformed α' Phase 96

References 101

IV. STEAM-EXPLOSION STUDIES 102

A. Vapor Explosions at Elevated Temperatures 102

B. Combined Physical-Chemical Explosions 104

References 106

LIST OF FIGURES

No.	Title	Page
I.1.	Power profile for Test Section II	1
I.2.	Overall View of Test Section II	1
I.3.	Lower-end View of Test Section II	2
I.4.	Upper-end View of Test Section II	2
I.5.	Heat-loss Results for Test Section II	3
I.6.	Heat-balance Results for Test Section II	4
I.7.	Single-phase Heat-transfer Results for Test Section II	5
I.8.	Wall-temperature Behavior during Steady-state CHF	6
I.9.	Equivalent Water Pressure for Freon-11 at Equal Orthobaric-density Ratio	7
I.10.	Mass-velocity Scaling Factor	7
I.11.	Comparison between Measured CHF and Bowring's Scaled CHF Prediction	8
I.12.	Comparison between Purcupile's CHF Data and Bowring's Scaled CHF Prediction	9
I.13.	Steady-state Wall-temperature Profile in Test DB-107	10
I.14.	Steady-state Wall-temperature Profile in Test DB-108	10
I.15.	Steady-state Wall-temperature Profile in Test DB-111	11
I.16.	Steady-state Wall-temperature Profile in Test DB-112	11
I.17.	System Pressure during Test DB-107	12
I.18.	Differential Pressure across Test Section during Test DB-107	13
I.19.	Differential Pressure across Break Orifice during Test DB-107	13
I.20.	Turbine-flowmeter Measurement during Test DB-107	14
I.21.	Fluid Temperature during Test DB-107	14
I.22.	Wall-thermocouple Measurement during Test DB-107	15
I.23.	System Pressure during Test DB-108	17
I.24.	Differential Pressure across Test Section during Test DB-108	17
I.25.	Differential Pressure across Break Orifice during Test DB-108	18
I.26.	Turbine-flowmeter Measurement during Test DB-108	18
I.27.	Fluid Temperature during Test DB-108	19

LIST OF FIGURES

No. Title Page

I.28. Wall-thermocouple Measurement during Test DB-108. 19

I.29. System Pressure during Test DB-111 21

I.30. Differential Pressure across Break Orifice during Test DB-111. 22

I.31. Turbine-flowmeter Measurement during Test DB-111. 22

I.32. Fluid Temperature during Test DB-111 23

I.33. Wall-thermocouple Measurement during Test DB-111. 23

I.34. System Pressure during Test DB-112 25

I.35. Differential Pressure across Break Orifice during Test DB-112. 26

I.36. Turbine-flowmeter Measurement during Test DB-112. 26

I.37. Fluid Temperature during Test DB-112 27

I.38. Wall-thermocouple Measurement during Test DB-112. 27

I.39. System Saturation Temperature during Test DB-107. 31

I.40. System Saturation Temperature during Test DB-108. 32

I.41. System Saturation Temperature during Test DB-111. 33

I.42. System Saturation Temperature during Test DB-112. 33

I.43. Comparison of Measured and Calculated Vessel Pressures during Blowdown Test of Nitrogen-Water System. 35

I.44. Experimental Data for High-pressure System from Hughes 43

I.45. Freon-22 Data in Boiling Flow, from Zuber et al. 43

I.46. Fully Developed Nitrogen-NaK Flow Data, from Thome. 43

I.47. Fully Developed Air-Water Flow Data, from Smissaert. 43

I.48. Fully Developed Nitrogen-Mercury Flow Data, from Smissaert . 44

I.49. Experimental Data for Cocurrent Upflow and Cocurrent Downflow of Steam-Water System, from Petrick. 44

I.50. Experimental Data for Cocurrent Upflow and Cocurrent Downflow of Heated Santowax-R System, from Bergonzoli and Halfen. . 44

I.51. Limiting Value of Distribution Parameter C_0 at Zero Void Fraction and $\rho_g/\rho_f \rightarrow 0$ Based on Single-phase Turbulent-flow Profile, from Nikuradse 45

I.52. Distribution Parameter for Fully Developed Flow in Round Tube 46

LIST OF FIGURES

No. Title Page

I.53. Distribution Parameter for Fully Developed Flow in Rectangular Channel 46

I.54. Axial Void Distribution with Corresponding Void Profiles at Various Stations for Steam-Water Experiment in Rectangular Channel, from St. Pierre 48

I.55. Axial Void Distribution with Corresponding Void Profiles at Various Stations for Freon-22 Experiment in Round Tube, from Zuber et al 48

I.56. Experimental Data of Rouhani and Becker in Round Tube and Effect of Developing Flow due to Boiling. 49

I.57. Experimental Data of St. Pierre in Rectangular Flow and Effect of Developing Flow due to Boiling. 49

I.58. Experimental Data of Marchaterre in Rectangular Duct and Effect of Developing Flow due to Boiling. 49

I.59. Distribution Parameter in Developing Flow due to Boiling 50

I.60. Comparison of Annular-flow Correlation to Experimental Data. 54

II.1. SST-GRASS-calculated Fractional Fission-gas Release vs Burnup for an Irradiation at 7 kW/ft 69

II.2. SST-GRASS-calculated Fractional Fission-gas Release vs Burnup for an Irradiation at 7 kW/ft with Power Cycling 71

III.1. Slip Lines on the Surface of a Zircaloy-4 Specimen Deformed at 850°C, $\dot{\epsilon} = 3.3 \times 10^{-1}\ s^{-1}$ 78

III.2. Facets due to Thermal Etching of the Surface of a Zircaloy-4 Specimen Deformed at 850°C, $\dot{\epsilon} = 3.3 \times 10^{-6}\ s^{-1}$ 79

III.3. Temperature-Time Curve for a Resistance-heated Zircaloy-4 Tube Cooled from 1030°C in Water 80

III.4. Effect of Cooling Rate on the Yield Stress of Transformed β-phase Zircaloy-4 at Several Temperatures 80

III.5. Influence of Cooling Rate on the UTS of Transformed β-phase Zircaloy-4 at Several Temperatures 81

III.6. Cooling-rate Dependence of Uniform Strain of Transformed β-phase Zircaloy-4 at Several Temperatures 81

III.7. Total Strain as a Function of Cooling Rate for Transformed β-phase Zircaloy-4 at Several Temperatures 82

LIST OF FIGURES

No.	Title	Page
III.8.	Uniform Strain vs Temperature for Transformed β-phase Zircaloy-4 at Various Cooling Rates	83
III.9.	Total Strain as a Function of Temperature for Transformed β-phase Zircaloy-4 at Various Cooling Rates	83
III.10.	Dependence of Yield Stress and UTS on Cooling Rate for Composite Zircaloy-4 Specimens with 4.0 wt % Oxygen	84
III.11.	Uniform and Total Strain as a Function of Cooling Rate for Composite Zircaloy-4 Specimens with 4.0 wt % Oxygen	84
III.12.	Effect of Cooling Rate on the Yield Stress and UTS of Composite Zircaloy-4 Specimens with 4.4 wt % Oxygen	85
III.13.	Influence of Cooling Rate on the Uniform and Total Strains of Composite Zircaloy-4 Specimens with 4.4 wt % Oxygen	85
III.14.	Maximum Circumferential Strain vs Burst Temperature for Axially Constrained Zircaloy-4 Cladding at a Heating Rate of 55°C/s in Steam and Vacuum Environments	86
III.15.	Maximum Rupture Circumferential Strain as a Function of Initial Internal Pressure for Axially Constrained Zircaloy-4 Cladding in Steam and Vacuum Environments at a Heating Rate of 55°C/s	86
III.16.	Maximum Rupture Circumferential Strain as a Function of Initial Internal Pressure for Axially Constrained Zircaloy-4 Cladding in Steam and Vacuum Environments at a Heating Rate of 115°C/s	87
III.17.	Effect of Initial Internal Pressure and Heating Rate on the Maximum Circumferential Strain for Axially Constrained Zircaloy-4 Cladding Burst In Vacuo.	87
III.18.	Effect of Initial Internal Pressure and Heating Rate on the Maximum Circumferential Strain for Axially Constrained Zircaloy-4 Cladding Burst in a Steam Environment	87
III.19.	Maximum Circumferential Strain vs Burst Temperature for Axially Constrained and Unconstrained Cladding at a Heating Rate of 115°C/s in a Steam Environment.	87
III.20.	Burst Temperature as a Function of Initial Internal Pressure for Axially Constrained Zircaloy-4 Cladding in Steam and Vacuum and for Axially Unconstrained Cladding in Steam at a Heating Rate of 115°C/s	88

LIST OF FIGURES

No.	Title	Page
III.34.	Intermediate Martensitic/Basketweave Structure of As-received Zircaloy-4 after Cooling through the $\beta \rightarrow \alpha'$ Transformation at ~1000°C/s from 1000°C	98
III.35.	Basketweave Structure of As-received Zircaloy-4 after Cooling through the $\beta \rightarrow \alpha'$ Transformation at ~500°C/s from 1000°C	98
III.36.	Intermediate Basketweave/Parallel-plate Structure of As-received Zircaloy-4 after Cooling through the $\beta \rightarrow \alpha'$ Transformation at 3.3°C/s from 1000°C	99
III.37.	Parallel-plate Structure of As-received Zircaloy-4 after Cooling through the $\beta \rightarrow \alpha'$ Transformation at 1.8°C/s from 1250°C	99
III.38.	Microstructure of As-received Zircaloy-4 after Cooling through $\beta \rightarrow \alpha'$ Transformation at 0.1°C/s from 1000°C	99
III.39.	Rim-α Structure at the Previous β-grain Boundaries of As-received Zircaloy-4 Formed during Cooling through the $\beta \rightarrow \alpha'$ Transformation	100
III.40.	Micrographs of Zircaloy-4/Oxygen Alloys with 0.446 and 1.15 wt % Oxygen after Cooling through the $\beta \rightarrow \alpha'$ Transformation That Illustrate the Martensitic and Parallel-plate Microstructures, Respectively	100
IV.1.	Large-scale Vapor Explosions in a Contained Volume	103
IV.2.	High-temperature Experimental Data on Freon-22 and Mineral Oil	104

LIST OF TABLES

No.	Title	Page
I.1.	Steady-state Critical-heat-flux Data	5
I.2.	Steady-state Test Conditions in Test Section II	9
I.3.	Equivalent Water Conditions during Steady-state Conditions	9
I.4.	Other Parameters during Blowdown	12
II.1.	Summary of DEH Transient Tests Run to Date Using Robinson Fuel and Tests Originally Anticipated in the Initial Plan	72
III.1.	Correlation of Cooling Rate with the $\beta \rightarrow \alpha'$ Transformation Structure of Zircaloy-4	97

ABSTRACT

This progress report summarizes the Argonne National Laboratory work performed during October, November, and December 1976 on water-reactor-safety problems. The following research and development areas are covered: (1) Loss-of-coolant Accident Research: Heat Transfer and Fluid Dynamics; (2) Transient Fuel Response and Fission-product Release Program; (3) Mechanical Properties of Zircaloy Containing Oxygen; and (4) Steam-explosion Studies.

I. LOSS-OF-COOLANT ACCIDENT RESEARCH: HEAT TRANSFER AND FLUID DYNAMICS

Responsible Section Managers:
M. A. Grolmes,* R. E. Henry, and P. A. Lottes, RAS

A. Transient Critical Heat Flux (J. C. Leung and R. E. Henry, RAS)

1. Installation of Test Section II

Test Section II has an axial nonuniform but symmetric heat-flux profile as shown in Fig. I.1. Photographs of the section before installation in the rig are shown in Figs. I.2-I.4. To prevent significant heat loss, the test section was covered with 0.2-cm-thick asbestos and 1.3 cm of fiberglass insulation.

Besides a longer heated section, an upper plenum was installed immediately above the exit turbine flowmeter. This plenum was made from a

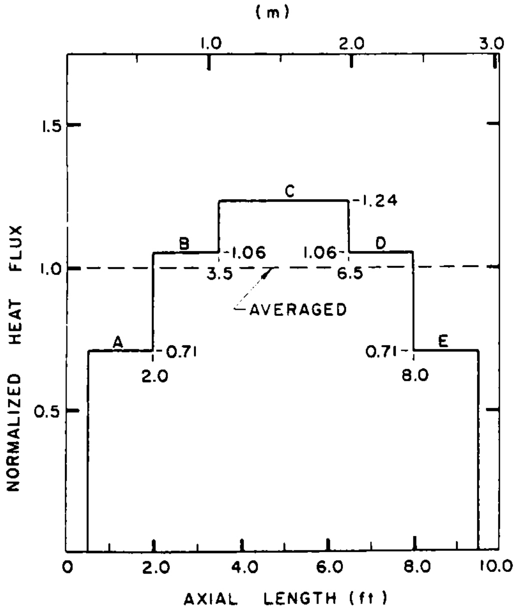

Fig. I.1

Power Profile for Test Section II. ANL Neg. No. 900-77-149.

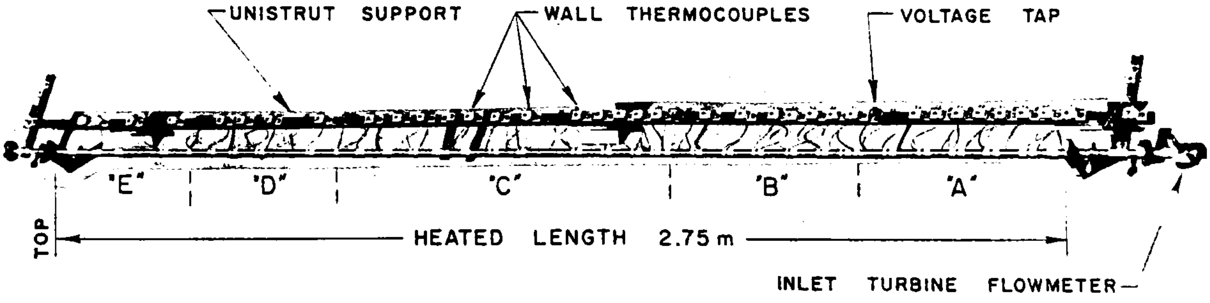
UNISTRUT SUPPORT
WALL THERMOCOUPLES
VOLTAGE TAP
"E"
"D"
"C"
"B"
"A"
TOP
HEATED LENGTH 2.75 m
INLET TURBINE FLOWMETER

Fig. I.2. Overall View of Test Section II. ANL Neg. No. 900-77-135.

---

*Now in the Office of the Director.

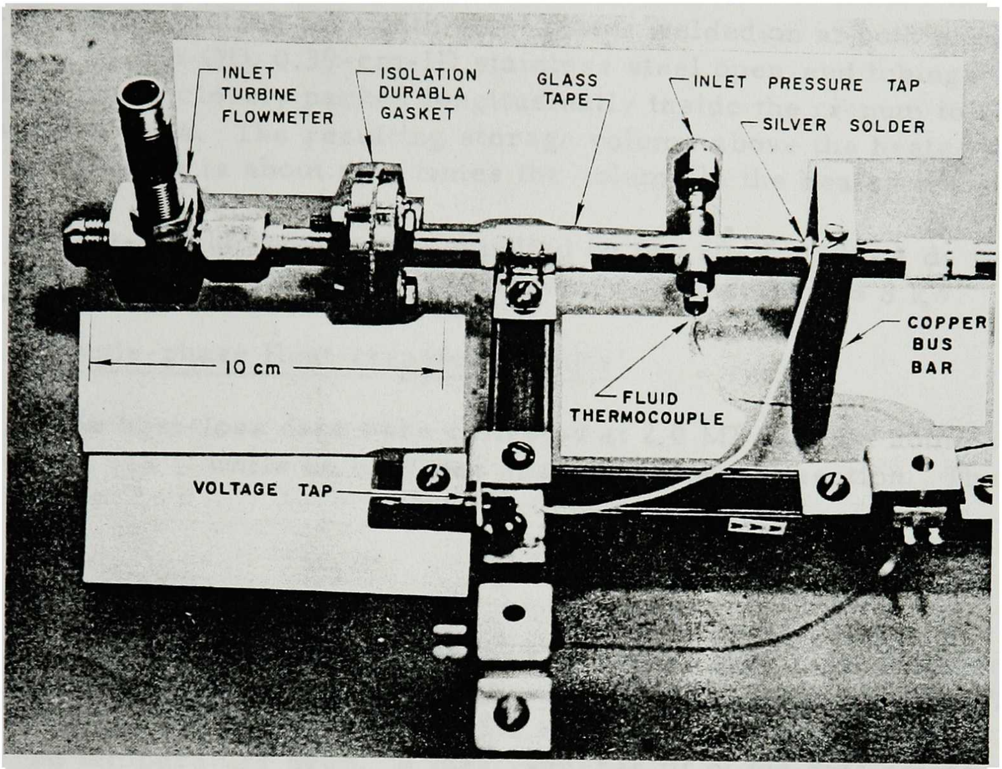
INLET TURBINE FLOWMETER
ISOLATION DURABLA GASKET
GLASS TAPE
INLET PRESSURE TAP
SILVER SOLDER
COPPER BUS BAR
10 cm
FLUID THERMOCOUPLE
VOLTAGE TAP

Fig. I.3. Lower-end View of Test Section II. ANL Neg. No. 900-77-134.

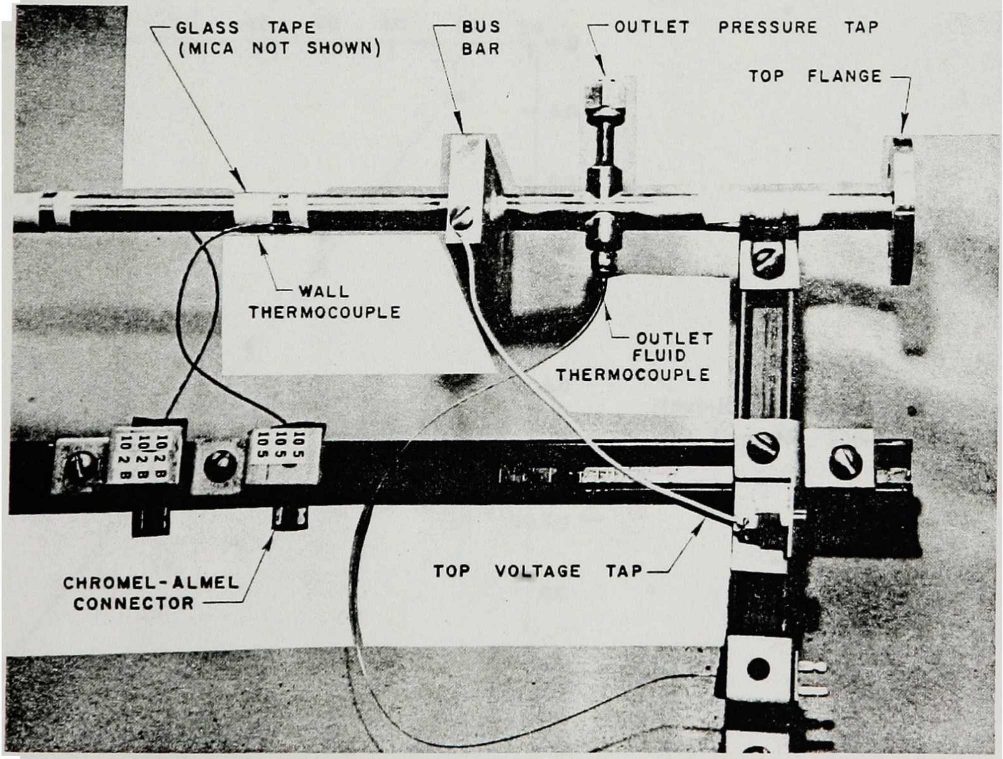
GLASS TAPE (MICA NOT SHOWN)
BUS BAR
OUTLET PRESSURE TAP
TOP FLANGE
WALL THERMOCOUPLE
OUTLET FLUID THERMOCOUPLE
102B
105
CHROMEL-ALMEL CONNECTOR
TOP VOLTAGE TAP

Fig. I.4. Upper-end View of Test Section II. ANL Neg. No. 900-77-133.

11.4-cm-ID, 30.5-cm-long tube with steel plates welded on at both ends. A total of 500 0.44-cm-OD, 0.39-cm-ID stainless steel open-end tubings, each 25.4 cm long, were closely packed longitudinally inside the plenum to provide greater surface area. The resulting storage volume above the heated zone was 2620 cm^3, which is about nine times the volume in the heated channel.

Test-section power was supplied by two 20-V, 1500-A dc rectifiers in series. The maximum output in the present test section was 8 kW.

2. Single-phase Heat-transfer Results

The heat-loss data were collected at 2.0 MPa with a nominal inlet temperature of 118°C while no heat was applied to the test section. The heat-loss equation is

$$q_L = W_f C_p \Delta t, \tag{1}$$

where q_L, W_f, C_p, and Δt are the heat loss, the mass flow rate, the specific heat, and the temperature drop across the test section, respectively. The results are shown in Fig. I.5 as a plot of the reciprocal of mass flow rate versus the measured temperature drop. A least-squares fit of the data points yields an average heat loss of 185 W. In most instances, this is less than 5% of the applied power input.

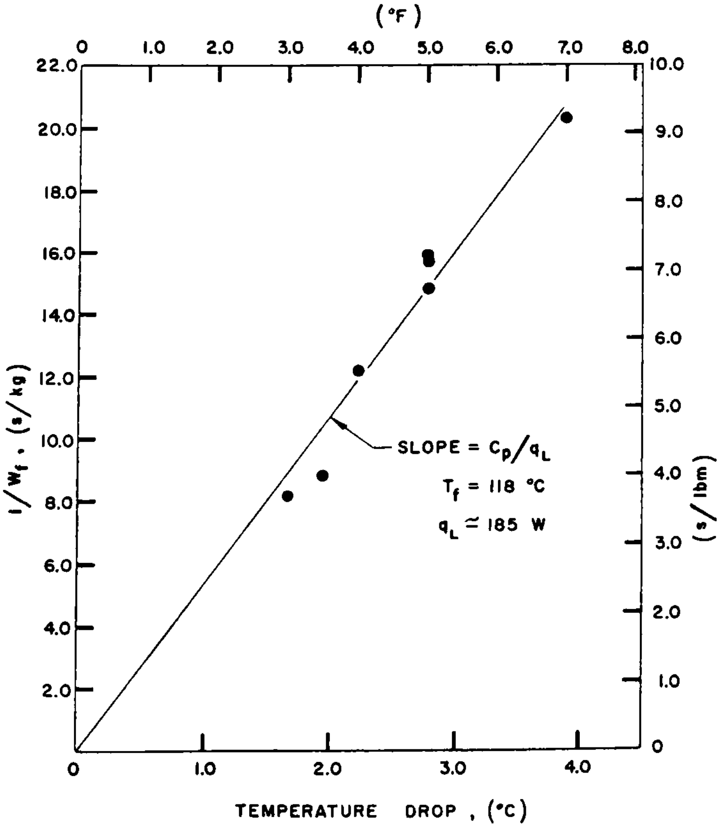

Fig. I.5

Heat-loss Results for Test Section II. ANL Neg. No. 900-77-145.

Single-phase heat-balance results are shown in Fig. I.6. The calculated heat input was based on the measured values of mass flow rate and temperature rise; the test-section power was calculated by the product of measured voltage drop and current. The agreement between these two values is well within 5%.

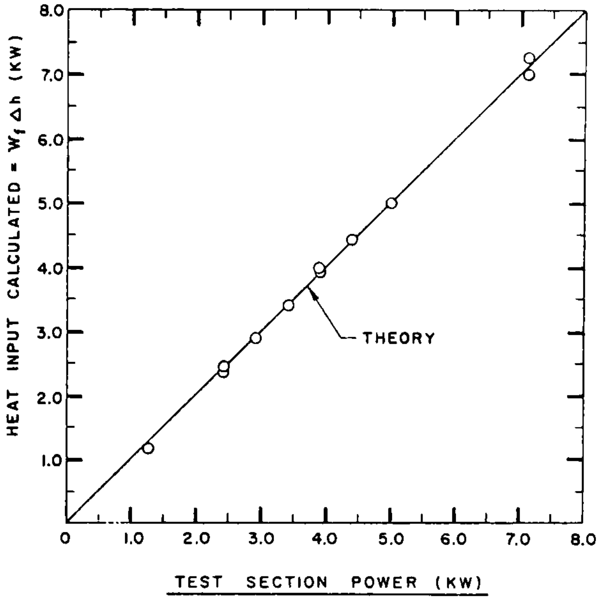

Fig. I.6

Heat-balance Results for Test Section II. ANL Neg. No. 900-76-1000.

Single-phase heat-transfer correlation is commonly given in dimensionless form as represented by the Dittus-Boelter equation. For large temperature variation near the heated wall, as in the present case, the Sieder-Tate correlation is recommended:

$$Nu = 0.023Re^{0.8}Pr^{0.4}\left(\frac{\mu}{\mu_w}\right)^{0.14}, \tag{2}$$

where Nu, Re, Pr, and μ are the conventional Nusselt number, Reynolds number, Prandtl number, and viscosity, respectively. Here the physical properties are evaluated at the fluid bulk temperature, except for μ_w, which is evaluated at the wall. The transport properties of Freon-11 were taken from the ASHRAE publication[1] and were found to be in good agreement with the Russian data.[2] The results shown in Fig. I.7 exhibited satisfactory agreement with the Sieder-Tate correlation.

3. Steady-state CHF Results

Twelve vertical-upflow steady-state critical-heat-flux (CHF) data points were obtained over the following ranges:

Pressure	1.5-2.0 MPa
Mass velocity	570-1200 $kg/m^2 \cdot s$

Inlet quality	-0.4 to -0.07
Average heat flux	59.0-80.0 kW/m^2

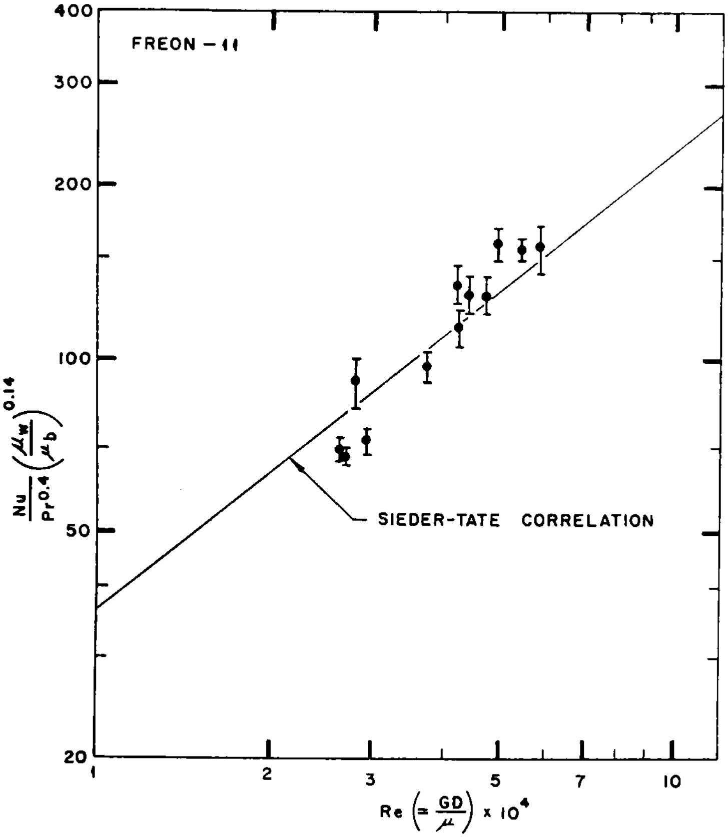

Fig. I.7

Single-phase Heat-transfer Results for Test Section II. ANL Neg. No. 900-77-141.

The results of these runs are tabulated in Table I.1. The applied heat flux was not high enough to cause CHF in the highest heat-flux zone, and the dryout location was always observed at the exit of the test section. An example of the dryout is indicated by the temperature excursion shown in Fig. I.8. Small oscillation in wall temperature was sometimes observed before

TABLE I.1. Steady-state Critical-heat-flux Data

Run	Pressure, MPa	Mass Velocity, kg/m^2 · s	Quality		Total Power, kW	Average Heat Flux, kW/m^2	Predicted CHF,[a] kW/m^2
			Inlet	Exit			
12.13.9	2.08	687.6	-0.388	0.470	7.12	70.2	66.6
12.14.1	1.78	820.6	-0.219	0.458	7.22	70.9	70.4
12.14.2	1.72	843.6	-0.203	0.462	7.36	72.5	71.9
12.14.3	1.61	907.4	-0.160	0.465	7.64	75.3	75.1
12.14.4	1.54	941.3	-0.135	0.458	7.64	75.3	76.7
12.16.1	1.62	590.0	-0.145	0.617	6.00	59.2	61.2
12.16.2	1.62	575.1	-0.135	0.642	6.00	59.2	60.3
12.16.3	1.57	832.8	-0.106	0.514	7.05	69.4	70.4
12.16.4	1.63	942.6	-0.121	0.462	7.41	73.0	72.6
12.16.5	1.58	980.6	-0.106	0.449	7.41	73.0	73.5
12.16.6	1.48	1013.2	-0.073	0.453	7.41	73.0	75.1
12.16.7	1.54	1201.7	-0.082	0.402	8.05	79.3	77.6

[a] Bowring's correlation with Ahmad scaling.

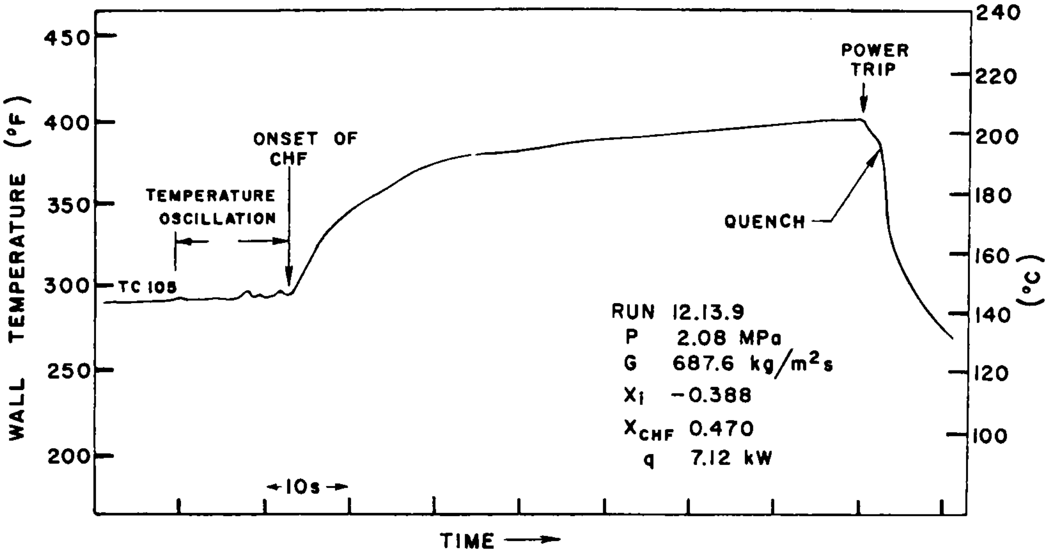

Fig. I.8. Wall-temperature Behavior during Steady-state CHF. ANL Neg. No. 900-77-143.

the onset of stable dryout, an observation previously reported by Groeneveld.[3] The results were compared with the Bowring's[4] water CHF correlation scaled to Freon-11 using Ahmad's modeling.[5] This comparison has given good results in Freon-113.[6] Bowring's correlation was developed from upflow in round tube data with uniform heat flux and has the equivalent forms of representation

$$\varphi_{CHF} = \frac{A - Bh_{fg}x}{C} \tag{3}$$

and

$$\varphi_{CHF} = \frac{A + B\Delta h_i}{C + L}, \tag{4}$$

where

φ_{CHF} = critical heat flux,

A, C = function (P, D, G),

$B = \frac{GD}{4}$,

h_{fg} = latent heat of vaporization,

Δh_i = inlet subcooling,

x = dryout quality,

G = mass velocity,

D = tube diameter,

and

L = heated length.

These two forms are related through the heat-balance equation

$$\frac{4\varphi L}{GD} = \Delta h_i + x h_{fg}. \tag{5}$$

To use the correlation in the nonuniform heat-flux case, dryout is assumed to occur at identical enthalpies or qualities,[7] the so-called "local-conditions hypothesis."[8]

In Ahmad's model, the pressure is scaled via the density ratio as shown in Fig. I.9. According to this model, the mass-velocity scaling factor K turned out to be about 0.78 over a wide pressure range. The same scaling factor proposed by Dix[9] is also shown in Fig. I.10, but it involves the ratio of the surface-tension terms, which have uncertainty in their values. If we further require the same inlet quality (i.e., $-\Delta h_i/h_{fg}$), the scaled CHF is given by

$$\varphi_F = \varphi_W \frac{(Gh_{fg})_F}{(Gh_{fg})_W} = \varphi_W K \frac{(h_{fg})_F}{(h_{fg})_W}, \tag{6}$$

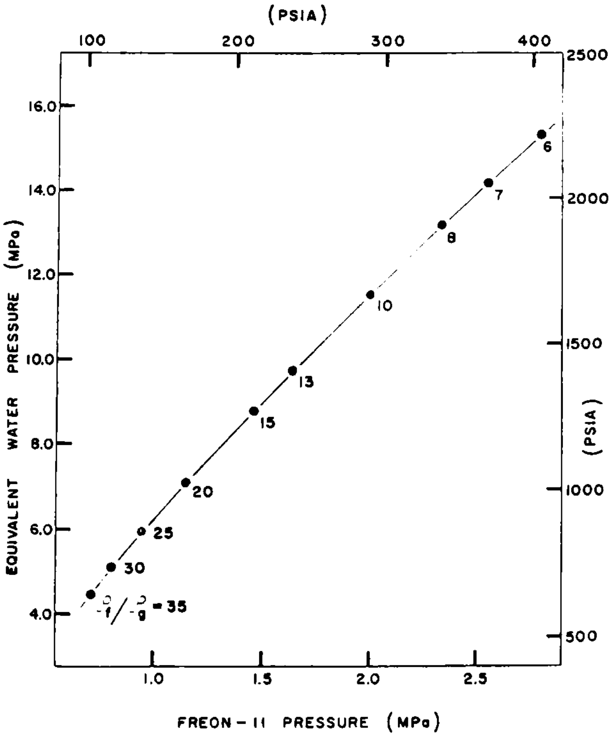

Fig. I.9. Equivalent Water Pressure for Freon-11 at Equal Orthobaric-density Ratio. ANL Neg. No. 900-77-140.

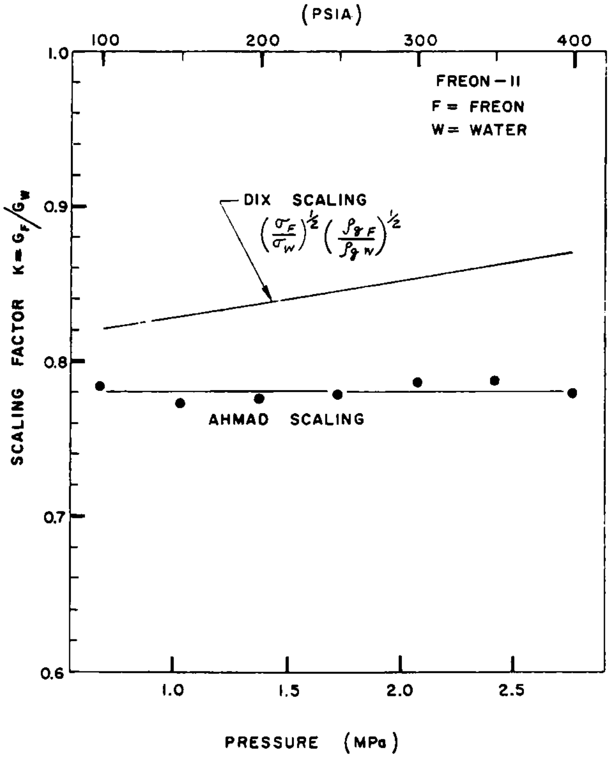

Fig. I.10. Mass-velocity Scaling Factor. ANL Neg. No. 900-77-142.

where the subscripts F and W represent Freon and water, respectively. Figure I.11 compares an average experimental heat flux with the predicted one; the agreement was within 5%. Figure I.12 shows good comparison with another round-tube uniform-heat-flux Freon-11 data[10] in the subcooled CHF region also.

4. Transient CHF Results

Four blowdown tests have been performed with the initial conditions as given in Table I.2. Using Ahmad's model, the equivalent water conditions during the steady state can be approximated as shown in Table I.3. The tests were conducted with the same initial heat flux, velocity, and temperature, but the operating pressure was different; Tests DB-107 and -111 were conducted at 2.20 MPa (P/P_C = 0.5), and Tests DB-108 and -112 at 2.78 MPa (P/P_C = 0.63). As shown in Figs. I.13-I.16, the steady-state subcooled boiling region was governed by the initial pressure; other parameters remaining constant. Initial power was maintained constant during the transient until power trip. The trip setting and the time of power trip are shown in Table I.4. The computer plots of the digitized transient data are presented in Figs. I.17-I.38.

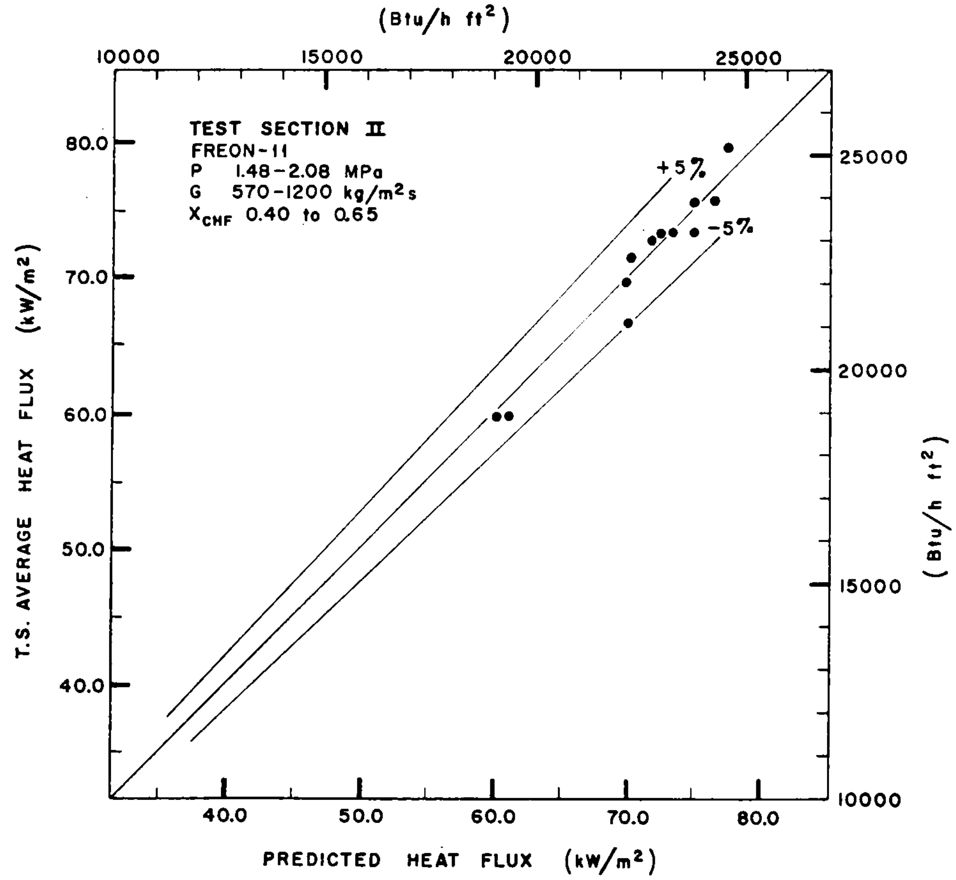

Fig. I.11. Comparison between Measured CHF and Bowring's Scaled CHF Prediction. ANL Neg. No. 900-77-139.

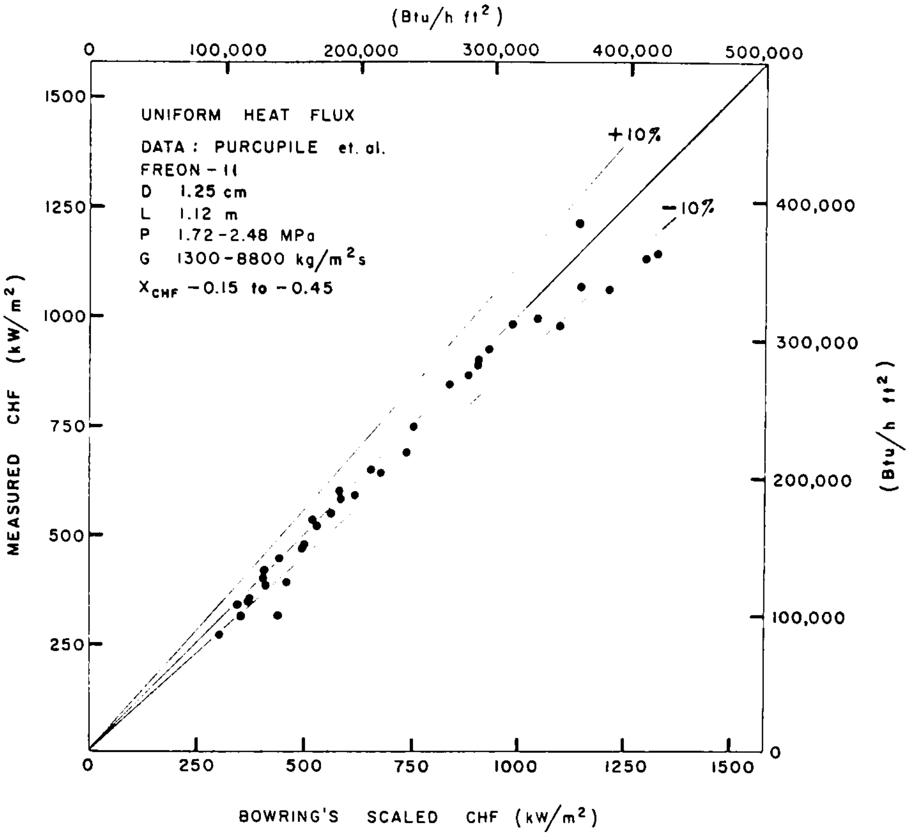

Fig. I.12. Comparison between Purcupile's CHF Data and Bowring's Scaled CHF Prediction. ANL Neg. No. 900-77-138.

TABLE I.2. Steady-state Test Conditions in Test Section II

Test No.	Pressure, MPa	Fluid Temperature, °C		Inlet Velocity, m/s	Mass Flow Rate, kg/m² · s	Heat Input, kW
		Inlet	Outlet			
DB-107	2.19	111	145	1.07	1330	5.05
DB-108	2.76	114	150	1.04	1270	5.05
DB-111	2.23	114	148	1.04	1280	5.03
DB-112	2.79	114	148	1.04	1280	5.00

TABLE I.3. Equivalent Water Conditions during Steady-state Conditions

Parameter	Tests DB-107, -111		Tests DB-108, -112		Typical PWR Condition
	Freon-11	Water	Freon-11	Water	
P, MPa	2.21	12.5	2.79	15.4	15.6
(psia)	(320)	(1815)	(404)	(2230)	(2265)
D, cm	1.17	1.17	1.17	1.17	1.35
L, m	2.75	2.75	2.75	2.75	3.66
T_i, °C	114.0	244.0	114.0	239.0	288
Δh_i, J/g	40.7	455.5	58.2	590.1	351.0
G, kg/m² · s	1288.0	1655.0	1288.0	1655.0	3390.0
ϕ, kW/m²					
Average	49.7	710.0	49.7	647.0	631.0
Zone A	34.7	496.3	34.7	451.2	-
B, D	52.1	744.6	52.1	676.7	-
C	60.9	870.8	60.9	792.0	-

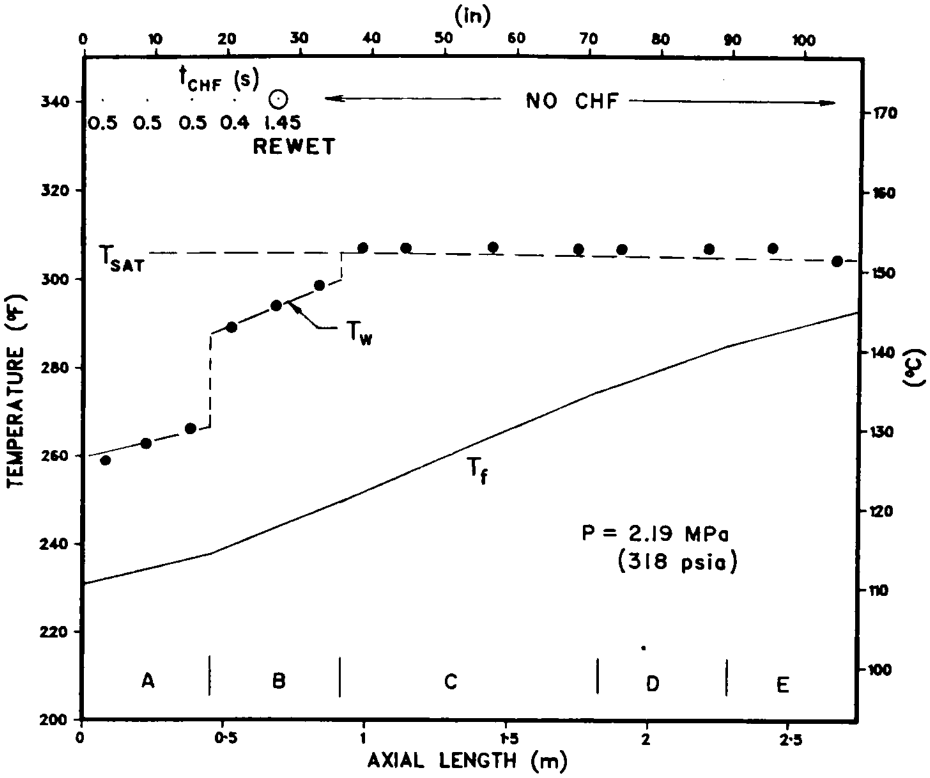

Fig. I.13. Steady-state Wall-temperature Profile in Test DB-107. ANL Neg. No. 900-77-144.

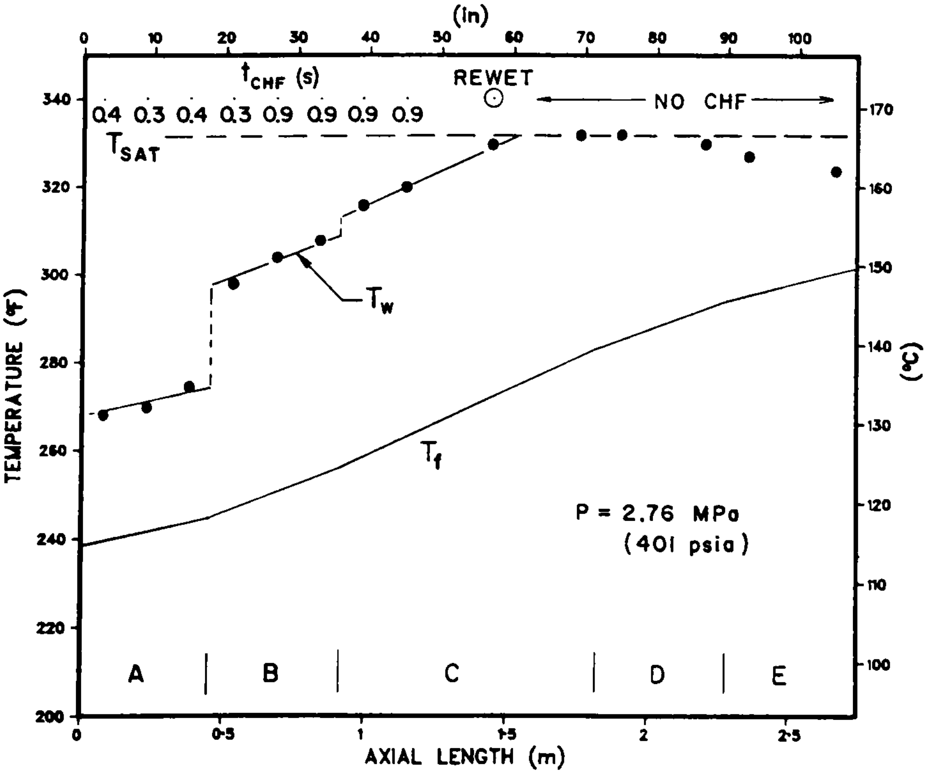

Fig. I.14. Steady-state Wall-temperature Profile in

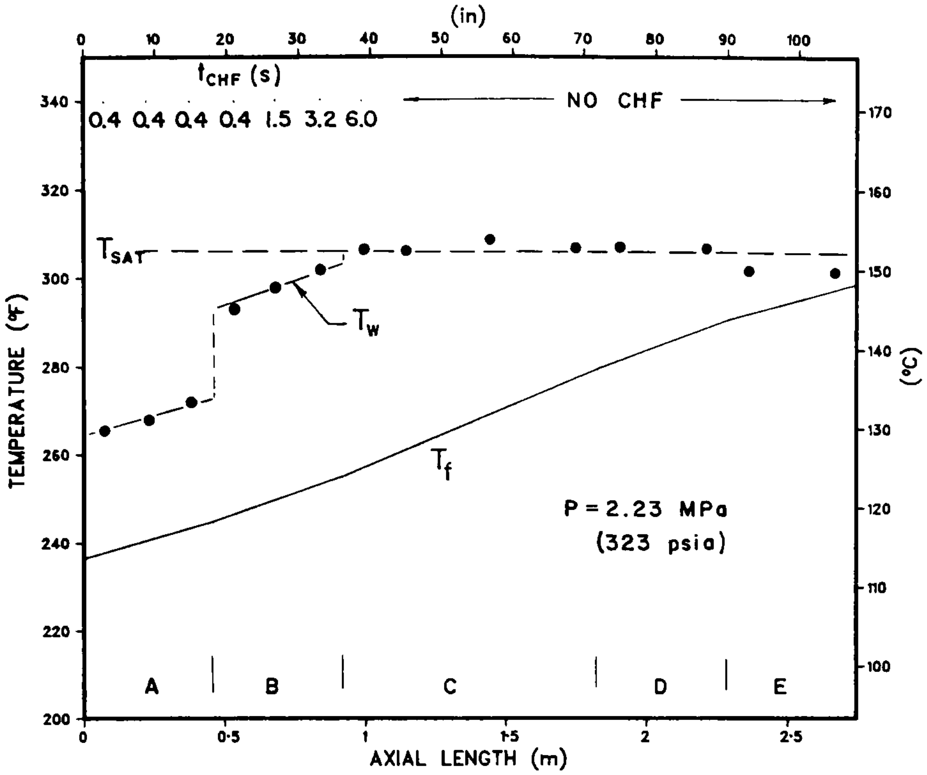

Fig. I.15. Steady-state Wall-temperature Profile in Test DB-111. ANL Neg. No. 900-77-147.

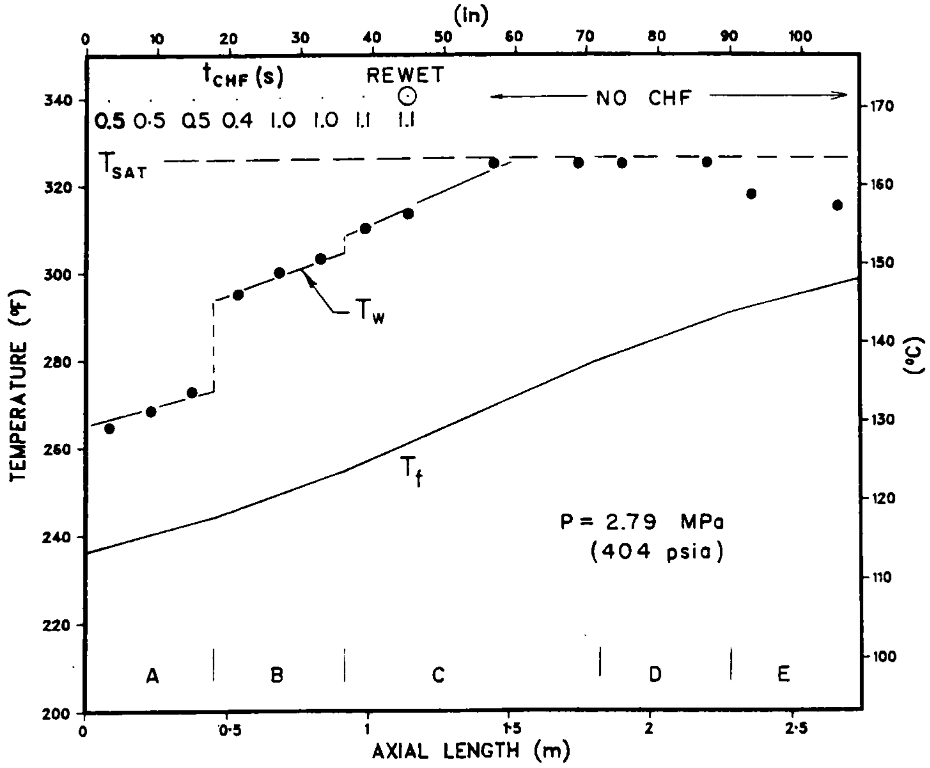

Fig. I.16. Steady-state Wall-temperature Profile in

TABLE I.4. Other Parameters during Blowdown

Test No.	Break Orifice Diameter, cm	Volume Above Heated Zone,[a] cm^3	Temperature Tripped Setting,[b] °C	Time at Power Trip, s
DB-107	0.38	2620	193	3.8
DB-108	0.38	2620	193	3.3
DB-111	0.38	2620	221	7.7
DB-112	0.38	2620	221	7.5

[a] Volume above heated zone/test section heated zone volume = 8.9.

[b] The trip temperature was first sensed by TC19B in all these tests.

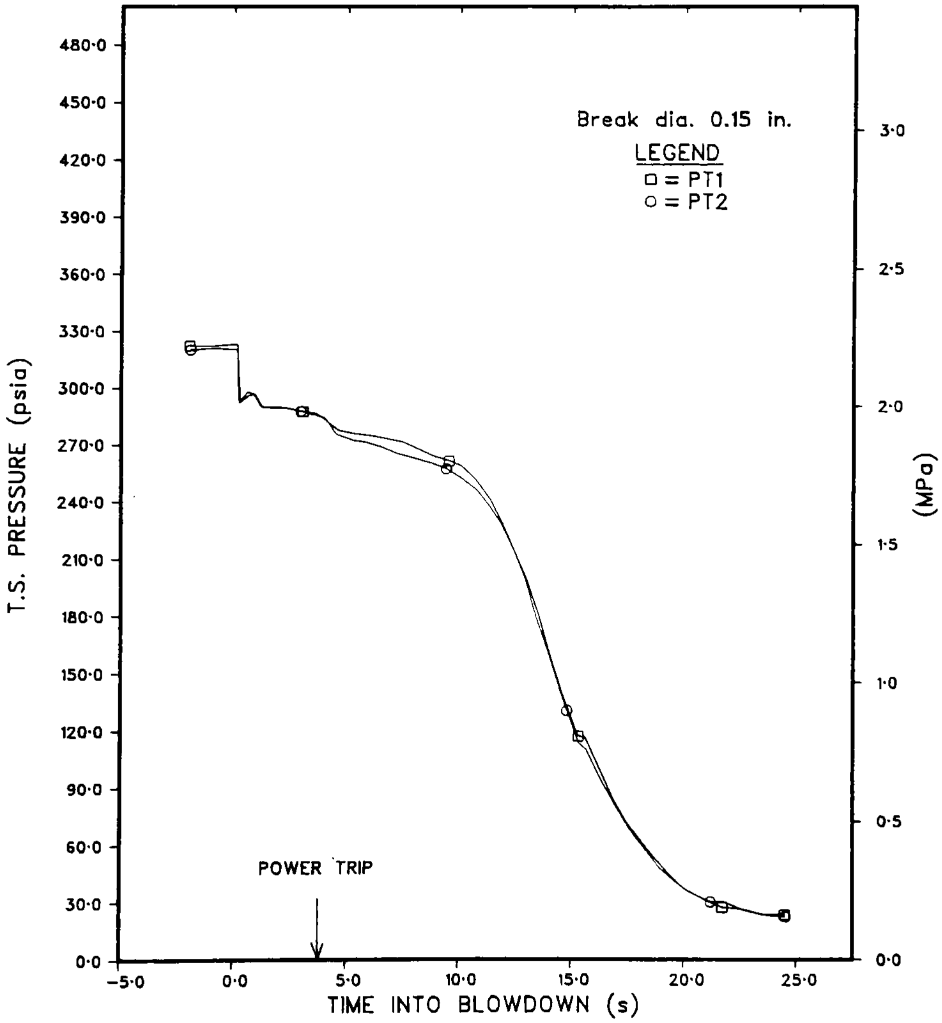

Fig. I.17. System Pressure during Test DB-107

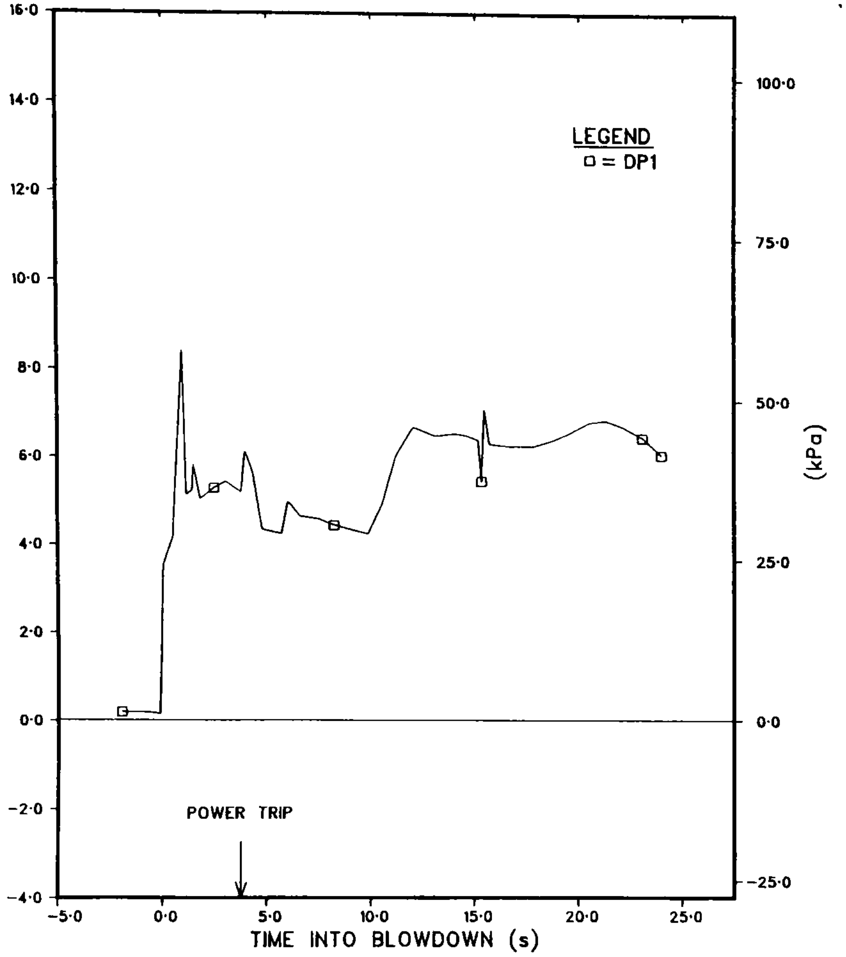

Fig. I.18. Differential Pressure across Test Section during Test DB-107

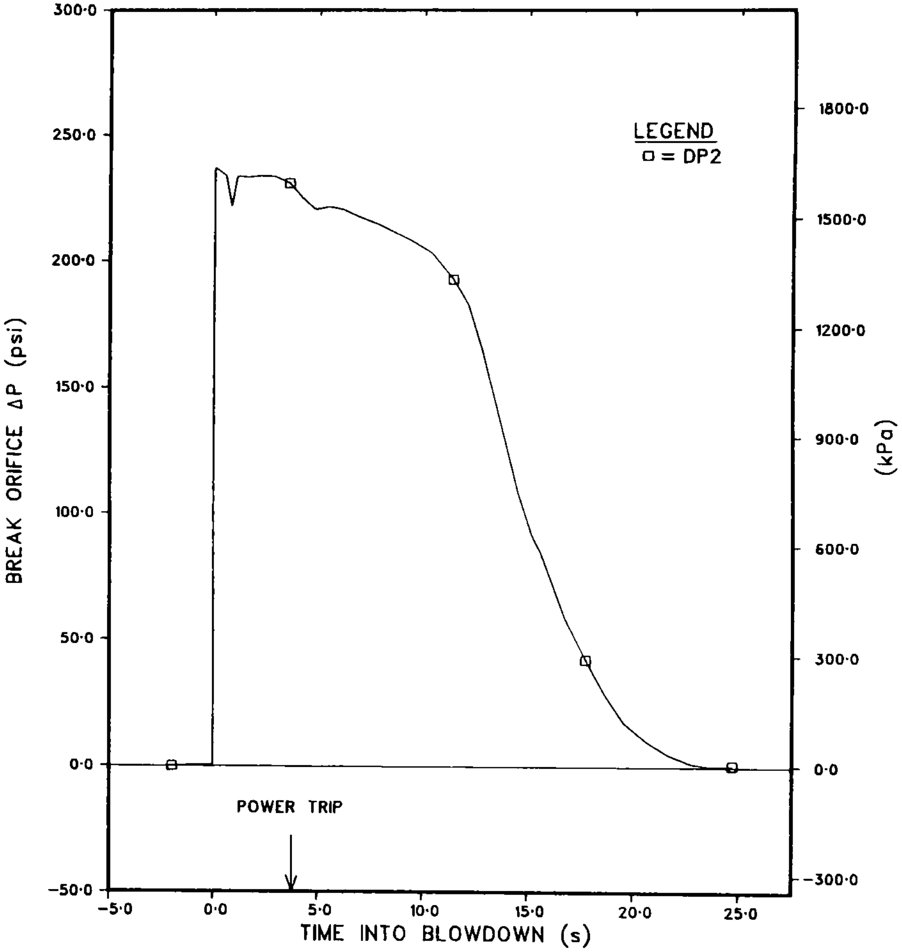

Fig. I.19. Differential Pressure across Break Orifice during Test DB-107

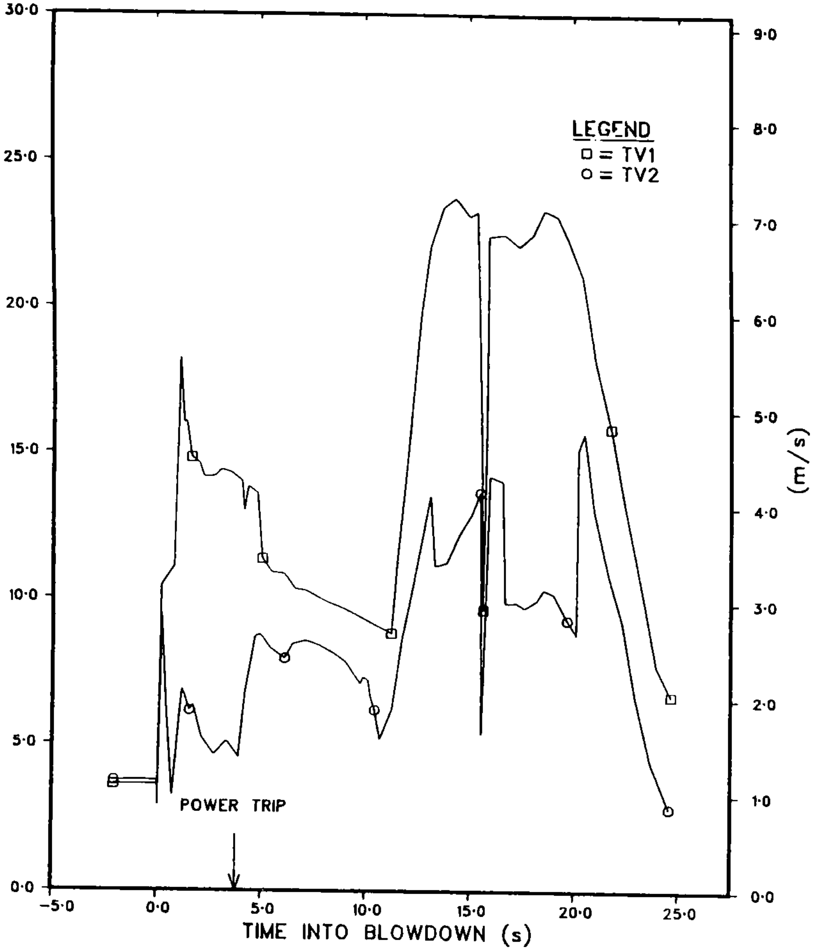

Fig. I.20. Turbine-flowmeter Measurement during Test DB-107

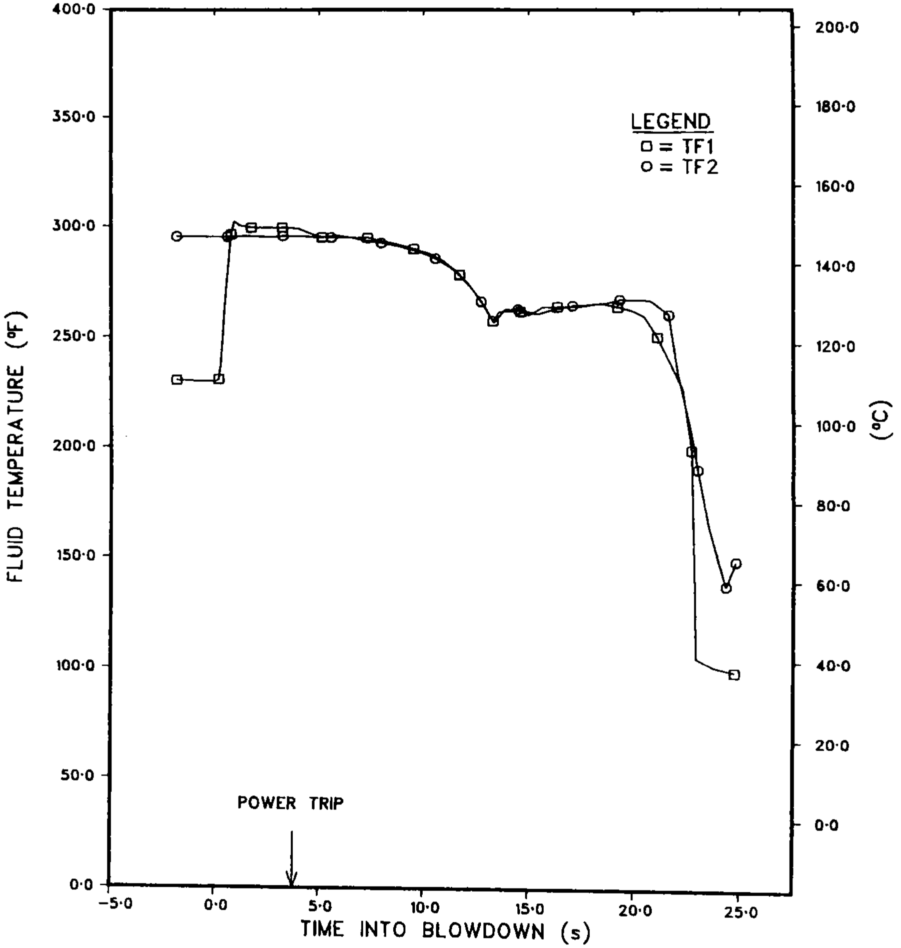

Fig. I.21. Fluid Temperature during Test DB-107

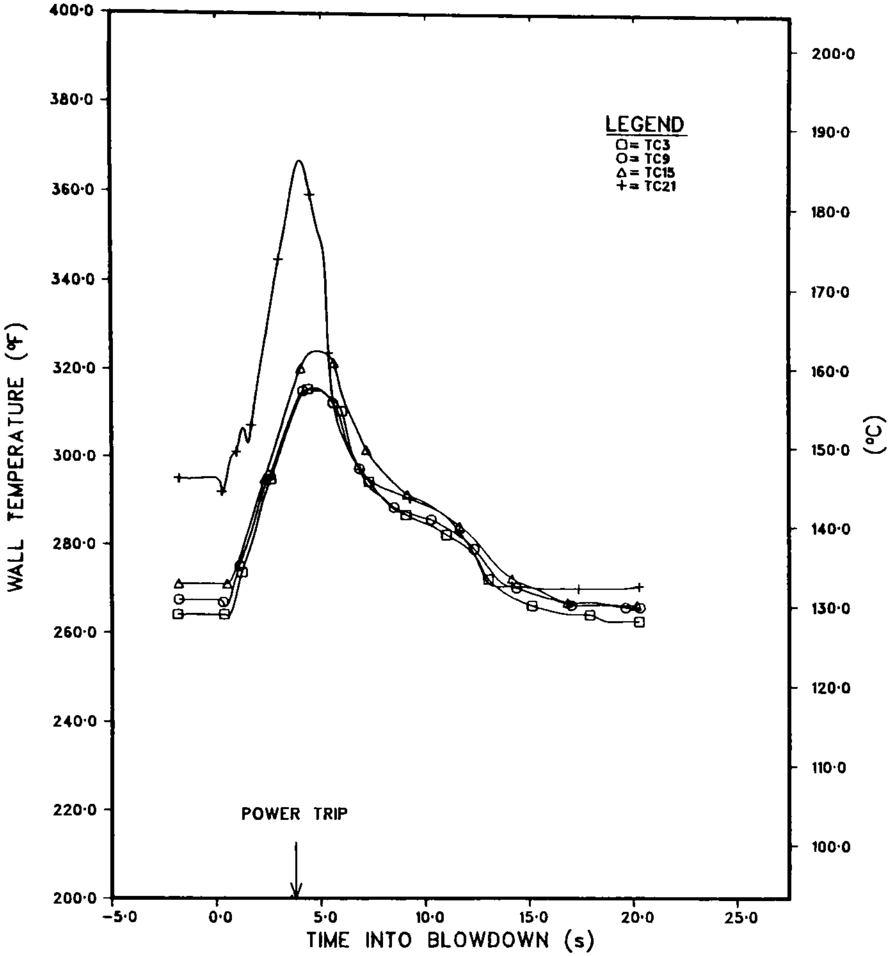

Fig. I.22. Wall-thermocouple Measurement during Test DB-107

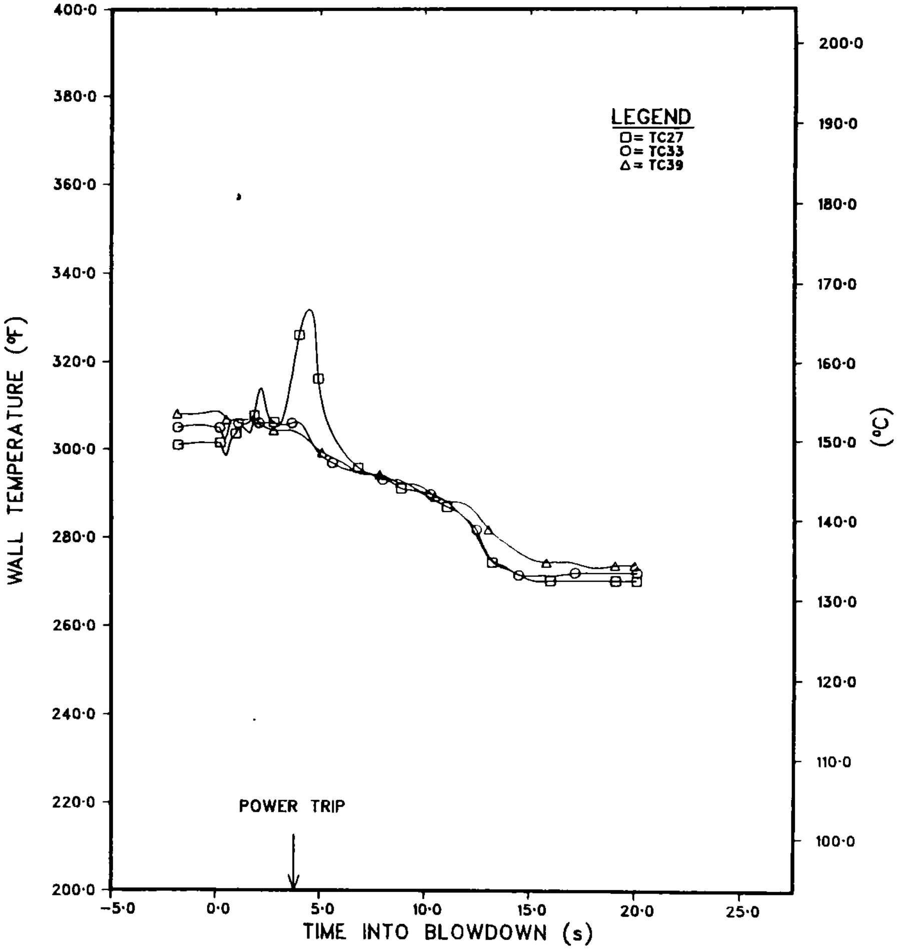

Fig. I.22 (Contd.)

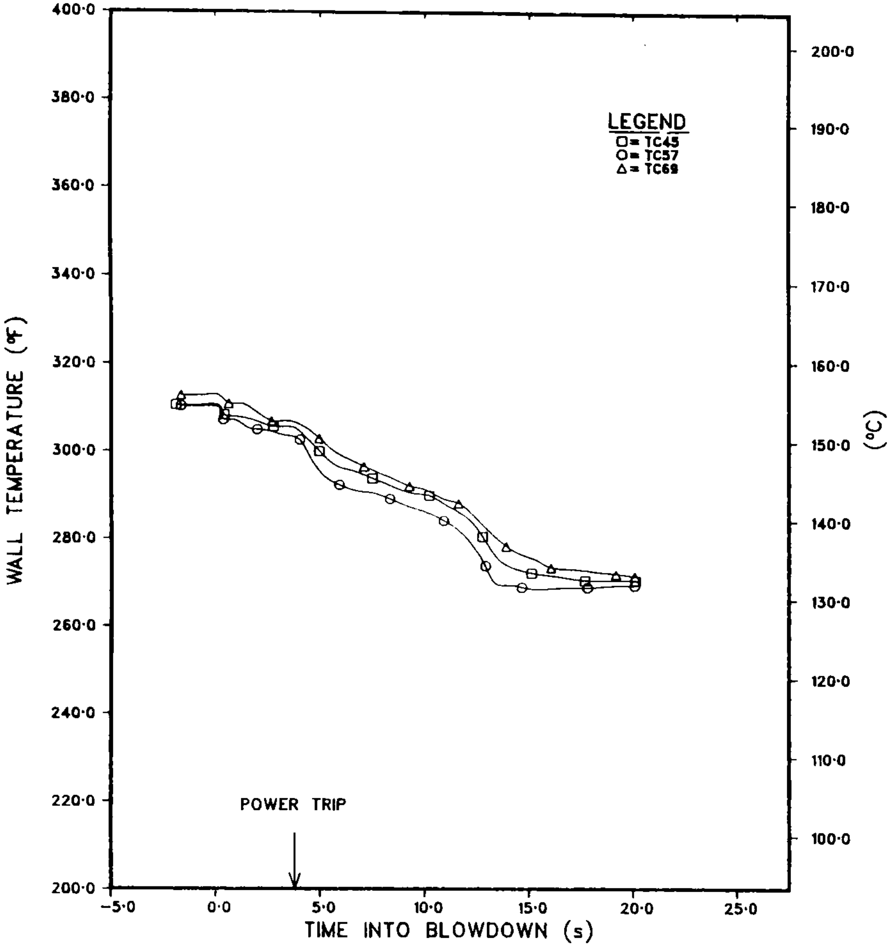

Fig. I.22 (Contd.)

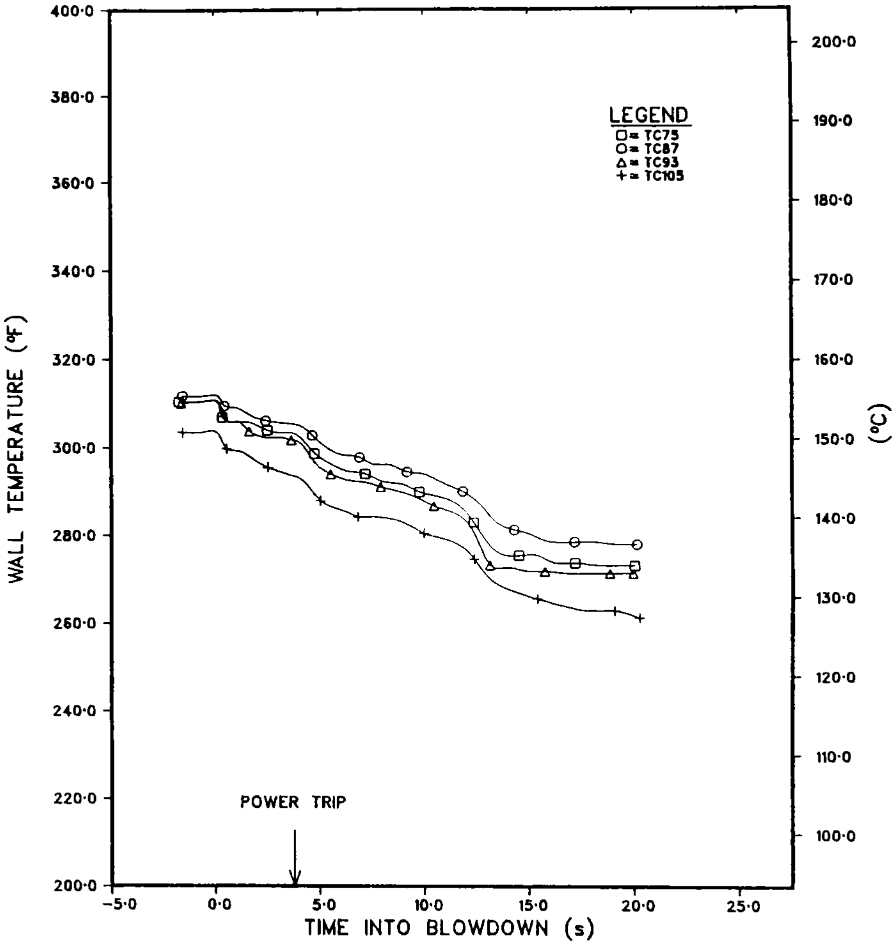

Fig. I.22 (Contd.)

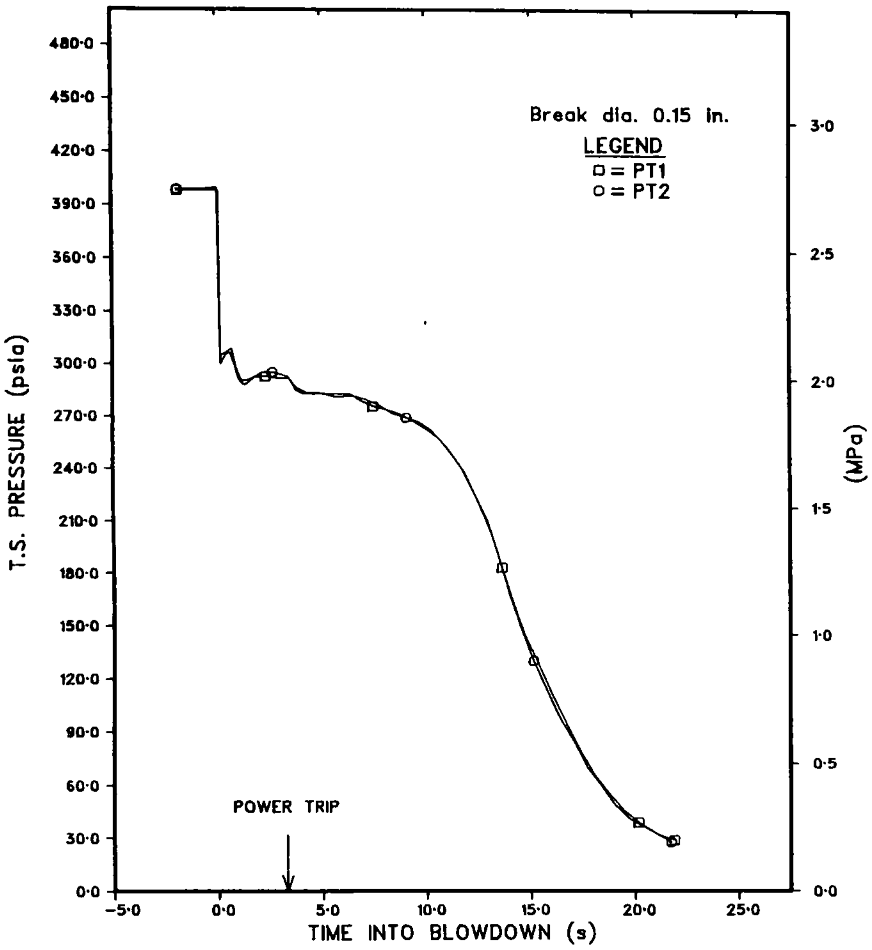

Fig. I.23. System Pressure during Test DB–108

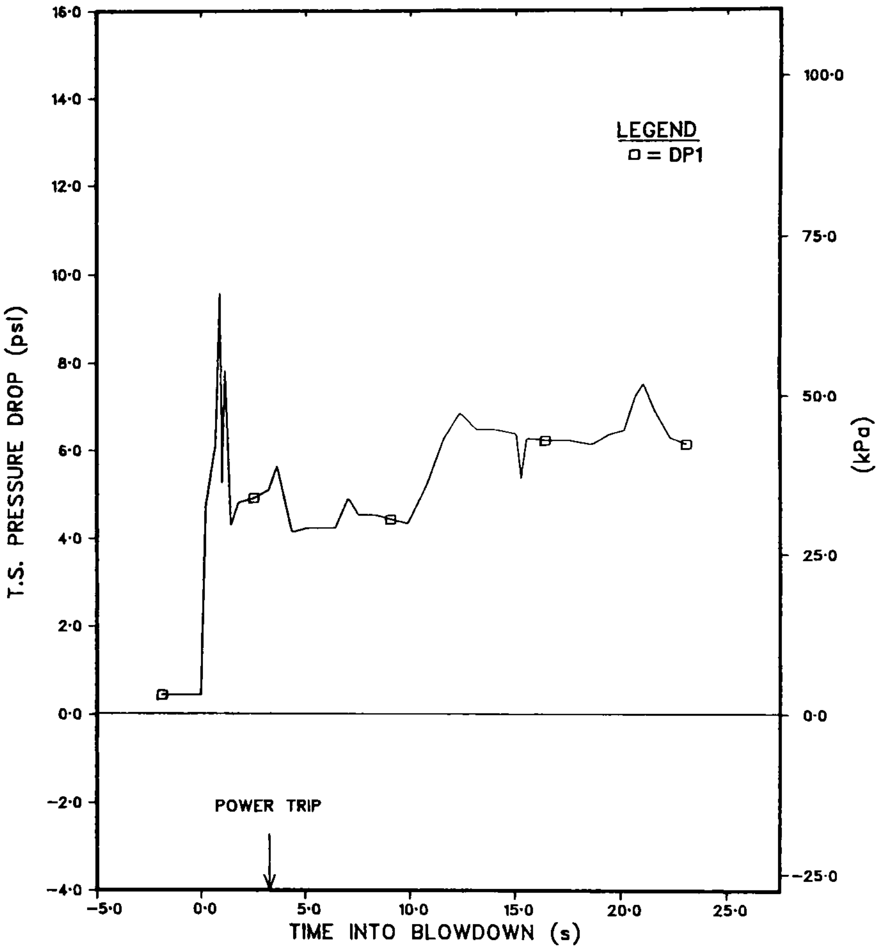

Fig. I.24. Differential Pressure across Test Section during Test DB–108

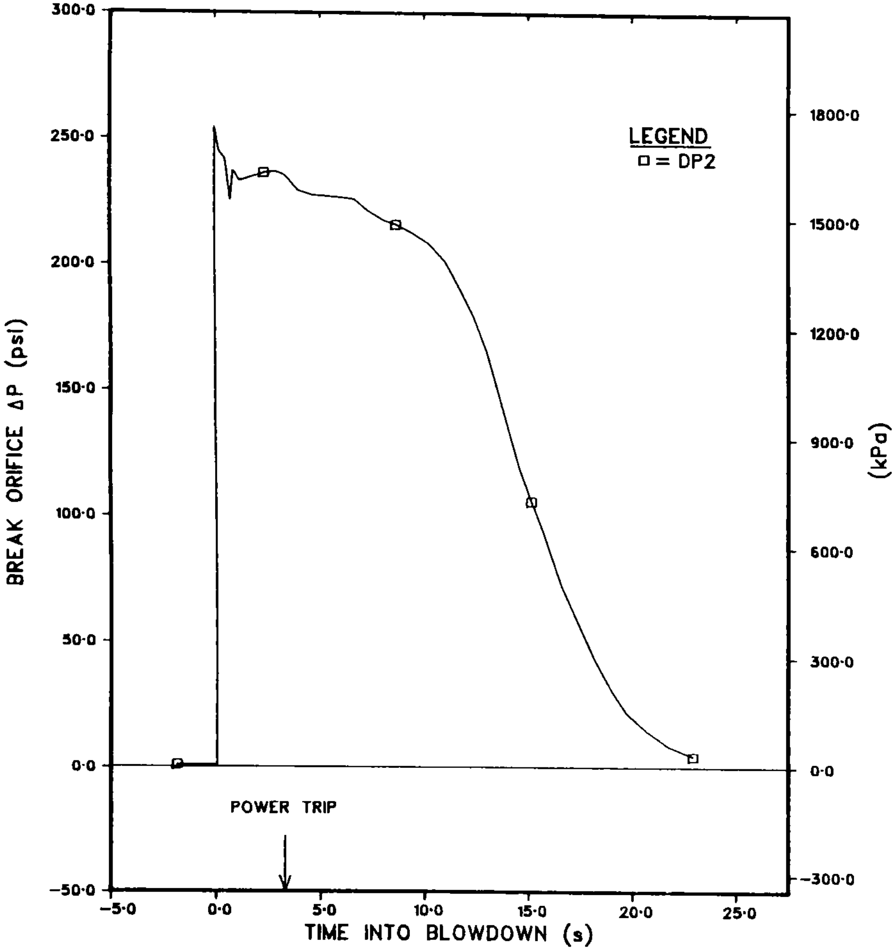

Fig. I.25. Differential Pressure across Break Orifice during Test DB–108

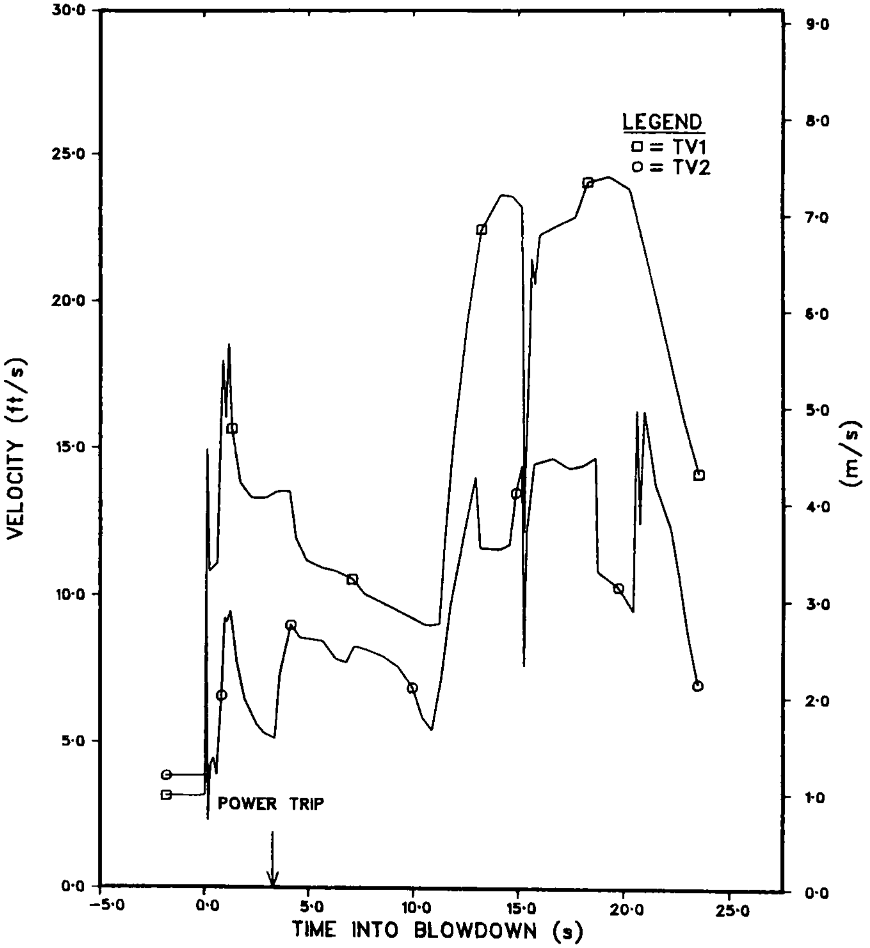

Fig. I.26. Turbine–flowmeter Measurement during Test DB–108

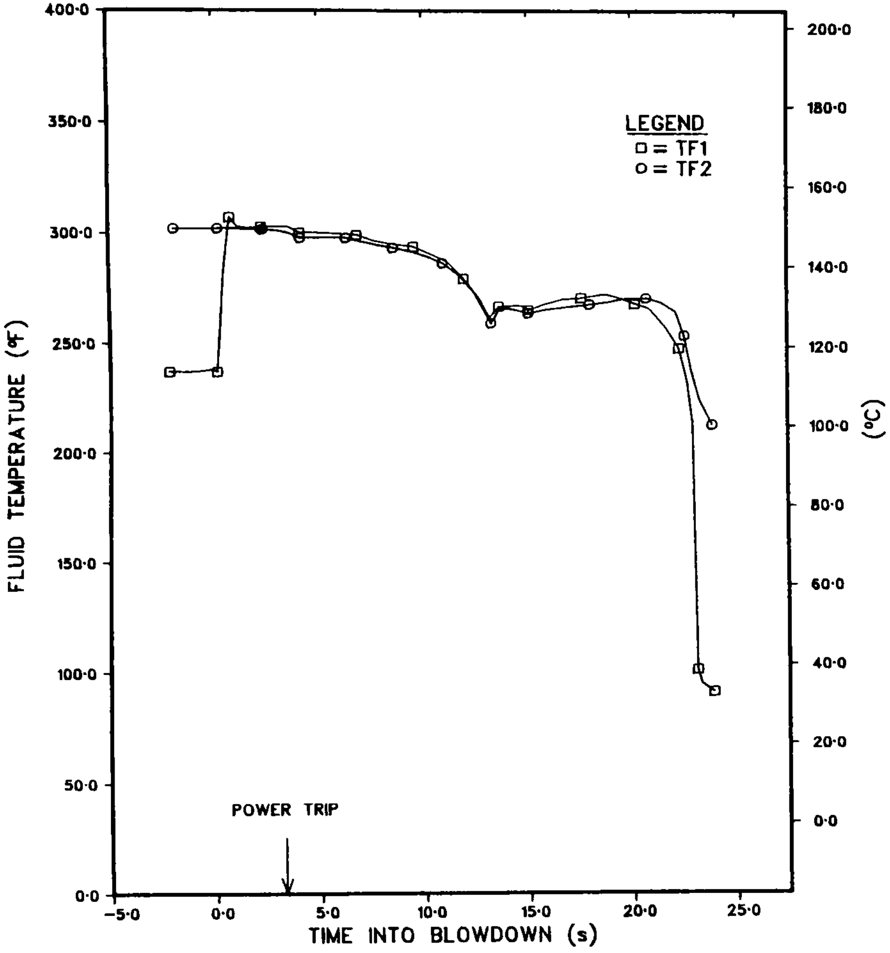

Fig. I.27. Fluid Temperature during Test DB–108

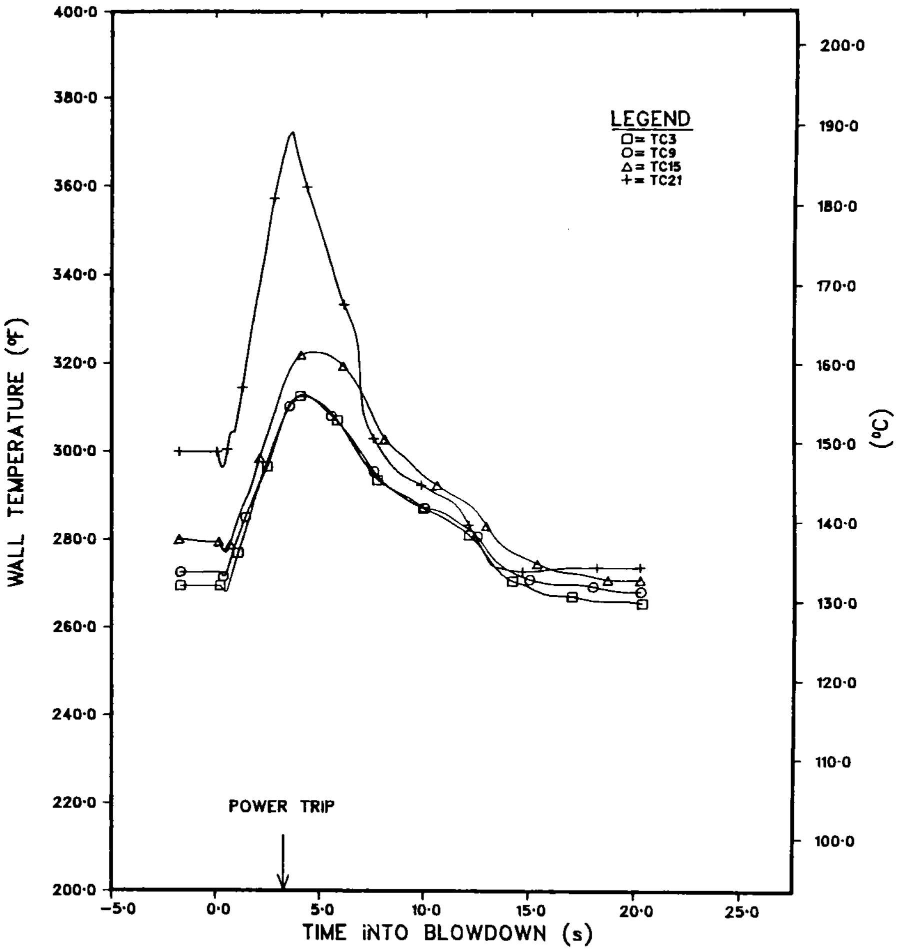

Fig. I.28. Wall–thermocouple Measurement during Test DB–108

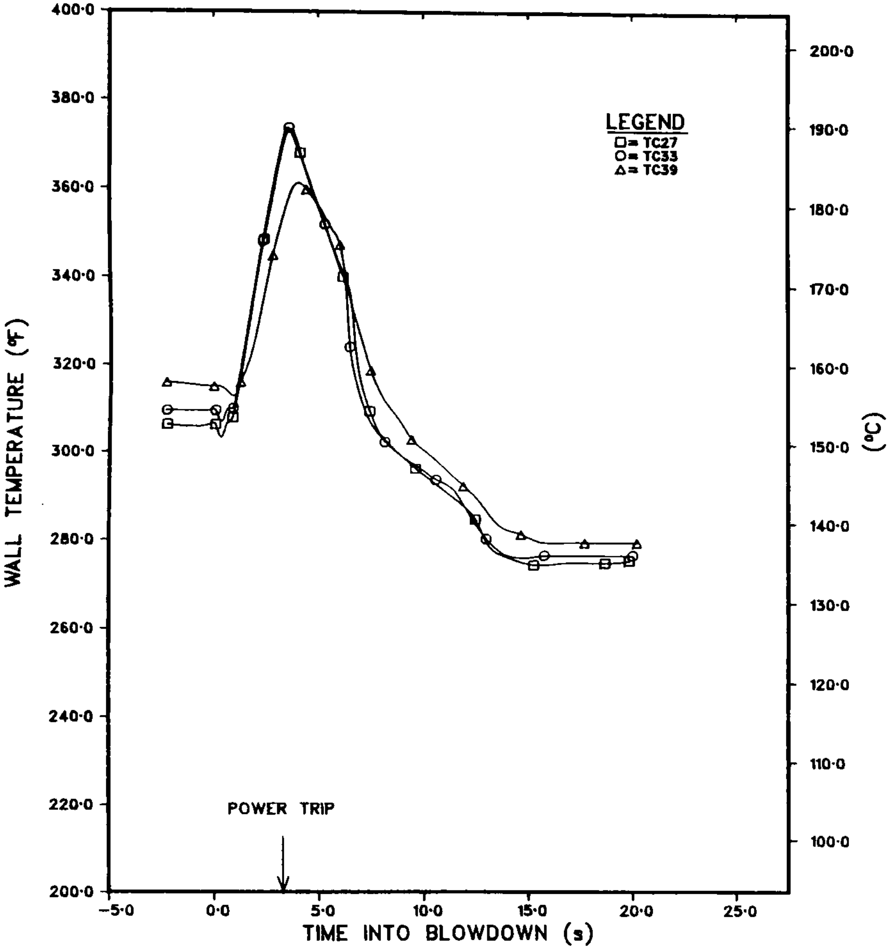

Fig. I.28 (Contd.)

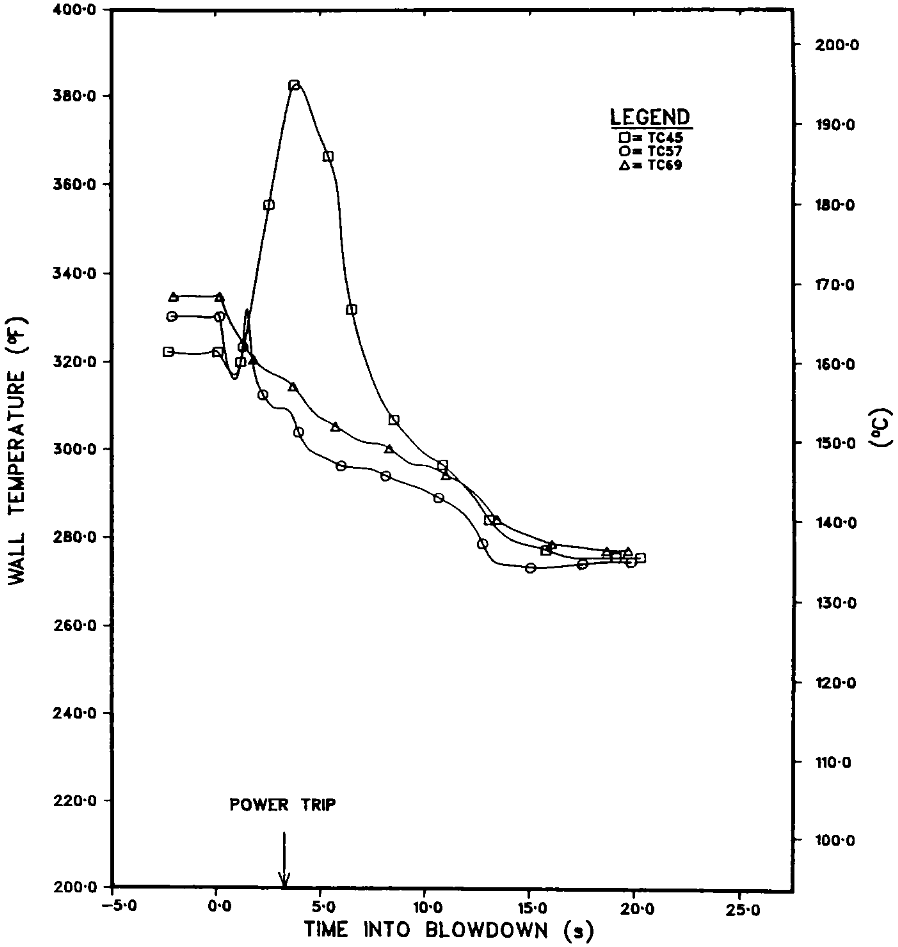

Fig. I.28 (Contd.)

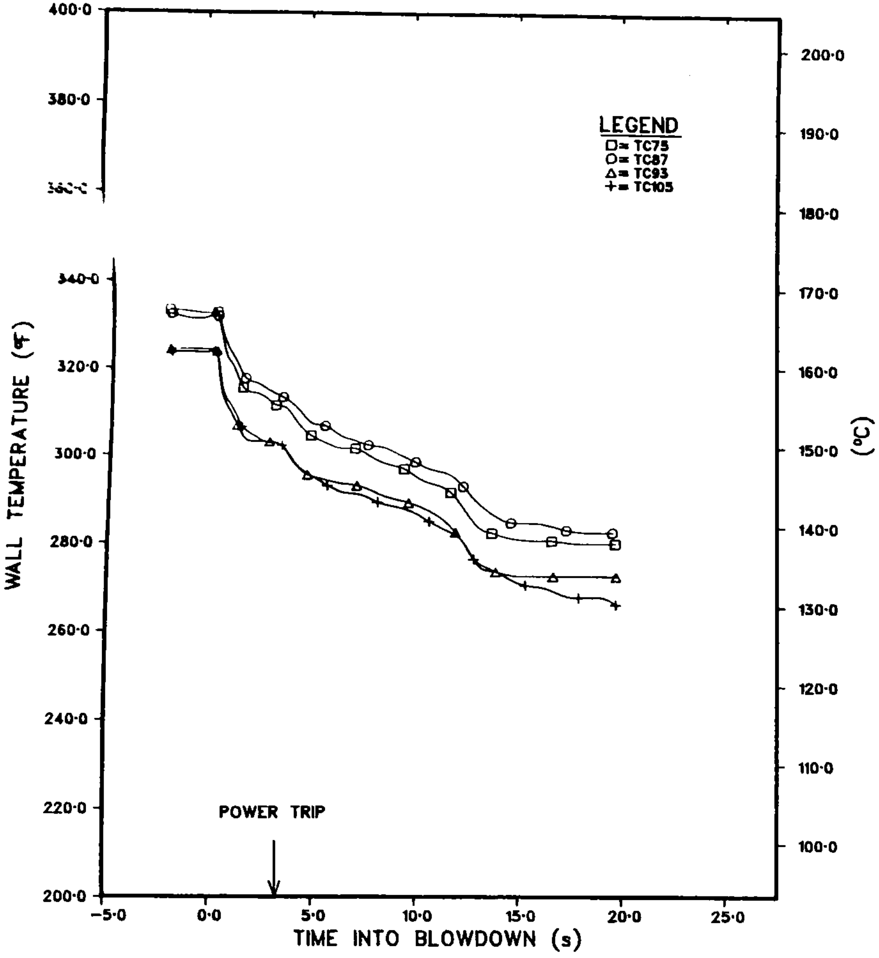

Fig. I.28 (Contd.)

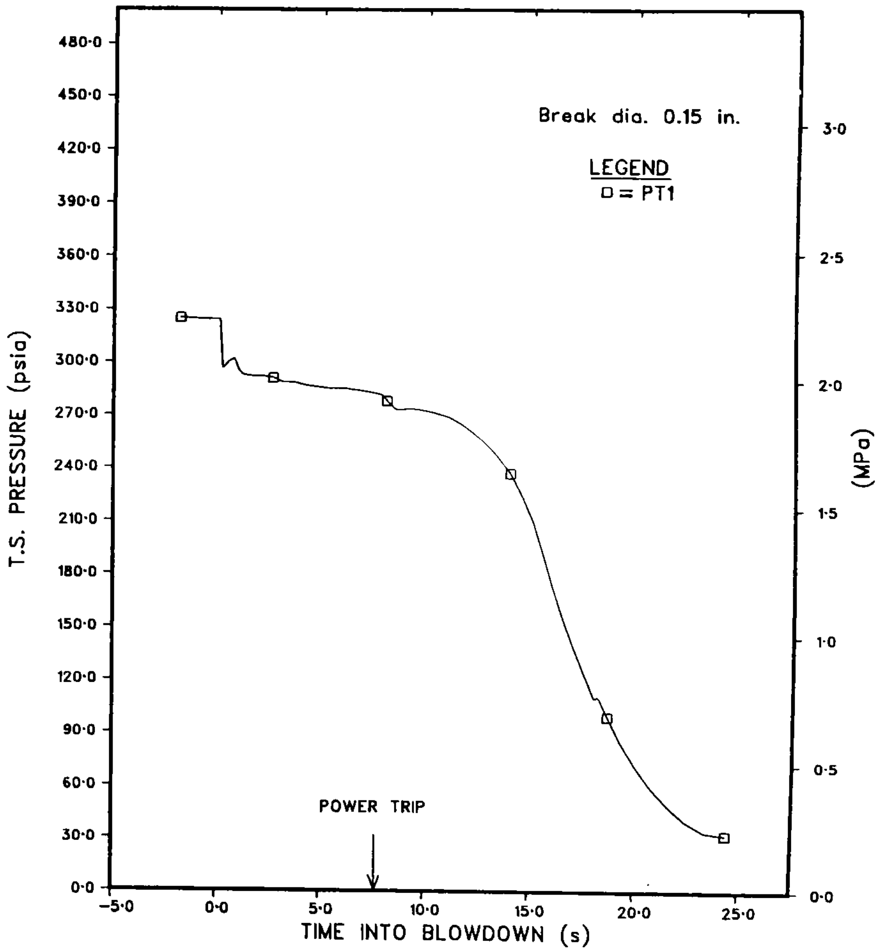

Fig. I.29. System Pressure during Test DB-111

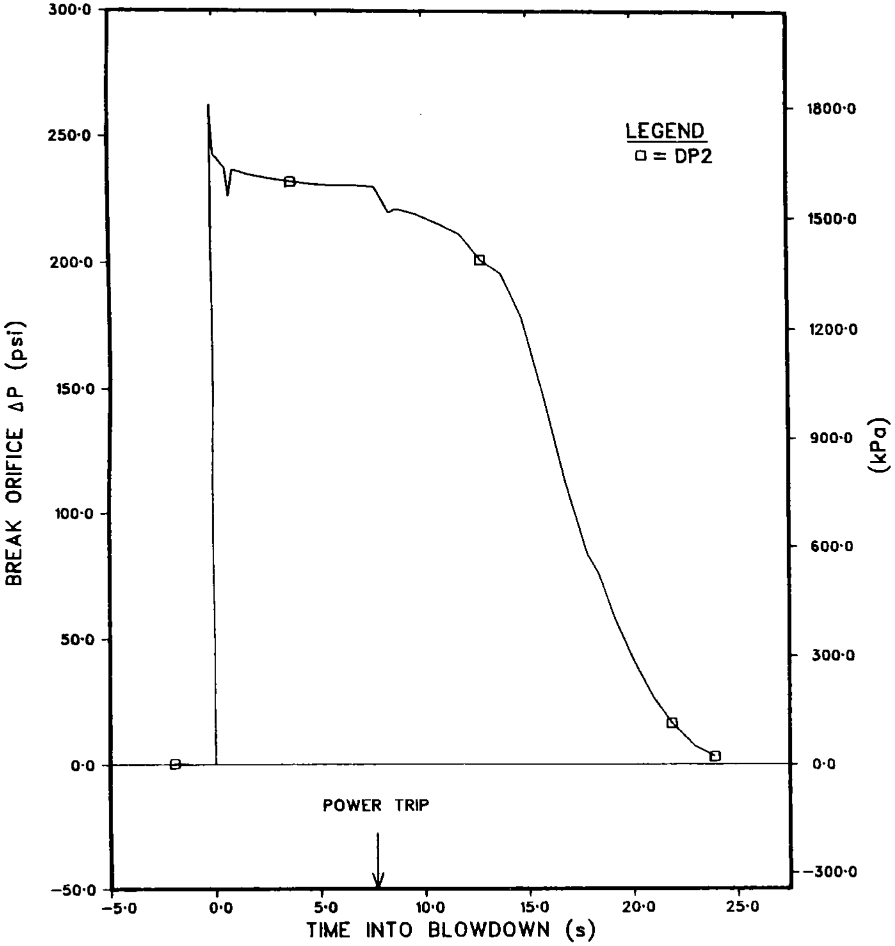

Fig. I.30. Differential Pressure across Break Orifice during Test DB-111

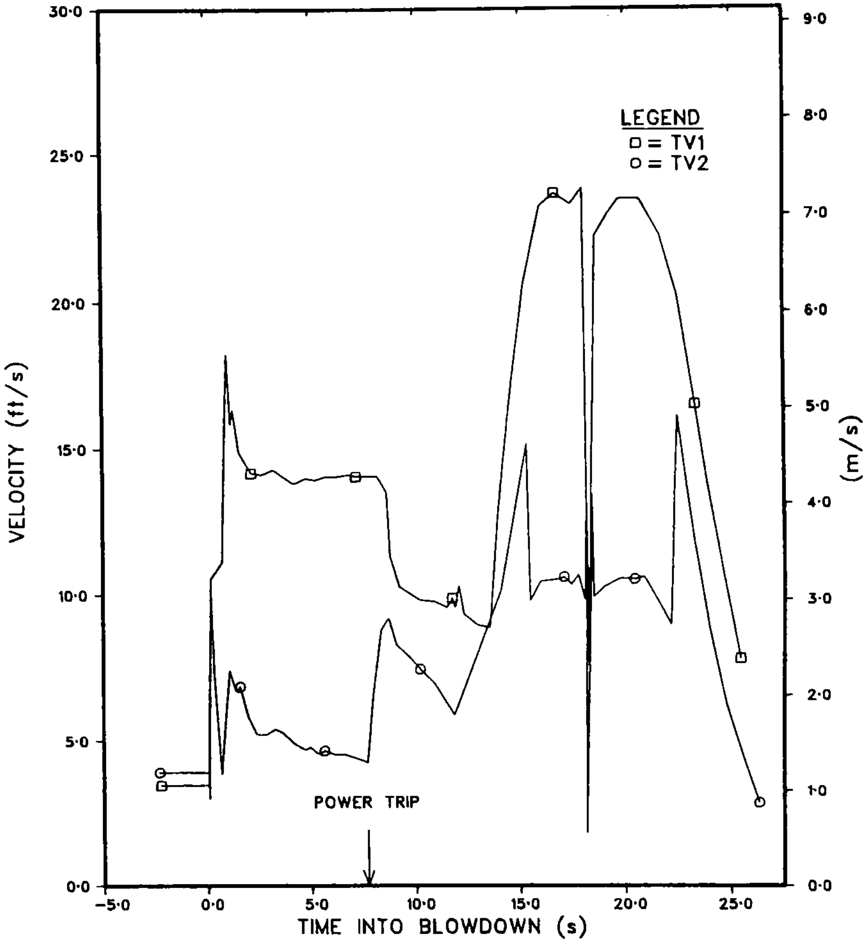

Fig. I.31. Turbine-flowmeter Measurement during Test DB-111

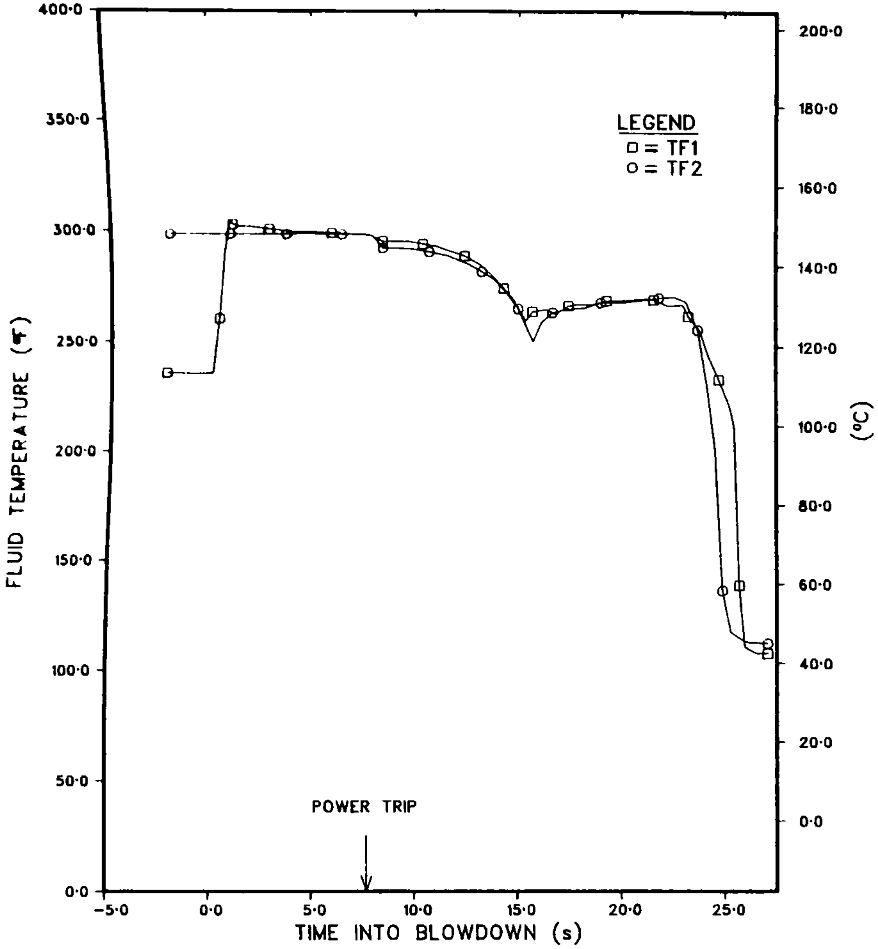

Fig. I.32. Fluid Temperature during Test DB-111

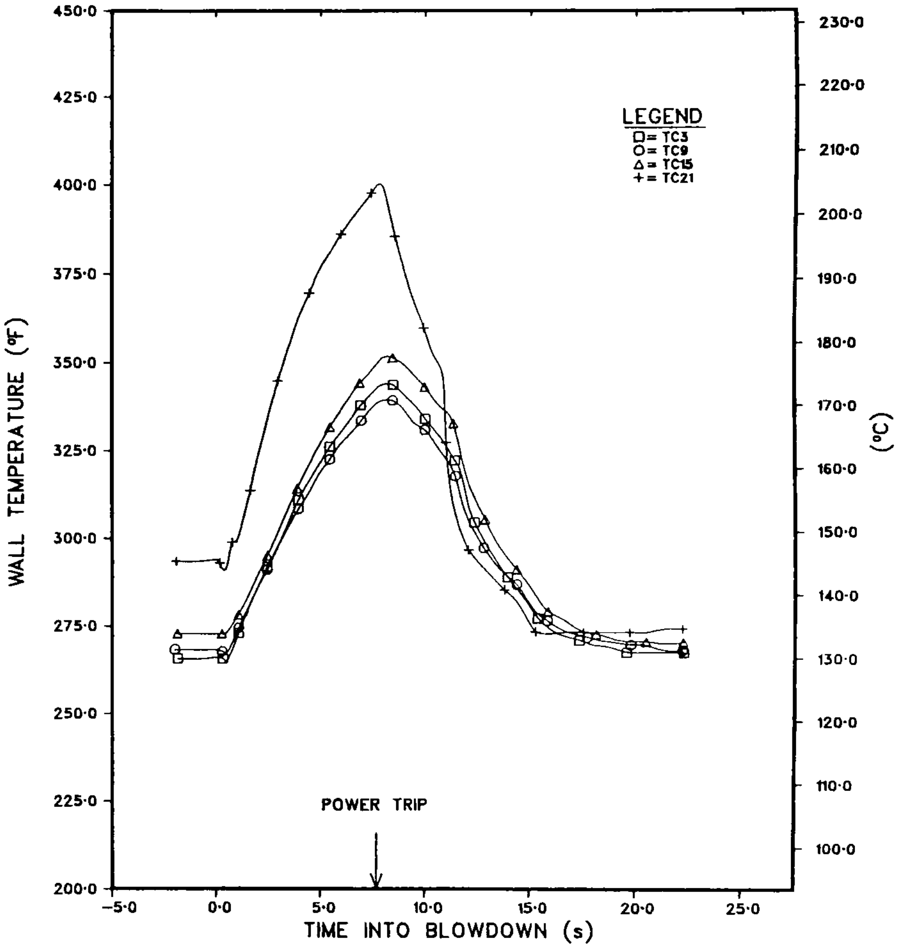

Fig. I.33. Wall-thermocouple Measurement during Test DB-111

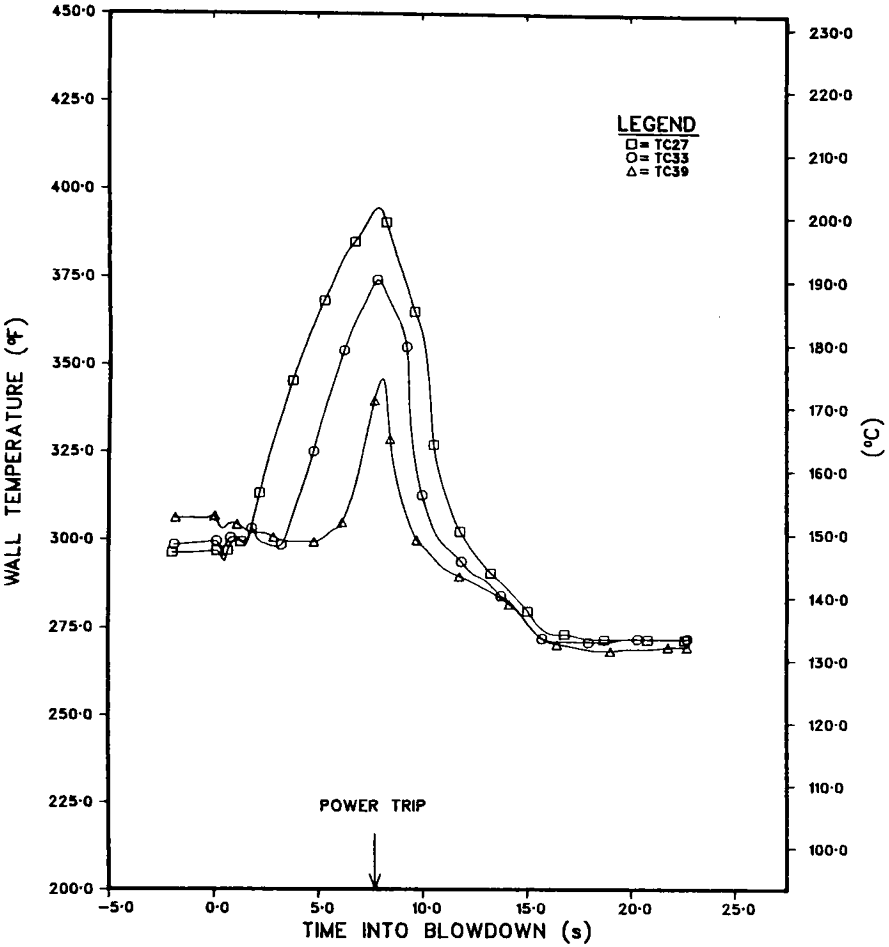

Fig. I.33 (Contd.)

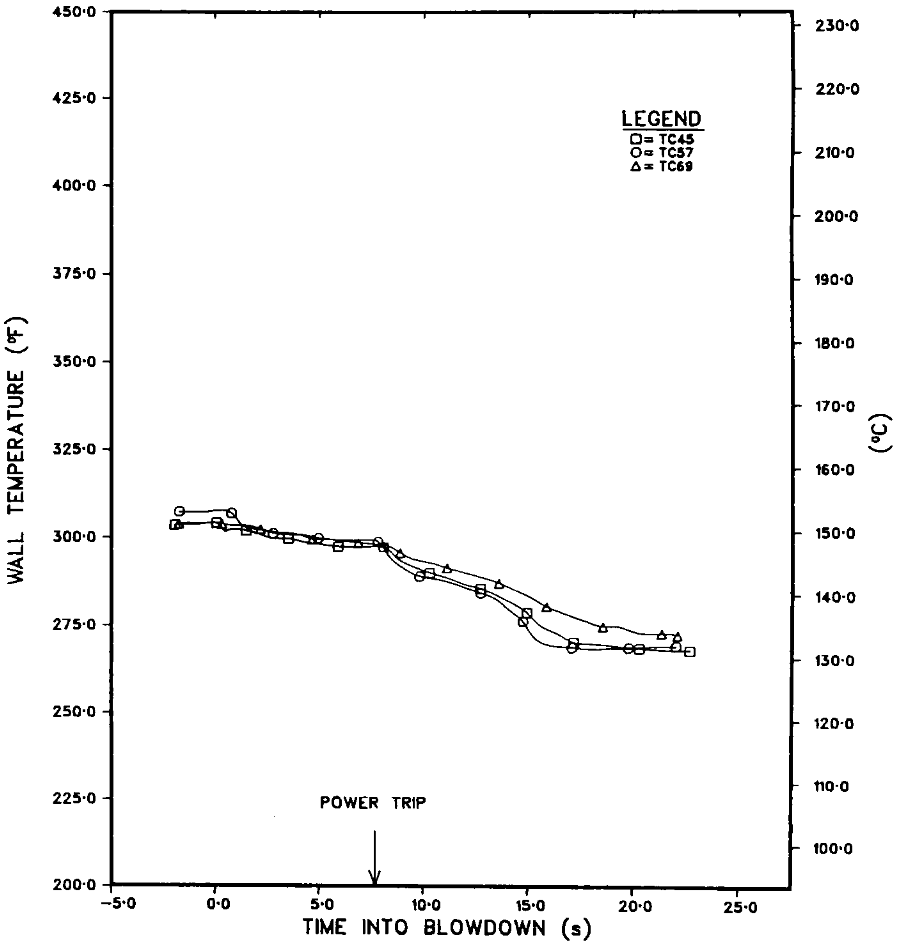

Fig. I.33 (Contd.)

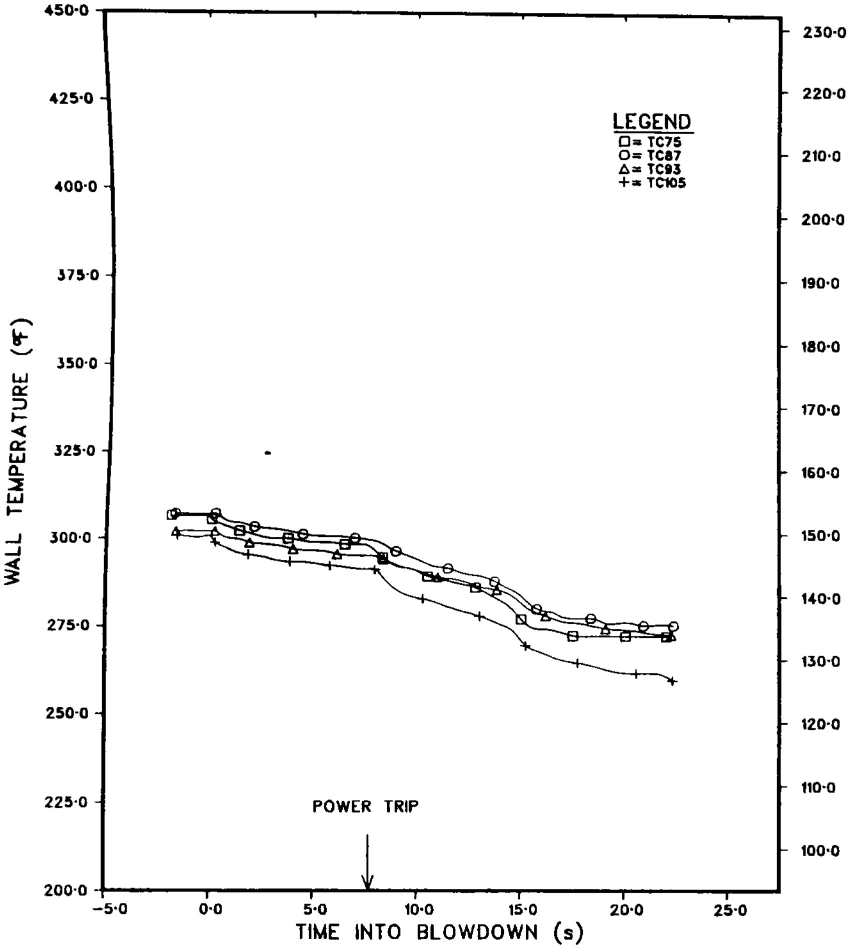

Fig. I.33 (Contd.)

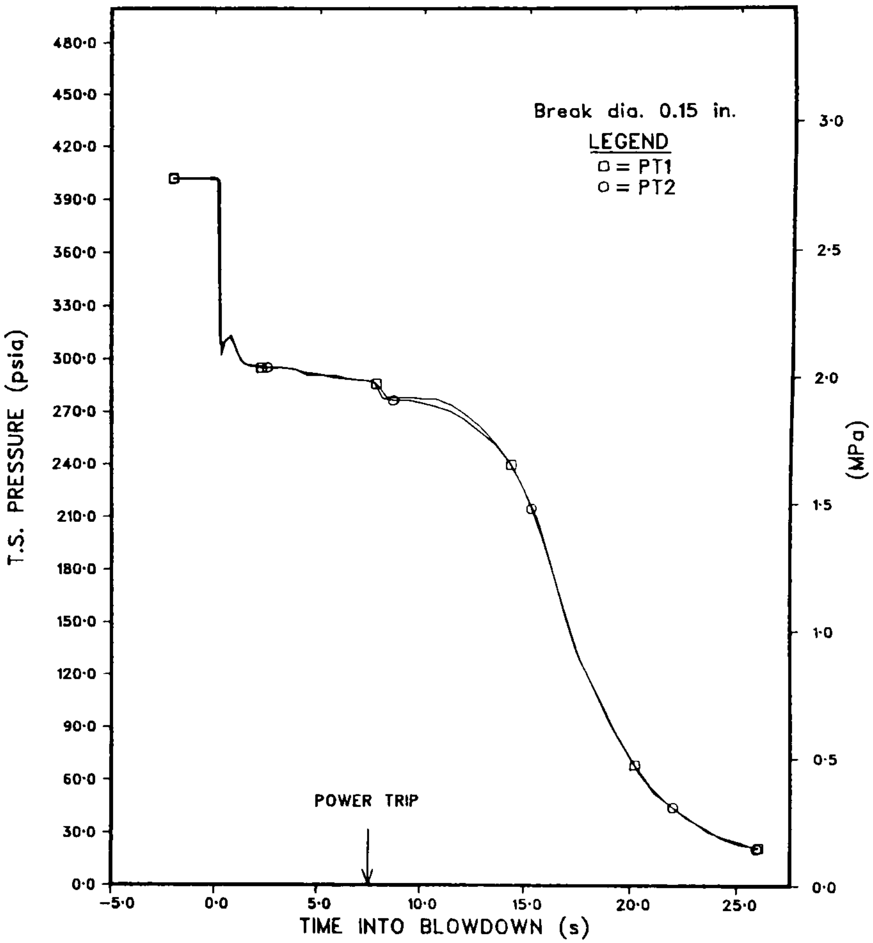

Fig. I.34. System Pressure during Test DB-112

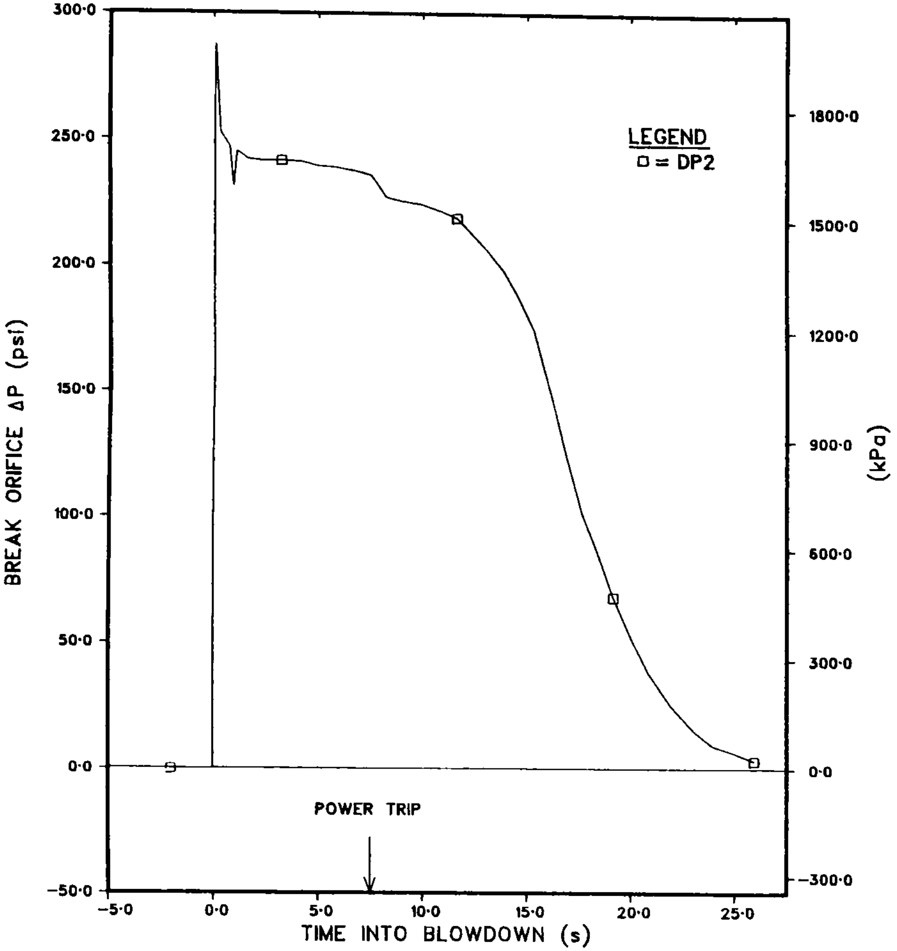

Fig. I.35. Differential Pressure across Break Orifice during Test DB-112

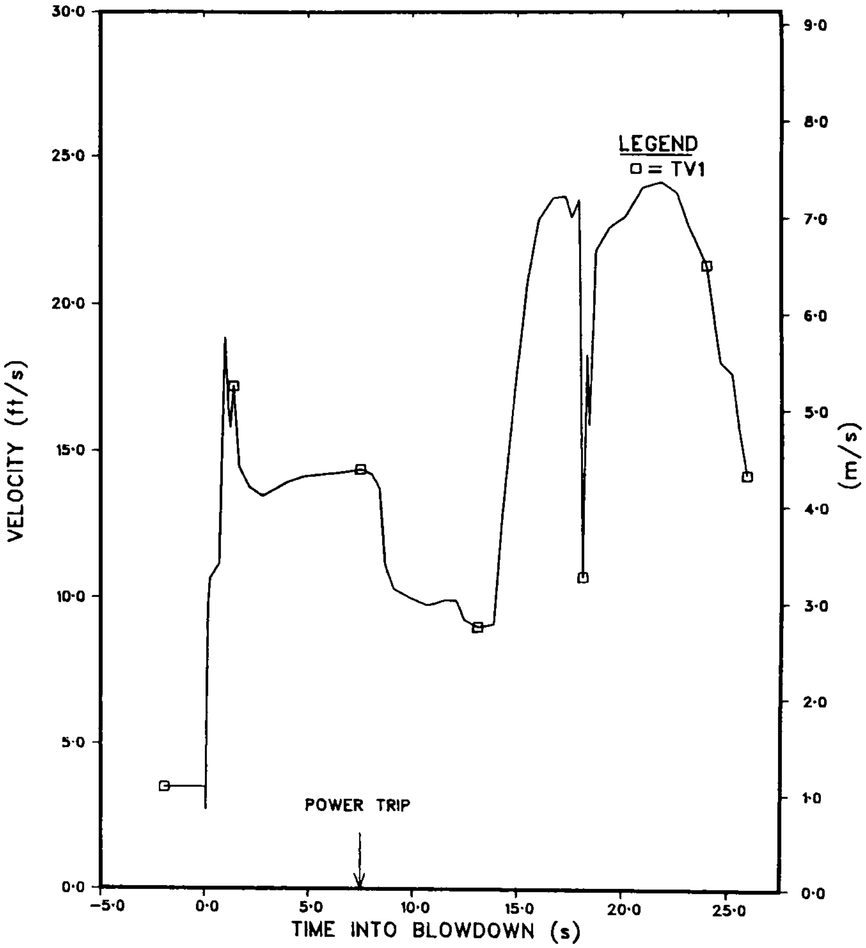

Fig. I.36. Turbine-flowmeter Measurement during Test DB-112

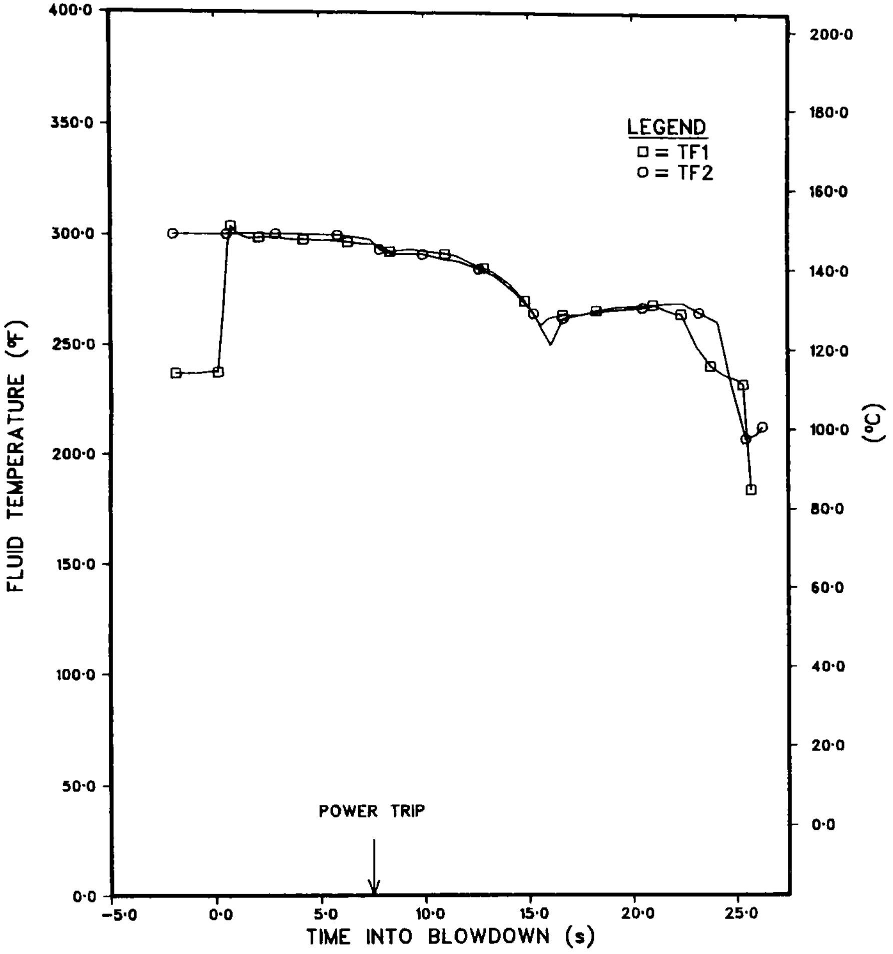

Fig. I.37. Fluid Temperature during Test DB-112

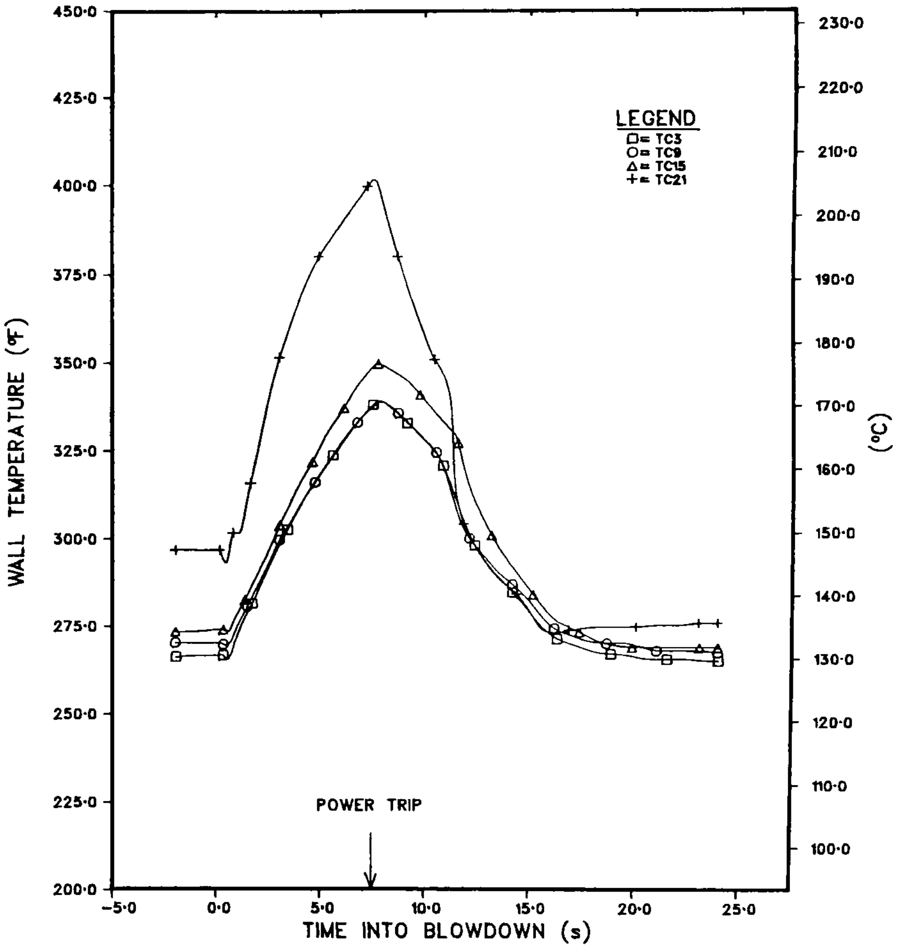

Fig. I.38. Wall-thermocouple Measurement during Test DB-112

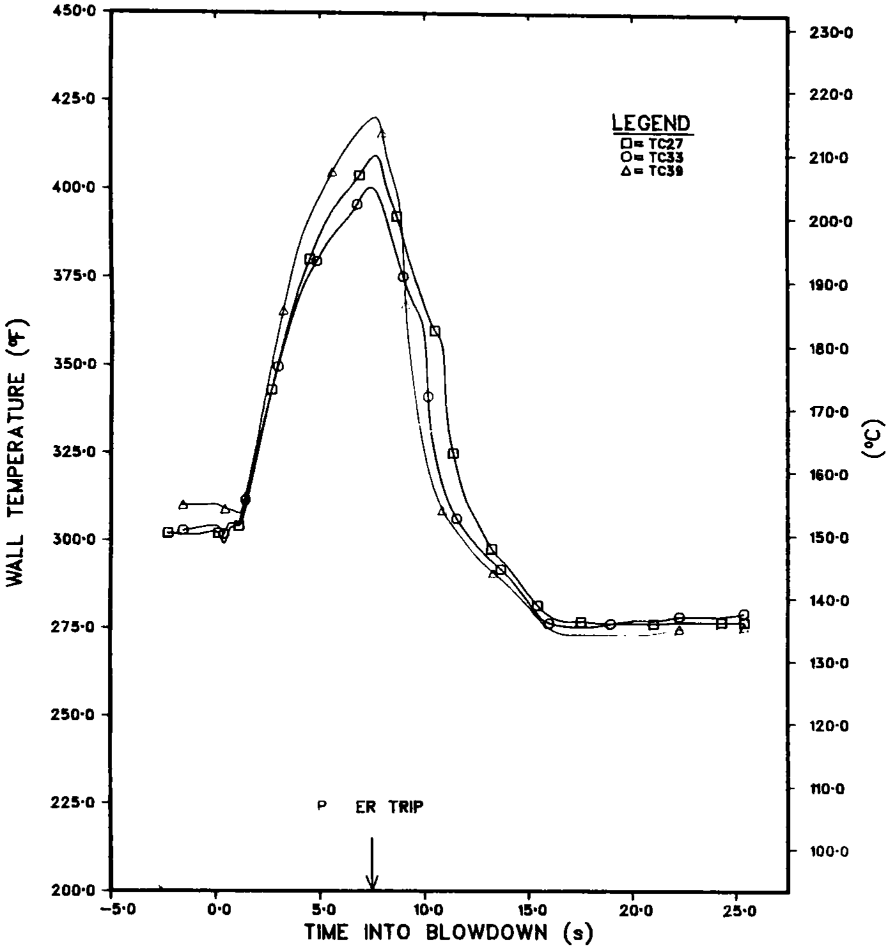

Fig. I.38 (Contd.)

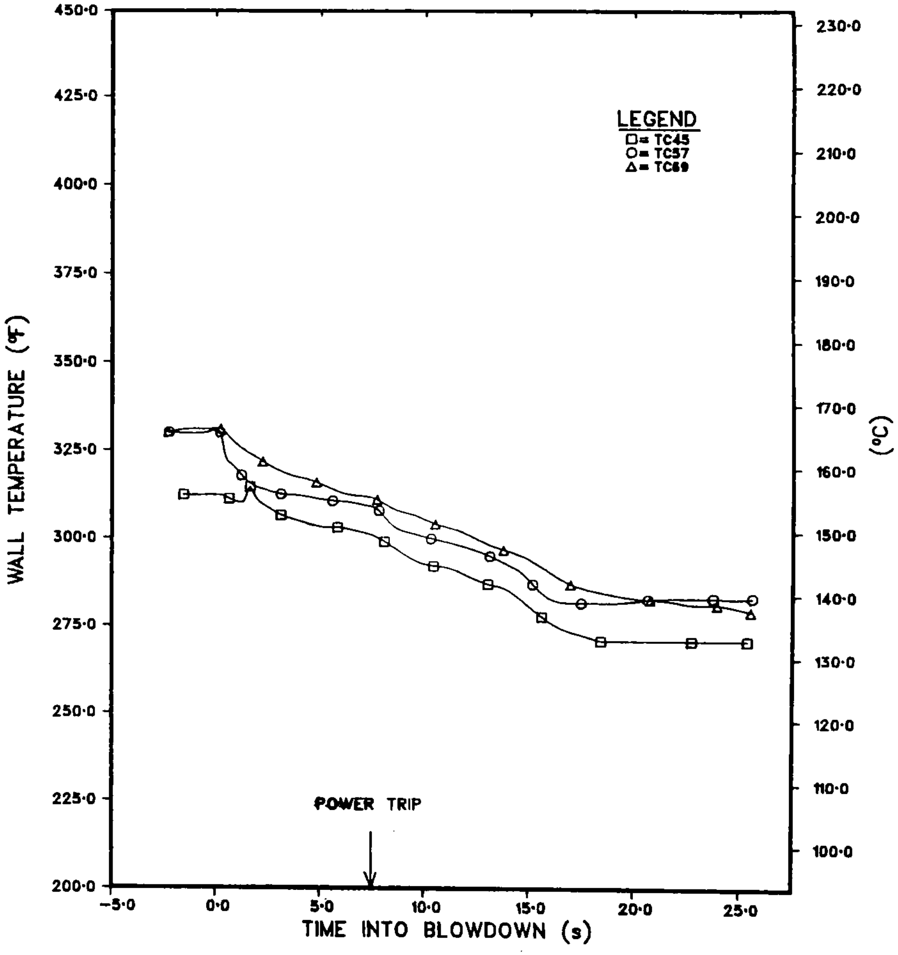

Fig. I.38 (Contd.)

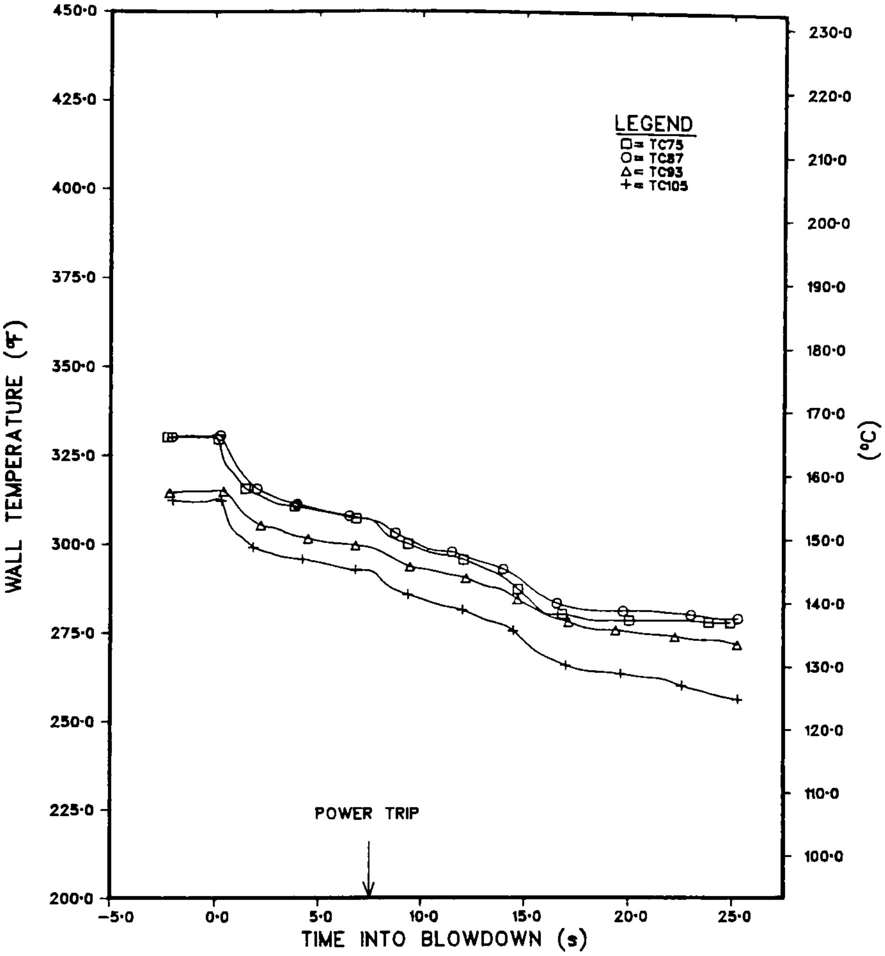

Fig. I.38 (Contd.)

During the transient, the following measurements exhibited similar history in Tests DB-111 and -112:

System pressures (PT1 and PT2)

Pressure differential across the break orifice (DP2)

Lower and upper flowmeters (TV1 and TV2)

Fluid temperatures (TF1 and TF2)

Wall temperatures in the bottom 53 cm.

However, between 53 and 114 cm (21 and 45 in.), the early thermal excursion was delayed considerably in the low-pressure test, DB-111. Upward propagation of the CHF front was observed in this region. In DB-107 and -108, the temperature trip setting was decreased to 193°C, and as a result the peak wall temperatures were lower and the time at power trip occurred earlier. But again, the increased cooling capability of the wall in the aforementioned region is evident in the low-pressure test, DB-107.

The present tests have demonstrated the effect of initial pressure on the time to CHF during the blowdown transient. Similar behavior has been reported in semiscale tests.[11,12] Our preliminary explanation is that the wall, which is in subcooled local boiling, has active nucleation sites that remain active during the early phase of the transient. Therefore cooling capability is ensured in this region simply due to the nucleate-boiling mode of heat transfer in bubbly flow and annular flow. On the other hand, the region that is not in the boiling regime during steady state will mostly rely on liquid, forced, convective heat transfer, principally by heat conduction through the laminar sublayer near the wall, because the nucleation sites have been deactivated. Reactivation of those sites require a large vapor pressure corresponding to high wall temperature.[13] In bubbly flow, the wall in this region can remain cooled because of the high-velocity core flow immediately following reversal.

However, when transition into annular flow occurred, the wall would experience considerable degradation in heat transfer, since the contribution from bubble nucleation is essentially zero and the convective component is small. Therefore the wall-temperature behavior is governed by whether or not the imposed heat flux can be transferred by conduction across the film alone. Figures I.13-I.16 show that the region that was in subcooled boiling experienced continuous cooling during the transient; in fact, the region that was just below the onset of subcooled boiling often experienced rewet and further cooling. Hence the lower-initial-pressure tests promoted a greater region in subcooled boiling and consequently more efficient cooling during blowdown.

With the present break size and blowdown volume, the transient lasted about 25 s. The near depletion of liquid in the channel with the simultaneous occurrence of high-velocity vapor flow was adequately indicated by the two turbine flowrates as an upsurge in flow velocity. This occurred at about 11 s in Test DB-107. At this point, the system pressure started to decay rapidly, resulting in the appearance of the "knee," simply because the volume that was exhausted at the break could only be replenished by the expansion of the two-phase mixture caused by further drop in system pressure.[14]

Within measurement accuracy, the fluid thermocouples indicated saturation temperature during most of the transient, as shown in Figs. I.39-I.42. Considerable superheat was observed after depletion of liquid. The nonequilibrium could be caused by the large amount of stored heat in the upper plenum and the fact that hardly any liquid phase exists to promote local equilibrium.

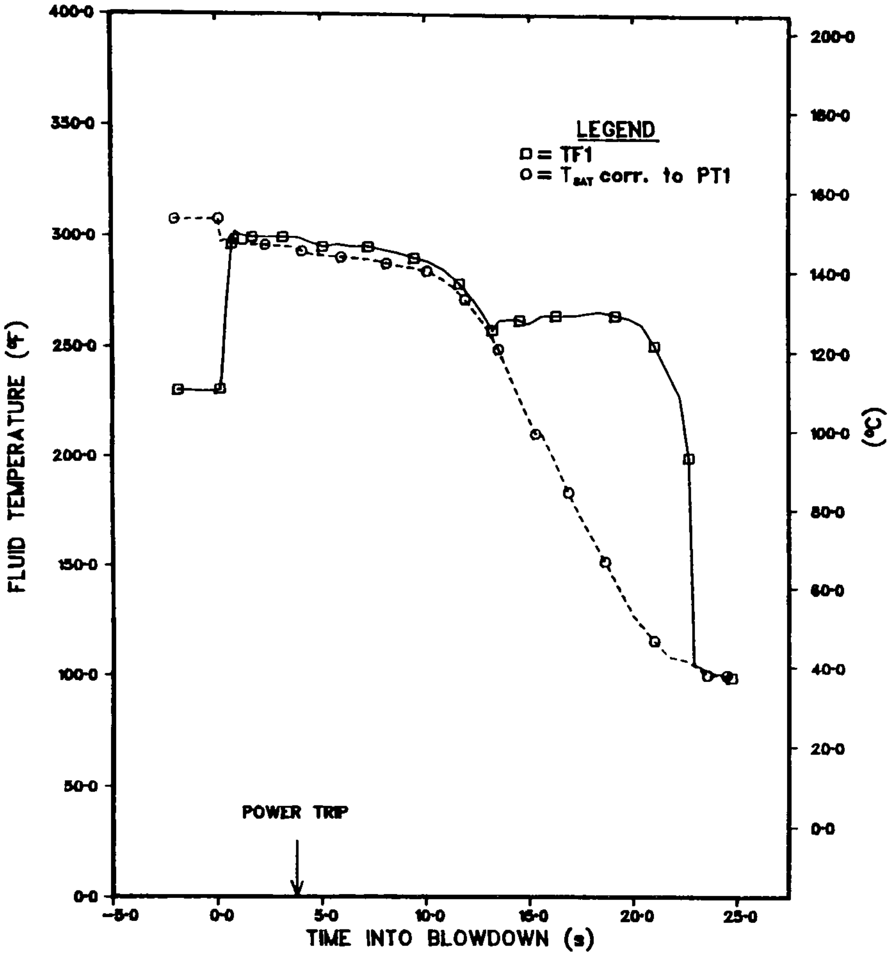

Fig. I.39. System Saturation Temperature during Test DB-107

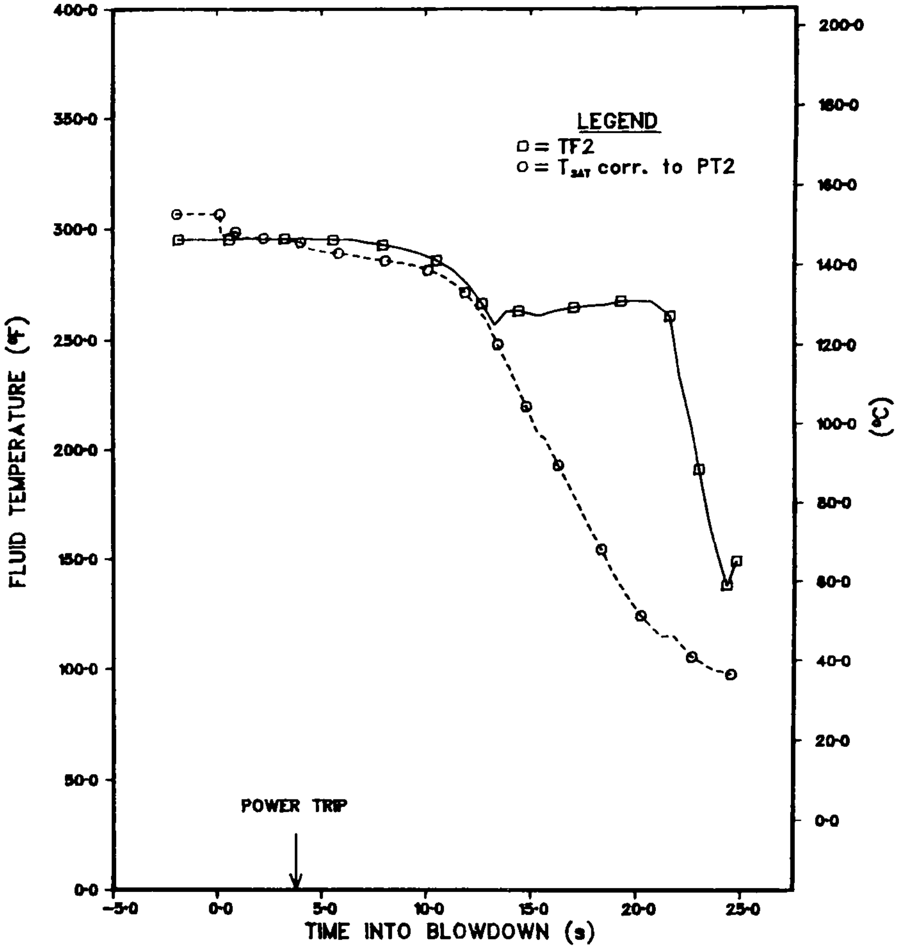

Fig. I.39 (Contd.)

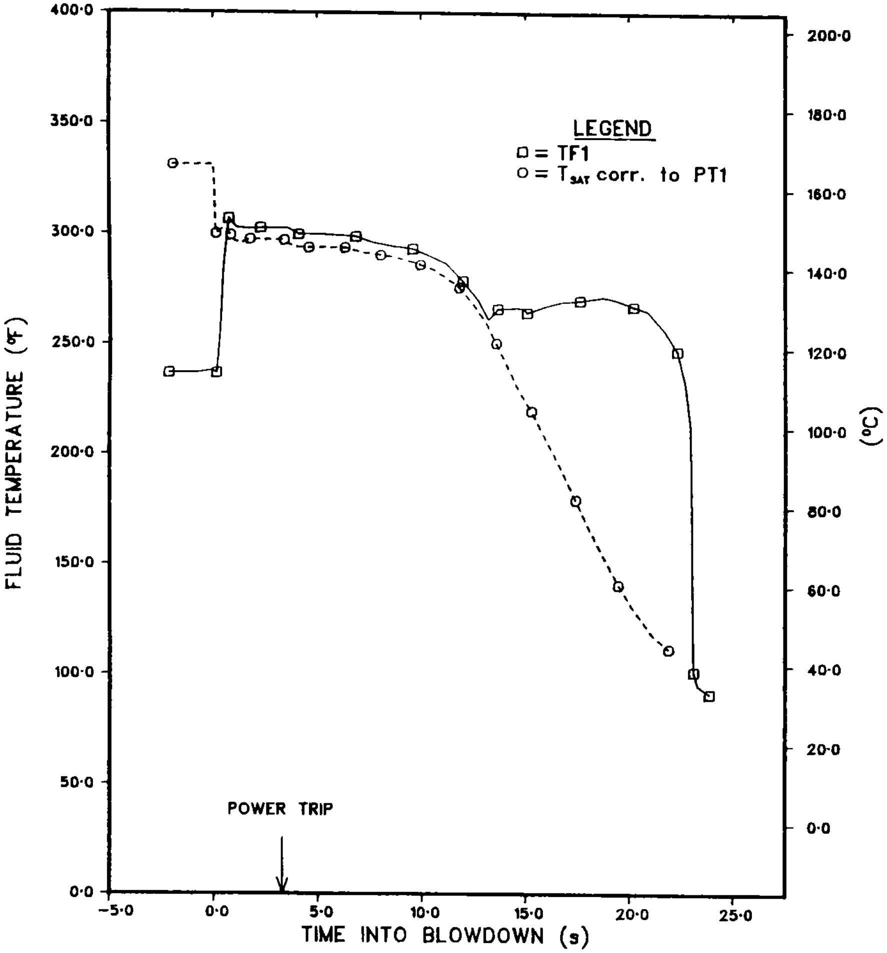

Fig. I.40. System Saturation Temperature during Test DB-108

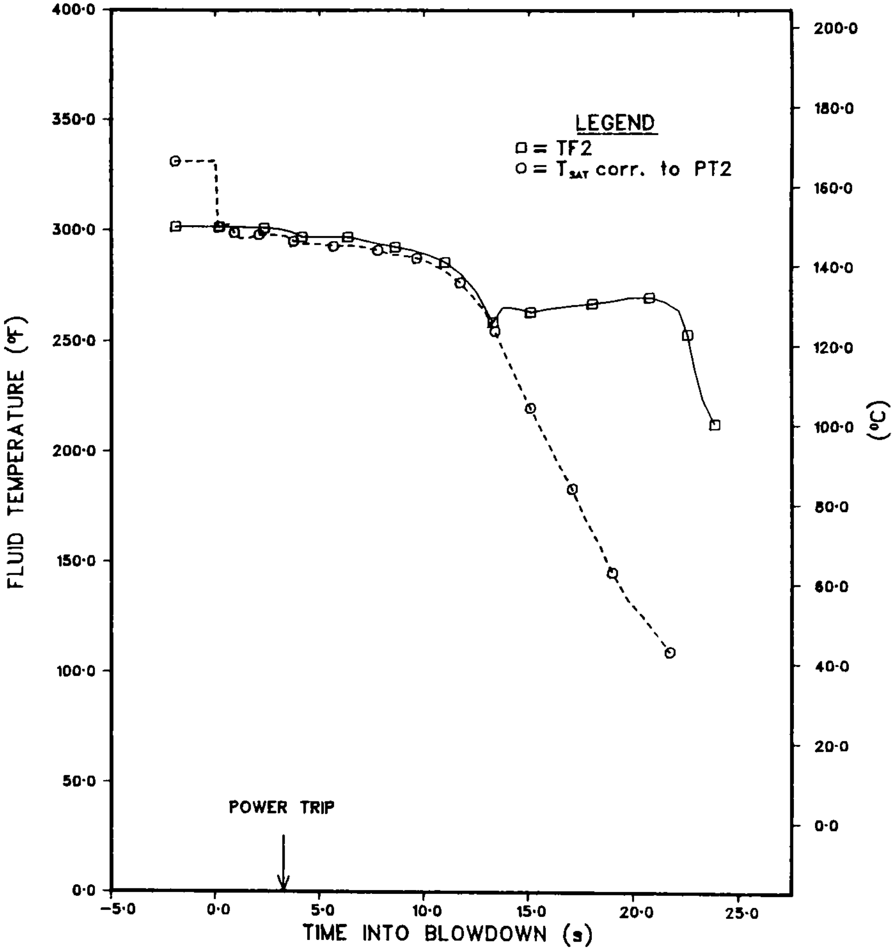

Fig. I.40 (Contd.)

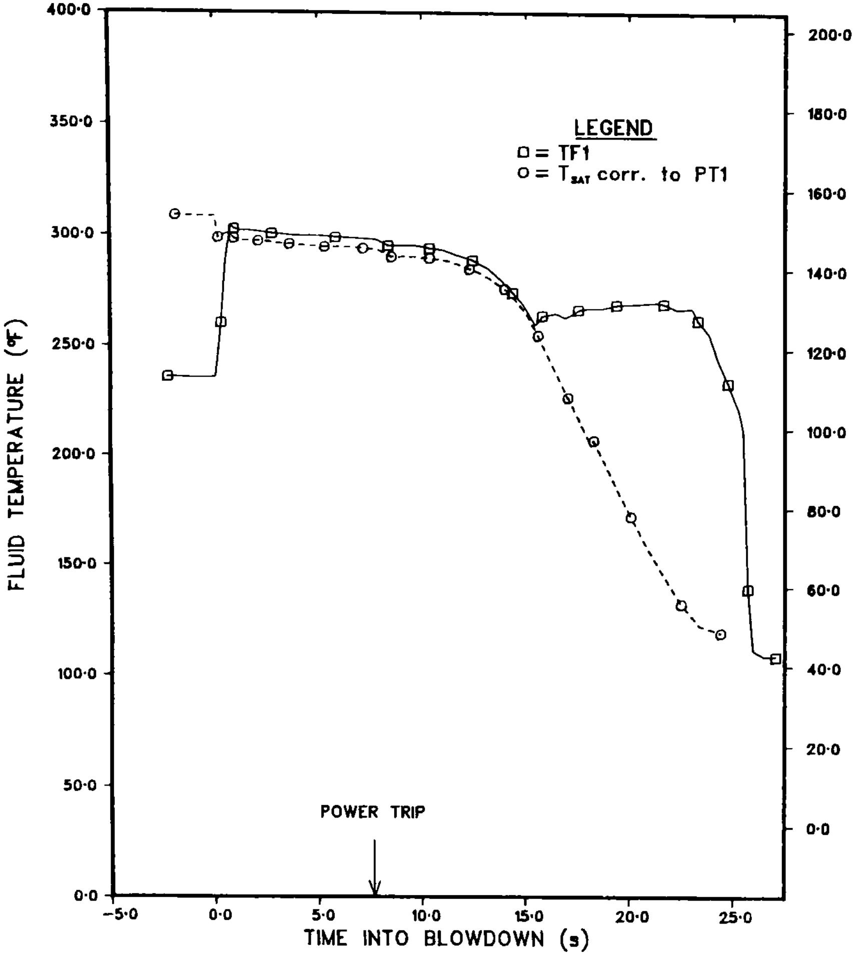

Fig. I.41. System Saturation Temperature during Test DB-111

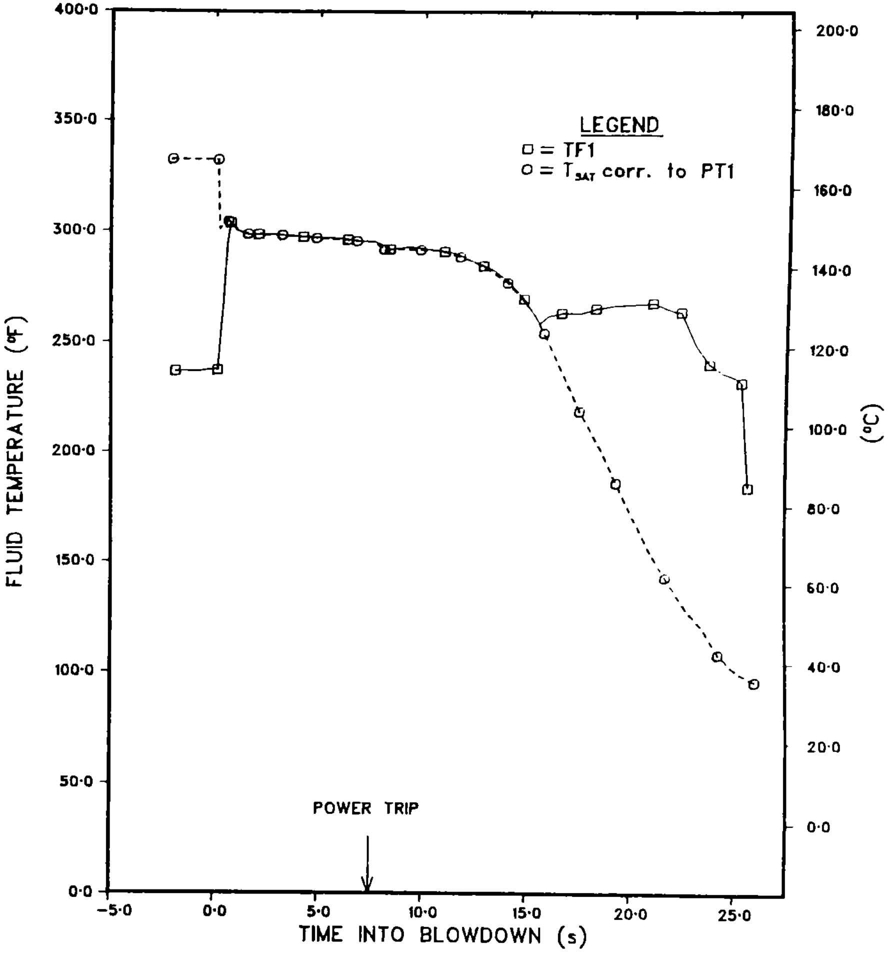

Fig. I.42. System Saturation Temperature during Test DB-112

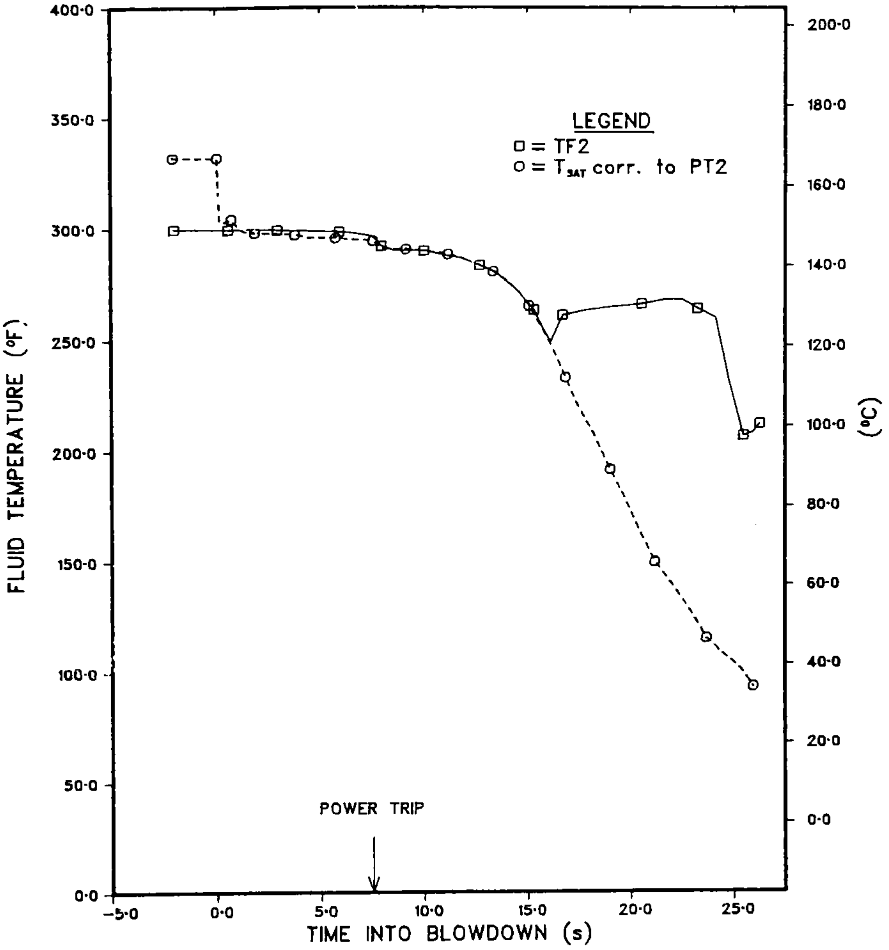

Fig. I.42 (Contd.)

B. Nitrogen-Water Blowdown Tests (Y. S. Cha and R. E. Henry, RAS)

During the blowdown of ECCS accumulators following a Loss-of-Coolant accident, the discharge flow rate and the rate of decompression in the blowdown vessel depend mainly on the discharge geometry, the ambient pressure, and the initial pressure in the vessel. Our experimental results[15] indicated that dissolved gas does not affect the blowdown process significantly unless the system contains a relatively large quantity of internal surface area to provide additional nucleation sites. The blowdown geometry considered here is like that shown in Fig. I.43, which consists of a blowdown vessel, a discharge nozzle, and a long circular duct downstream.

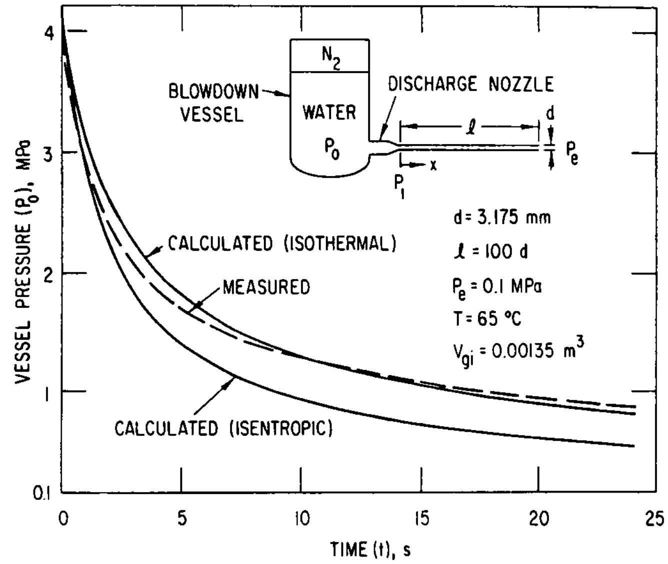

Fig. I.43

Comparison of Measured and Calculated Vessel Pressures during Blowdown Test of Nitrogen-Water System. ANL Neg. No. 900-77-123.

If the diameter of the vessel is much larger than that at the throat of the discharge nozzle, and the liquid is assumed to be incompressible, then the velocity at the throat of the nozzle at any instant is given approximately by

$$U_1 = [2(P_0 - P_1)\nu_\ell]^{1/2}, \tag{7}$$

where

P_0 = pressure in the vessel,

P_1 = pressure at the throat of the nozzle,

and

ν_ℓ = specific volume of liquid.

If we assume that no mass transfer occurred at the liquid-gas interface in the vessel and that the gas volume expands according to the relation

$$P_0\nu_g^n = \text{constant}, \tag{8}$$

where

ν_g = specific volume of gas

and

n = polytropic exponent,

then the following equation can be readily obtained,

$$\frac{dP_0}{dt} = -\frac{AnP_0^{(1+1/n)}U_1}{V_{gi}P_{0i}^{1/n}}, \tag{9}$$

where

t = time,

A = cross-sectional area at the throat of the nozzle,

U_1 = velocity at the throat of the nozzle,

V_{gi} = initial gas volume in the vessel,

and

P_{0i} = initial pressure in the vessel.

The momentum equation in the pipe downstream of the nozzle is

$$\nu_\ell \frac{\partial P}{\partial x} + \frac{f}{2}\frac{U_1^2}{d} + \frac{dU_1}{dt} = 0, \tag{10}$$

where

P = pressure,

x = distance downstream from the nozzle throat,

f = friction factor,

and

d = diameter of the pipe.

If we assume that the flow behavior is quasi-steady ($dU_1/dt \simeq 0$), and the pressure decreases linearly with distance, then Eq. 10 becomes

$$\frac{Pe - P_1}{\ell} + \frac{f(P_0 - P_1)}{d} = 0, \tag{11}$$

where

P_e = exit pressure

and

ℓ = length of the pipe downstream of the nozzle.

If we use the Blasius equation for f,

$$f = 0.3164\mathrm{Re}^{-0.25}, \qquad (12)$$

where

Re = Reynolds number,

then Eqs. 7, 9, 11, and 12, together with the initial conditions,

$$P_0 = P_{0i}, \quad P_1 = P_e \quad \text{at} \quad t = 0, \qquad (13)$$

completely determine the blowdown process. For practical purposes, f can be approximated by $f \simeq 0.015$. If the ambient pressure is much smaller than the vessel pressure, then Eq. 9 can be integrated directly, which results in an algebraic equation for P_0,

$$P_0 = P_{0i}\left[1 + \frac{A(2+n)\left[\dfrac{2\nu_\ell P_{0i}}{1 + 0.015\ell/d}\right]^{1/2} t}{2V_{gi}}\right]^{-2n/(2+n)} . \qquad (14)$$

Figure I.43 compares the calculated and measured vessel pressures during a blowdown test of a nitrogen-water system. The results shown in Fig. I.43 indicate that the gas initially expands isentropically. Shortly afterward, the expansion of the gas moves gradually from an isentropic process toward an isothermal process. Similar results were observed for tests with larger pipe diameter (d = 4.763 mm) and for tests without the long pipe downstream of the nozzle ($\ell = 0$).[16] Numerical solution of Eqs. 9 and 10 indicated that dU_1/dt is indeed small compared to the other two terms in Eq. 10, and experimental results indicated that the pressure gradient is indeed constant in the pipe downstream of the nozzle for 1.48 MPa $\le P_{0i} \le$ 4.24 MPa and P_e = 0.1 MPa.[16] Thus, the simple model described here is able to predict the blowdown-vessel pressure as accurately as one can assess the polytropic behavior of the initial gas volume. For design and safety analyses, an assumption of isothermal behavior appears to be an excellent engineering approximation.

C. One-dimensional Drift-flux Modeling: One-dimensional Drift Velocity of Bubbly, Droplet, Annular, and Annular Mist Flows in Confined Channel
(M. Ishii, RAS)

1. One-dimensional Drift-flux Model

It has long been realized that the cross-sectional area averaging is very useful for complicated engineering problems involving fluid flow and heat transfer, since field equations can be reduced to quasi-one-dimensional forms. By area averaging, the information on changes of variables in the direction normal to the main flow within a channel is basically lost; therefore, the transfer of momentum and energy between the wall and the fluid should be expressed by empirical correlations or by simplified models. The rational approach to obtain a one-dimensional model is to integrate the three-dimensional model over a cross-sectional area to introduce proper mean values.

A simple area average over the cross-sectional area A is defined by

$$\langle F \rangle = \frac{1}{A} \int_A F \, dA, \tag{15}$$

and the void fraction weighted mean values is given by

$$\langle\langle F_k \rangle\rangle = \langle \alpha_k F_k \rangle / \langle \alpha_k \rangle. \tag{16}$$

In the subsequent analysis, the density of each phase ρ_d and ρ_c within any cross-sectional area is considered to be uniform such that $\rho_k = \langle\langle \rho_k \rangle\rangle$. For most of the practical two-phase flow problems, this assumption is valid, since the transverse pressure gradient within a channel is relatively small. The detailed analysis without this approximation appears in Ref. 16. Under the above simplifying assumption, the average mixture density is given by

$$\langle \rho_m \rangle \equiv \langle \alpha_d \rangle \rho_d + (1 - \langle \alpha_d \rangle) \rho_c. \tag{17}$$

The axial component of the weighted mean velocity of k phase is

$$\langle\langle v_k \rangle\rangle = \frac{\langle \alpha_k v_k \rangle}{\langle \alpha_k \rangle} = \frac{\langle j_k \rangle}{\langle \alpha_k \rangle}, \tag{18}$$

where the scalar expression of the velocity corresponds to the axial component of the vector. Then the mixture velocity is defined by

$$\bar{v}_m \equiv \frac{\langle \rho_m v_m \rangle}{\langle \rho_m \rangle} = [\langle \alpha_d \rangle \rho_d \langle\langle v_d \rangle\rangle + (1 - \langle \alpha_d \rangle) \rho_c \langle\langle v_c \rangle\rangle] / \langle \rho_m \rangle, \tag{19}$$

and the volumetric flux is given by

$$\langle j \rangle \equiv \langle j_d \rangle + \langle j_c \rangle = \langle \alpha_d \rangle \langle\!\langle v_d \rangle\!\rangle + (1 - \langle \alpha_d \rangle) \langle\!\langle v_c \rangle\!\rangle.$$

The mean mixture enthalpy also should be weighted by the density. Thus we have

$$\bar{h}_m \equiv \frac{\langle \rho_m h_m \rangle}{\langle \rho_m \rangle} = [\langle \alpha_d \rangle \rho_d \langle\!\langle h_d \rangle\!\rangle + (1 - \langle \alpha_d \rangle) \rho_c \langle\!\langle h_c \rangle\!\rangle] / \langle \rho_m \rangle. \tag{21}$$

The appropriate mean drift velocity is defined by

$$\bar{V}_{dj} \equiv \langle\!\langle v_d \rangle\!\rangle - \langle j \rangle = (1 - \langle \alpha_d \rangle)(\langle\!\langle v_d \rangle\!\rangle - \langle\!\langle v_c \rangle\!\rangle). \tag{22}$$

The experimental determination of the above-defined drift velocity is possible if the volume flow rate of each phase, Q_k, and the mean void fraction, $\langle \alpha_d \rangle$, are measured. This is because Eq. 22 can be transformed into

$$\bar{V}_{dj} = \frac{\langle j_d \rangle}{\langle \alpha_d \rangle} - (\langle j_d \rangle + \langle j_c \rangle), \tag{23}$$

where $\langle j_k \rangle$ is given by $\langle j_k \rangle = Q_k / A$. Furthermore, the present definition of the drift velocity can also be used for annular two-phase flows. Under the definitions of various velocity fields, we obtain several important relations such as

$$\left.\begin{aligned} \langle\!\langle v_d \rangle\!\rangle &= \bar{v}_m + \frac{\rho_c}{\langle \rho_m \rangle} \bar{V}_{dj}, \\ \langle\!\langle v_c \rangle\!\rangle &= \bar{v}_m - \frac{\langle \alpha_d \rangle}{1 - \langle \alpha_d \rangle} \frac{\rho_d}{\langle \rho_m \rangle} \bar{V}_{dj}, \end{aligned}\right\} \tag{24}$$

and

$$\langle j \rangle = \bar{v}_m + \frac{\langle \alpha_d \rangle (\rho_c - \rho_d)}{\langle \rho_m \rangle} \bar{V}_{dj}. \tag{25}$$

In the drift-flux formulation, a problem is solved for $\langle \alpha_d \rangle$ and $\bar{v}_m$ with a given constitutive relation for $\bar{V}_{dj}$. Thus Eq. 24 can be used to recover a solution for the velocity of each phase after a problem is solved.

By area averaging the three-dimensional field equations,[17] and using the various mean values we obtain the following:

Mixture-continuity Equation

$$\frac{\partial\langle\rho_m\rangle}{\partial t} + \frac{\partial}{\partial z}(\langle\rho_m\rangle\overline{v}_m) = 0. \tag{26}$$

Continuity Equation for Dispersed Phase

$$\frac{\partial\langle\alpha_d\rangle\rho_d}{\partial t} + \frac{\partial}{\partial z}(\langle\alpha_d\rangle\rho_d\overline{v}_m) = \langle\Gamma_d\rangle - \frac{\partial}{\partial z}\left(\frac{\langle\alpha_d\rangle\rho_d\rho_c}{\langle\rho_m\rangle}\overline{V}_{dj}\right). \tag{27}$$

Mixture-momentum Equation

$$\begin{aligned}\frac{\partial\langle\rho_m\rangle\overline{v}_m}{\partial t} + \frac{\partial}{\partial z}(\langle\rho_m\rangle\overline{v}_m^2) &= -\frac{\partial}{\partial z}\langle p_m\rangle + \frac{\partial}{\partial z}\langle\tau_{zz} + \tau_{zz}^T\rangle - \langle\rho_m\rangle g_z \\ &\quad - \frac{f_m}{2D}\langle\rho_m\rangle\overline{v}_m|\overline{v}_m| - \frac{\partial}{\partial z}\left[\frac{\langle\alpha_d\rangle\rho_d\rho_c}{(1-\langle\alpha_d\rangle)\langle\rho_m\rangle}\overline{V}_{dj}^2\right] \\ &\quad - \frac{\partial}{\partial z}\sum_k \mathrm{COV}(\alpha_k\rho_k v_k v_k).\end{aligned} \tag{28}$$

Mixture-enthalpy-energy Equation

$$\begin{aligned}\frac{\partial\langle\rho_m\rangle\overline{h}_m}{\partial t} + \frac{\partial}{\partial z}(\langle\rho_m\rangle\overline{h}_m\overline{v}_m) &= -\frac{\partial}{\partial z}\langle q + q^T\rangle + \frac{q''_w\xi_h}{A} - \frac{\partial}{\partial z}\left(\frac{\langle\alpha_d\rangle\rho_d\rho_c}{\langle\rho_m\rangle}\Delta h_{dc}\overline{V}_{dj}\right) \\ &\quad - \frac{\partial}{\partial z}\sum_k \mathrm{COV}(\alpha_k\rho_k h_k v_k) + \frac{\partial\langle p_m\rangle}{\partial t} \\ &\quad + \left[\overline{v}_m + \frac{\langle\alpha_d\rangle(\rho_c - \rho_d)}{\langle\rho_m\rangle}\overline{V}_{dj}\right]\frac{\partial\langle p_m\rangle}{\partial z} + \langle\Phi_m^\mu\rangle.\end{aligned} \tag{29}$$

Here $\tau_{zz} + \tau_{zz}^T$ denotes the normal components of the stress tensor in the axial direction and Δh_{dc} is the enthalpy difference between phases; thus, $\Delta h_{dc} = \langle\langle h_d\rangle\rangle - \langle\langle h_c\rangle\rangle$. The covariance terms represent the difference between the average of a product and the product of the average of two variables such that $\mathrm{COV}(\alpha_k\rho_k\psi_k v_k) \equiv \langle\alpha_k\rho_k\psi_k(v_k - \langle\langle v_k\rangle\rangle)\rangle$. If the profile of either ψ_k or v_k is flat, then the covariance term reduces to zero. For most of the dispersed two-phase flows in a turbulent-flow regime, the effects of the covariance terms are small and may be neglected as a first-order approximation. The term represented by $f_m\langle\rho_m\rangle\overline{v}_m|\overline{v}_m|/(2D)$ in Eq. 28 is the two-phase frictional

pressure drop. We note here that the effects of the mass, momentum, and energy diffusions associated with the relative motion between phases appear explicitly in the drift-flux formulation, since the convective terms on the left-hand side of the field equations are expressed in terms of the mixture velocity. These effects of diffusions in the present formulation are expressed in terms of the drift velocity of the dispersed phase $\overline{V}_{dj}$. In the drift-flux formulation, this drift velocity should be specified by a kinematic constitutive equation. The kinematic constitutive equation may be formulated in a functional form as

$$\overline{V}_{dj} = \overline{V}_{dj}(\langle\alpha_d\rangle, \langle\rho_m\rangle, g_z, \overline{v}_m, \text{etc.}). \tag{30}$$

This constitutive equation replaces one of the phase-momentum equations of the two-fluid model formulation. To take into account the mass transfer across the interfaces, a consitutive equation for $\langle\Gamma_d\rangle$ should also be given. In a functional form, this phase-change constitutive equation may be written as

$$\langle\Gamma_d\rangle = \langle\Gamma_d\rangle\left(\langle\alpha_d\rangle, \langle p_m\rangle, \overline{v}_m, \frac{\partial\langle p_m\rangle}{\partial t}, \text{etc.}\right). \tag{31}$$

The above formulation can be extended to nondispersed two-phase flows such as an annular flow, provided a proper constitutive relation for a drift velocity of one of the phases is given.

2. Dispersed Two-phase Flow

To obtain a kinematic constitutive equation for the one-dimensional drift-flux model, the local drift velocity must be averaged over the channel cross section. The constitutive relation for the local drift velocity in a confined channel has been developed.[18] Now we shall relate this V_{dj} to the mean drift velocity $\overline{V}_{dj}$ defined by Eq. 22.

From Eqs. 16 and 22, we have

$$\overline{V}_{dj} = \left\langle \frac{\alpha_d(j + V_{dj})}{\langle\alpha_d\rangle} - j \right\rangle = \langle\langle V_{dj}\rangle\rangle + (C_0 - 1)\langle j\rangle, \tag{32}$$

where

$$\langle\langle V_{dj}\rangle\rangle \equiv \langle\alpha_d V_{dj}\rangle/\langle\alpha_d\rangle \tag{33}$$

and

$$C_0 \equiv \frac{\langle\alpha_d j\rangle}{\langle\alpha_d\rangle\langle j\rangle}. \tag{34}$$

The second term on the right-hand side of Eq. 32 is a covariance between the concentration profile and the volumetric flux profile; thus it can also be expressed as $\mathrm{COV}(\alpha_d j)/\langle\alpha_d\rangle$. The factor C_0 has been used for bubbly or slug flows by several authors,[19-21] and it is known as a distribution parameter. The inverse of this parameter was also used in the early work of Bankoff.[22] Physically, this effect arises from the fact that the dispersed phase is locally transported with the drift velocity V_{dj} with respect to local volumetric flux j and not with respect to the average volumetric flux $\langle j\rangle$. For example, if the dispersed phase is more concentrated in the higher flux region, then the mean transport of the dispersed phase is promoted by higher local j.

The value of C_0 can be determined from assumed profiles of the void fraction α_d and total volumetric flux j,[21] or from experimental data.[23] By assuming power-law profiles in a pipe for j and α_d, we have

$$\left.\begin{aligned} j/j_0 &= 1 - (R/R_W)^m \\ &\text{and} \\ \frac{\alpha_d - \alpha_{dW}}{\alpha_{d0} - \alpha_{dW}} &= 1 - (R/R_W)^n \end{aligned}\right\}, \tag{35}$$

where j_0, α_{d0}, α_{dW}, R, and R_W are, respectively, the value of j and α at the center, the void fraction at the wall, the radial distance, and the radius of a pipe. By substituting these profiles into the definition of C_0 given by Eq. 34, we obtain

$$C_0 = 1 + \frac{2}{m + n + 2}\left(1 - \frac{\alpha_{dW}}{\langle\alpha_d\rangle}\right). \tag{36}$$

A further discussion on the distribution parameter based on the above assumed profiles appears in Ref. 23.

Now Eq. 32 can be transformed to

$$\langle\langle v_d\rangle\rangle = \frac{\langle j_d\rangle}{\langle\alpha_d\rangle} = C_0\langle j\rangle + \langle\langle V_{dj}\rangle\rangle, \tag{37}$$

where $\langle\langle v_d\rangle\rangle$ and $\langle j\rangle$ are easily obtainable parameters in experiments, particularly under an adiabatic condition. Therefore, this equation suggests a plot of the mean velocity $\langle\langle v_d\rangle\rangle$ versus the average volumetric flux $\langle j\rangle$. Figures I.44-I.50 show various experimental data using this mean velocity-flux plane. Note that if the concentration profile is uniform across the channel, then the value of the distribution parameter is equal to unity. In addition, if the effect of the local drift $\langle\langle V_{dj}\rangle\rangle$ is negligibly small, then the flow becomes essentially

homogeneous. In this case, the relation between the mean velocity and flux reduces to a straight line through the origin having an angle of 45°. The deviation of the experimental data from this homogeneous flow line shows the magnitude of the drift of the dispersed phase with respect to the volume center of the mixture.

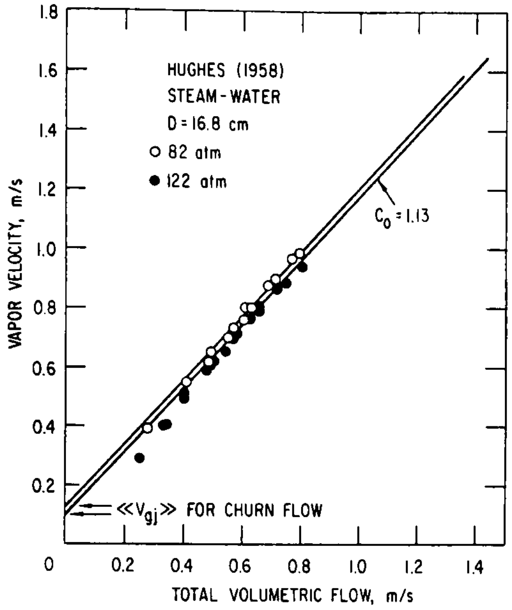

Fig. I.44. Experimental Data for High-pressure System, from Hughes.[24] ANL Neg. No. 900-77-187.

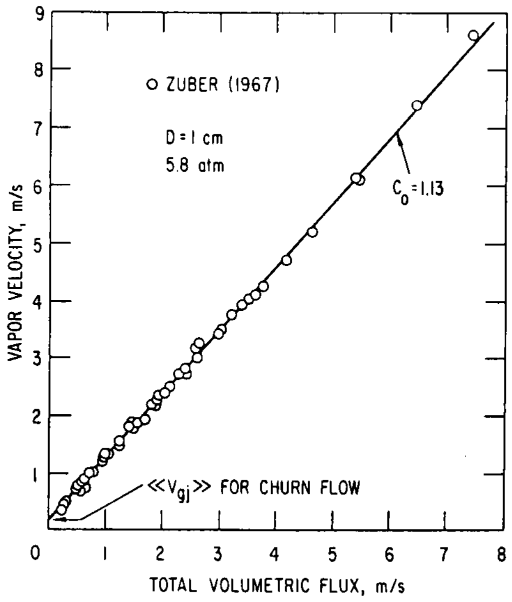

Fig. I.45. Freon-22 Data in Boiling Flow, from Zuber et al.[23] ANL Neg. No. 900-77-181.

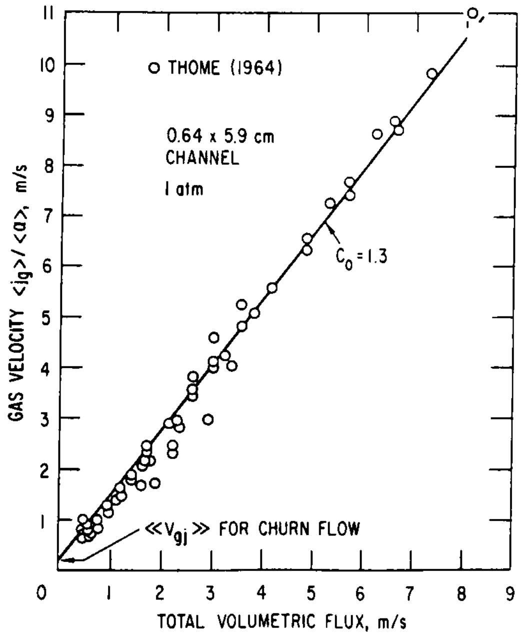

Fig. I.46. Fully Developed Nitrogen-NaK Flow Data, from Thome.[25] ANL Neg. No. 900-77-177.

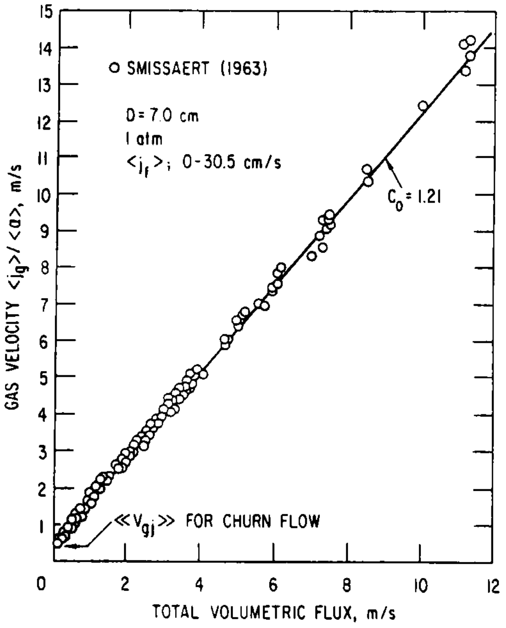

Fig. I.47. Fully Developed Air-Water Flow Data, from Smissaert.[26] ANL Neg. No. 900-77-182.

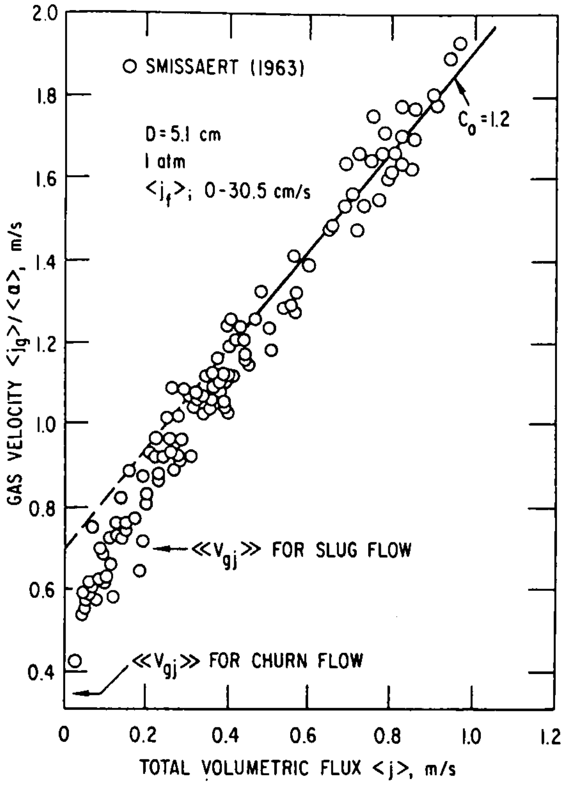

Fig. I.48. Fully Developed Nitrogen-Mercury Flow Data, from Smissaert.[26] ANL Neg. No. 900-77-176.

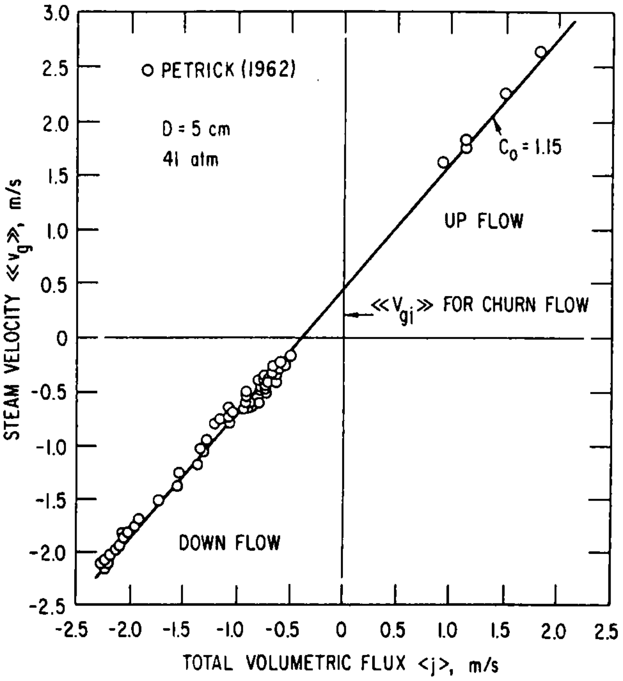

Fig. I.49. Experimental Data for Cocurrent Upflow and Cocurrent Downflow of Steam-Water System, from Petrick.[27] ANL Neg. No. 900-77-180 Rev. 1.

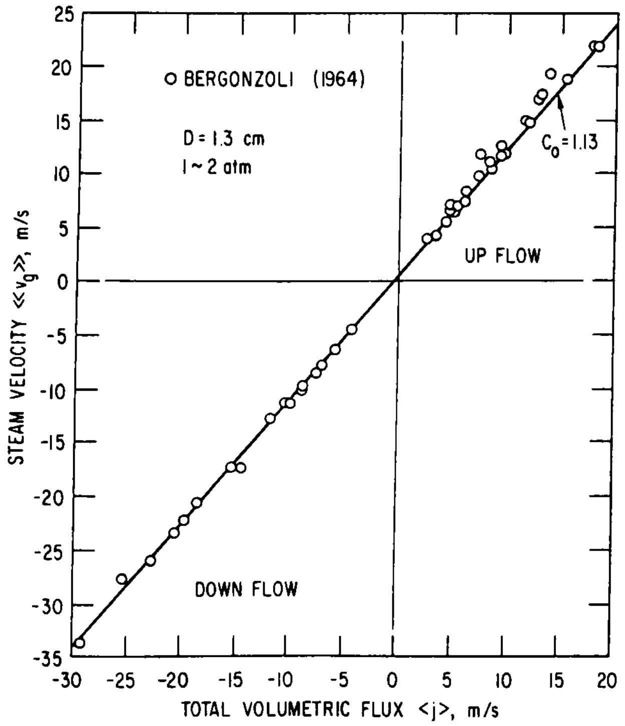

Fig. I.50

Experimental Data for Cocurrent Upflow and Cocurrent Downflow of Heated Santowax-R System, from Bergonzoli and Halfen.[28] ANL Neg. No. 900-77-185.

An important characteristic of such a plot is that, for two-phase flow regimes with fully developed void and velocity profiles, the data points cluster around a straight line, as shown in Figs. I.44-I.50. This trend is particularly pronounced when the local drift velocity is constant or negligibly small. Hence, for a given flow regime, the value of the distribution parameter C_0 may be obtained from the slope of these lines, whereas the intercept of this line with the mean velocity axis can be interpreted as the weighted mean local drift velocity, $\langle\langle V_{dj} \rangle\rangle$. The extensive study by Zuber et al.[23] shows that C_0 depends on pressure, channel geometry, and perhaps flow rate. Also, an important effect of subcooled boiling and developing void profile on the distribution parameter has been noted by Hancox and Nicoll.[29]

In the present study, a simple correlation for the distribution parameter in the bubbly-flow regime has been developed along the above studies. First, by considering a fully developed bubbly flow, we assumed that C_0 depends on the density ratio, ρ_g/ρ_f, and the Reynolds number based on liquid properties, GD/μ_f, where G, D, and μ_f are the total mass flow rate, hydraulic diameter, and the viscosity of the liquid, respectively. Hence,

$$C_0 = C_0\left(\frac{\rho_g}{\rho_f}, \frac{GD}{\mu_f}\right). \tag{38}$$

A single-phase turbulent-flow profile and the ratio of the maximum velocity to mean velocity gives a theoretical limiting value of C_0 at $\alpha \rightarrow 0$ and $\rho_g/\rho_f \rightarrow 0$, since in this case all the bubble should be concentrated at the central region. Thus, from the experimental data of Nikuradse[30] for a round tube, we have

$$C_0 \rightarrow C_\infty = 1.3926 - 0.0155 \ln \frac{GD}{\mu_f} \tag{39}$$

as $\alpha \rightarrow 0$ and $\rho_g/\rho_f \rightarrow 0$ (see Fig. I.51). On the other hand, as the density ratio approaches the unity, the distribution parameter C_0 should also become unity. Thus

$$C_0 \rightarrow 1 \quad (\text{as } \rho_g/\rho_f \rightarrow 1). \tag{40}$$

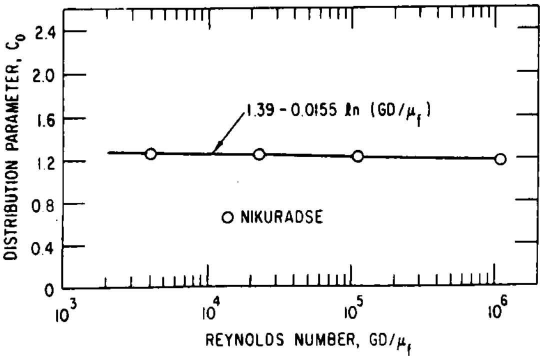

Fig. I.51

Limiting Value of Distribution Parameter C_0 at Zero Void Fraction and $\rho_g/\rho_f \rightarrow 0$ Based on Single-phase Turbulent-flow Profile, from Nikuradse.[30] ANL Neg. No. 900-77-178.

Based on these limits and from various experimental data in a fully developed flow, the distribution parameter can be given approximately by

$$C_0 = C_\infty - (C_\infty - 1)\sqrt{\rho_g/\rho_f}, \tag{41}$$

where the density group scales the inertia effects of each phase in transverse void distribution. Physically, Eq. 41 models the tendency of the lighter phase to migrate into a higher-velocity regime and thus result in a higher void concentration in the central regime.[22]

Over a wide range of Reynolds number, GD/μ_f, Eq. 39 can be approximated by $C_\infty \simeq 1.2$ for a flow in a round tube. On the other hand, for a rectangular channel, the experimental data show this value to be about 1.35. Thus, for a fully developed turbulent bubbly flow, we have

$$C_0 \simeq \begin{cases} 1.2 - 0.2\sqrt{\rho_g/\rho_f}: & \text{round tube;} \\ \\ 1.35 - 0.35\sqrt{\rho_g/\rho_f}: & \text{rectangular channel.} \end{cases} \tag{42}$$

Figures I.52 and I.53 compare the above correlation with various experimental data. Note here that each point in the figures represents anywhere from five to 150 data. For example, the original experimental data of Smissaert[26] shown in Fig. I.47 are presented by a single point in Fig. I.52. It is evident that each

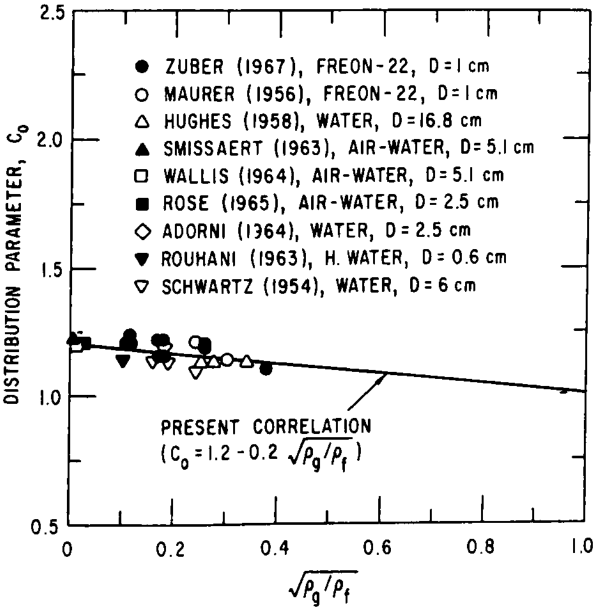

Fig. I.52. Distribution Parameter for Fully Developed Flow in Round Tube. ANL Neg. No. 900-77-173.

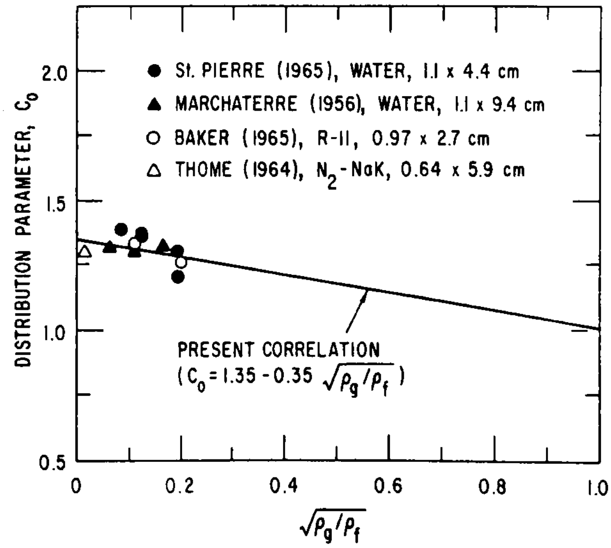

Fig. I.53. Distribution Parameter for Fully Developed Flow in Rectangular Channel. ANL Neg. No. 900-77-184.

point in Fig. I.47 can be used to obtain a corresponding value for C_0 by using the existing correlation for the mean local drift velocity $\langle\langle V_{dj}\rangle\rangle$. However, in view of the strong linear relation between the mean velocity of dispersed phase and the total flux, the average C_0 value obtained by linear fitting has been used in Figs. I.52 and I.53.

In the velocity-flux plane (Figs. I.49 and I.50), three operational modes can be easily identified. In the first quadrant, the flow is basically cocurrent upward; therefore both the liquid and vapor phase flow in upward direction. The examples of this mode are shown in Figs. I.44-I.48. In the second quadrant, the vapor phase is moving upward; however, there is a net downward flow of mixture. Consequently, the flow is countercurrent. The cocurrent downflow operation should appear in the third quadrant of the velocity-flux plane, as shown in Figs. I.49 and I.50. These data indicate that the basic characteristic described by Eq. 37 is valid for both cocurrent up and down flows with an identical value for the distribution parameter C_0. This fact demonstrates the usefulness of correlating the drift velocity in terms of the mean local drift velocity, $\langle\langle V_{dj}\rangle\rangle$, and C_0.

In two-phase systems with heat addition, the change of void profiles from concave to convex can occur as illustrated in Figs. I.54 and I.55. The concave void-fraction profile is caused by the wall nucleation and delayed transverse migration of bubbles toward the center of a channel. Under these conditions, most of the bubbles are initially located near the nucleating wall. The concave profile is particularly pronounced in the subcooled boiling regime, because here only the wall boundary layer is heated above the saturation temperature and the core liquid is subcooled. This temperature profile will induce collapses of migrating bubbles in the core region and resulting latent heat transport from the wall to the subcooled liquid. However, a similar concave profile can also be obtained by injecting gas into liquid flow through porous tube wall.[33]

In the region where voids are still concentrated close to the wall, the mean velocity of vapour can be smaller than the mean velocity of liquid, because the bulk of liquid moves with the high core velocity. Hence, in this region, the data should fall below the line for a fully developed two-phase flow. This is illustrated in Figs. I.56-I.58. If the data fall below the homogeneous line, the value of C_0 should be less than unity. However, as more and more vapour is generated along the channel, the void-fraction profile changes from concave to convex and becomes fully developed. This trend can easily be seen in Figs. I.56-I.58, where the data approach the fully developed flow line from below in the bulk boiling regime.

For a flow with generation of void at the wall due to either nucleation or gas injection, the distribution parameter C_0 should have a near-zero value at the beginning of the two-phase flow region. This can also be seen from the definition of C_0 in Eq. 34. Hence we have

$$\lim_{\langle\alpha\rangle\to 0} C_0 \to 0 \quad \text{for} \quad \Gamma_g > 0. \tag{43}$$

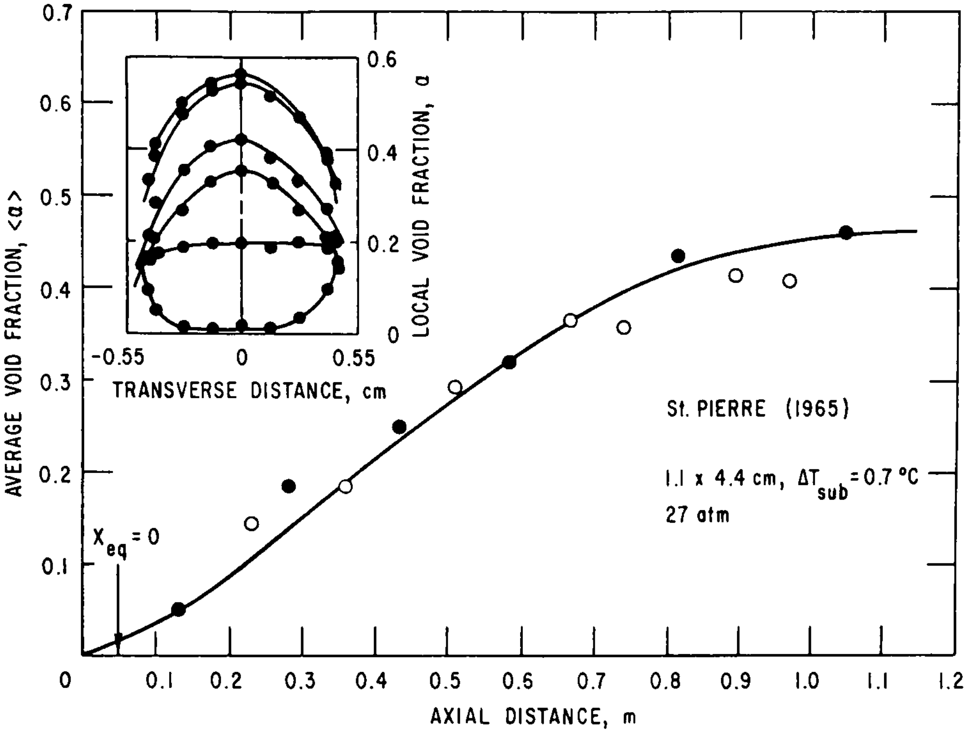

Fig. I.54. Axial Void Distribution with Corresponding Void Profiles at Various Stations for Steam-Water Experiment in Rectangular Channel, from St. Pierre.[37] ANL Neg. No. 900-77-172.

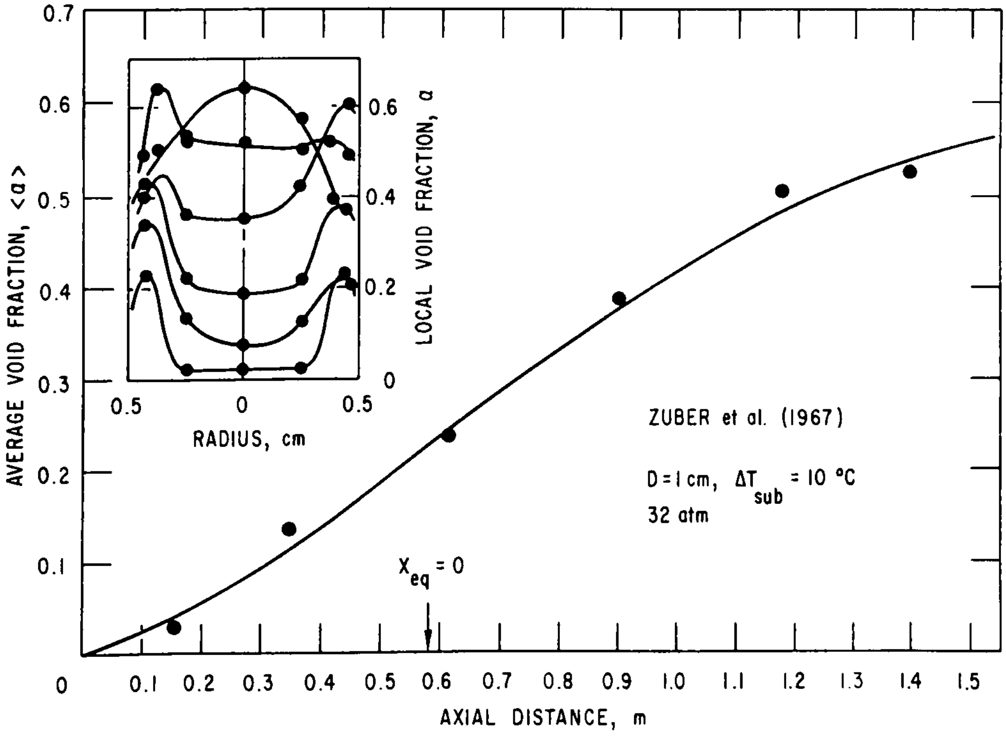

Fig. I.55. Axial Void Distribution with Corresponding Void Profiles at Various Stations for Freon-22 Experiment in Round Tube, from Zuber et al.[23] ANL Neg. No. 900-77-183.

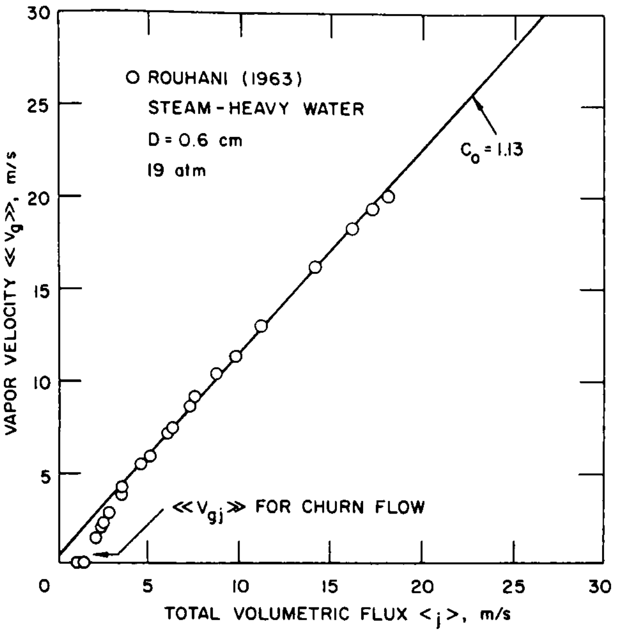

Fig. I.56. Experimental Data of Rouhani and Becker[35] in Round Tube and Effect of Developing Flow due to Boiling. ANL Neg. No. 900-77-179.

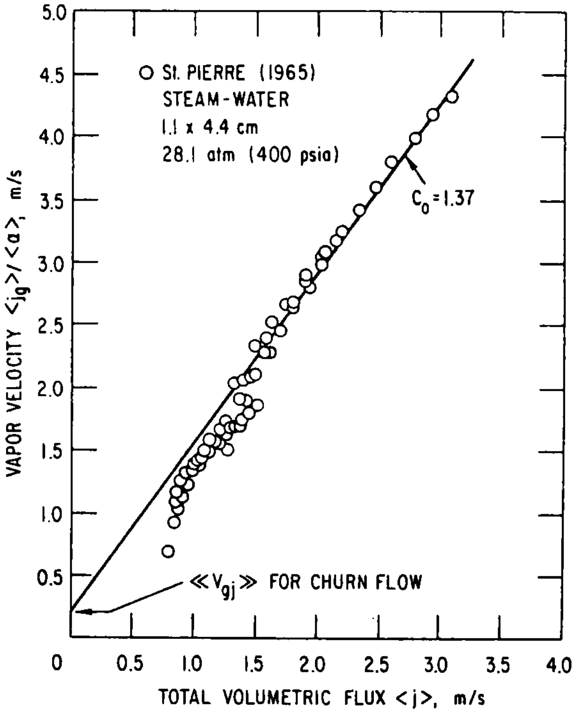

Fig. I.57. Experimental Data of St. Pierre[37] in Rectangular Flow and Effect of Developing Flow due to Boiling. ANL Neg. No. 900-77-174.

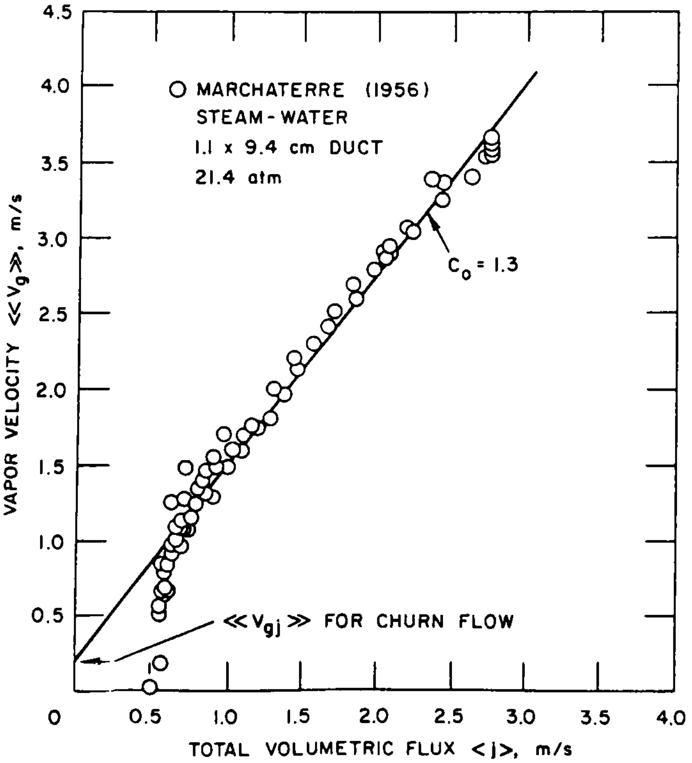

Fig. I.58

Experimental Data of Marchaterre[38] in Rectangular Duct and Effect of Developing Flow due to Boiling. ANL Neg. No. 900-77-175.

With the increase in the cross-sectional mean void fraction, the peak of the local void fraction moves from the near-wall region to the central region, as shown in Figs. I.54 and I.55. This will lead to the increase in the value of C_0 as the void profile develops.

In view of the basic characteristic described above and various experimental data,[23,31,37,38] the following simple correlation is proposed:

$$C_0 = \left[C_\infty - (C_\infty - 1)\sqrt{\rho_g/\rho_f}\right]\left(1 - e^{-18\langle\alpha\rangle}\right). \qquad (44)$$

This expression indicates the significance of the developing void profile in the region given by $\langle\alpha\rangle < 0.25$; beyond this region, the value of C_0 approaches rapidly to the one for a fully developed flow (see Fig. I.59). Hence, for $\Gamma_g > 0$, we obtain

$$C_0 = \begin{cases} \left(1.2 - 0.2\sqrt{\dfrac{\rho_g}{\rho_f}}\right)\left(1 - e^{-18\langle\alpha\rangle}\right): & \text{round tube;} \\[2ex] \left(1.35 - 0.35\sqrt{\dfrac{\rho_g}{\rho_f}}\right)\left(1 - e^{-18\langle\alpha\rangle}\right): & \text{rectangular channel.} \end{cases} \qquad (45)$$

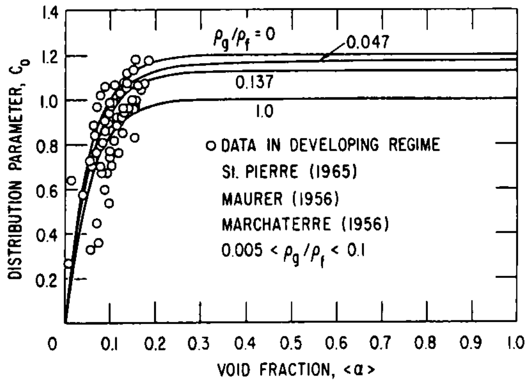

Fig. I.59

Distribution Parameter in Developing Flow due to Boiling. (Data for rectangular duct have been modified by a factor of 1.2/1.35 to obtain corresponding data for round tube.) ANL Neg. No. 900-77-186.

For most droplet or particulate flows in the turbulent regime, the volumetric flux profile is quite flat due to the turbulent mixing and particle slips near the wall that increase the volumetric flux. The concentration of dispersed phase also tends to be uniform, except for weak peaking near the core of the flow. Because of these profiles for j and α_d, the value of the distribution parameter C_0 is expected to be quite close to unity $(1.0 \leq C_0 \leq 1.1)$. Thus, by assuming that the covariance term is negligibly small for droplet or particulate flows, we have

$$\overline{V}_{dj} \simeq \langle\!\langle V_{dj} \rangle\!\rangle, \qquad (46)$$

in which case the local slip becomes important.

The calculation of $\langle\langle V_{dj}\rangle\rangle$ based on the local constitutive equations is the integral transformation, Eq. 18; thus it will require additional information on the void profile.[18] Instead of performing the integral operation defined by Eq. 18, we make the following simplifying approximations. The average drift velocity $\langle\langle V_{dj}\rangle\rangle$ due to the local slip can be predicted by the same expression as the local constitutive relations given in Ref. 18, provided the local void fraction α_d and the nondimensional difference of the stress gradient are replaced by the average values. These approximations are good for flows with a relatively flat void-fraction profile and can be considered acceptable from the overall simplicity of the one-dimensional model.

For a fully developed vertical flow, the stress distribution in the fluid and dispersed phase should be similar. Thus the effect of shear gradient on the mean local drift velocity can be neglected. Under these conditions, we obtain the following results:

Undistorted-particle Regime

The limiting case of the undistorted-particle regime is the Stokes regime in which the mean drift velocity reduces to

$$\overline{V}_{dj} = (C_0 - 1)\langle j\rangle + \frac{2r_d^2}{9}\,\frac{g\Delta\rho}{\mu_c}\,(1 - \langle\alpha_d\rangle)^2\,\frac{\mu_c}{\langle\mu_m\rangle}\,\frac{\rho_c - \rho_d}{\Delta\rho}. \tag{47}$$

Distorted-particle Regime

$$\overline{V}_{dj} = (C_0 - 1)\langle j\rangle + \sqrt{2}\left(\frac{\sigma g\Delta\rho}{\rho_c^2}\right)^{1/4}(1 - \langle\alpha_d\rangle)^{1.5}\,\frac{\rho_c - \rho_d}{\Delta\rho}. \tag{48}$$

Churn Turbulent-flow Regime

$$\overline{V}_{dj} = (C_0 - 1)\langle j\rangle + \sqrt{2}\left(\frac{\sigma g\Delta\rho}{\rho_c^2}\right)^{1/4}\left[\frac{\langle\mu_m\rangle}{\mu_c}(1 - \langle\alpha_d\rangle)\right]^{1/3}\frac{\rho_c - \rho_d}{\Delta\rho}. \tag{49}$$

Here the mean mixture viscosity[18] is given by

$$\frac{\langle\mu_m\rangle}{\mu_c} = 1 - \left(\frac{\langle\alpha_d\rangle}{\alpha_{dm}}\right)^{-2.5\alpha_{dm}(\mu_d+0.4\mu_c)/(\mu_d+\mu_c)} . \tag{50}$$

The value of maximum packing $\alpha_{dm} = 0.62$ is recommended for solid- or liquid-particle systems, though it can range anywhere from 0.5 to 0.74. However, for a bubbly flow, α_{dm} can be much higher. By considering

the standard range of interest of void fraction in bubbly flow, we may approximate α_{dm} by $\alpha_{dm} = 1$. Hence, for a bubbly flow, the mixture viscosity becomes

$$\frac{\langle \mu_m \rangle}{\mu_c} = \frac{1}{1 - \langle \alpha_d \rangle}. \tag{51}$$

On the other hand, for a particulate or drop flow with a low particle concentration, i.e., $\langle \alpha_d \rangle \ll 1$, $\langle \mu_m \rangle$ can be approximated by

$$\frac{\langle \mu_m \rangle}{\mu_c} = (1 - \langle \alpha_d \rangle)^{-2.6}. \tag{52}$$

In a horizontal flow with a complete suspension of the dispersed phase, the transverse mixing, which keeps the particles to be suspended, can significantly influence the stress gradient of each phase. Thus this effect may not be neglected. However, in view of the present state of the art, the assumption $\langle\!\langle V_{dj} \rangle\!\rangle \doteq 0$ may be used as a first-order approximation, particularly in high-flux flows.

For high-flux flows, the effect of the local drift, $\langle\!\langle V_{dj} \rangle\!\rangle$, on the mean drift velocity is small in comparison with the covariance term $(C_0 - 1)\langle j \rangle$. Thus, by neglecting the former, we have

$$\overline{V}_{dj} = \frac{(C_0 - 1)\langle \rho_m \rangle \overline{v}_m}{\langle \rho_m \rangle - (C_0 - 1)\langle \alpha_d \rangle (\rho_c - \rho_d)}. \tag{53}$$

For bubbly flows, Eq. 53 imposes a condition on applicable void-fraction ranges. Thus we should have $\langle \rho_m \rangle > (C_0 - 1)\langle \alpha_d \rangle (\rho_c - \rho_d)$. Here a simple criterion for the boundary between the high- and low-flux flows can be obtained by taking the ratio of the total volumetric flux and the terminal velocity. If this ratio is more than 10, the flow can be considered as a high-flux flow.

The other limiting case of the dispersed two-phase flow in a confined channel is the slug flow. When the volume of a bubble is very large, the shape of the bubble is significantly deformed to fit the channel geometry. The diameter of the bubbles becomes approximately that of the pipe with a thin liquid film separating the bubbles from the wall. The bubbles have the bullet form with a cap-shaped nose. The motion of these bubbles in relatively inviscid fluids can be studied by using a potential flow analysis around a sphere,[40] and the result is shown to agree with experimental data. Thus we have

$$\overline{V}_{dj} = 0.2\langle j \rangle + 0.35\left(\frac{gD\Delta\rho}{\rho_c}\right)^{1/2}, \tag{54}$$

which was originally proposed in Refs. 19 and 20.

3. Annular Two-phase Flow

In annular two-phase flows, the relative motions between phases are governed by the interfacial geometry, the body-force field, and the interfacial momentum transfer. The constitutive equation for the vapor-drift velocity in annular two-phase flows has been developed by taking into account those macroscopic effects of the structured two-phase flows.[41] Assuming steady-state, adiabatic, two-phase annular flow with constant single-phase properties, we have the following one-dimensional momentum equations for each phase:

$$-\left(\frac{dp_m}{dz} + \rho_g g_z\right) = \frac{\tau_i P_i}{\langle\alpha\rangle A} \tag{55}$$

and

$$-\left(\frac{dp_m}{dz} + \rho_f g_z\right) = \frac{P_{wf}\tau_{wf}}{A(1 - \langle\alpha\rangle)} - \frac{\tau_i P_i}{A(1 - \langle\alpha\rangle)}\,, \tag{56}$$

where τ_i, τ_{wf}, P_i, and P_{wf} are the interfacial shear, wall shear, interfacial wetted perimeter, and wall wetter perimeter, respectively. The hydraulic diameter and the ratio of wetted perimeters are defined by $D \equiv 4A/P_{wf}$ and $\xi \equiv P_i/P_{wf}$. By assuming that the film thickness δ is small compared with D, we have $4\delta/D \simeq 1 - \langle\alpha\rangle$. On the other hand, for an annular flow in a pipe, ξ reduces to $\sqrt{\alpha}$.

The wall shear can be expressed through the friction factor with a gravity-correction term by $\tau_{wf} = f_{wf}\rho_f\langle\langle v_f\rangle\rangle|\langle\langle v_f\rangle\rangle|/2 - \Delta\rho g_z\delta/3$, where f_{wf} can be given by the standard friction-factor correlation; $f_{wf} = 16/Re_f$ for laminar film flows and $f_{wf} = 0.0791Re_f^{-0.25}$ for turbulent flows. Here the film Reynolds number is given by $Re_f = \rho_f|\langle j_f\rangle|D/\mu_f$. Similarly, the interfacial shear can be expressed as $\tau_i = f_i\rho_g|\bar{v}_r|\bar{v}_r/2$ with the interfacial friction factor given by $f_i = 0.005[1 + 75(1 - \langle\alpha\rangle)]$ for rough wavy films.[42]

By definition, the vapor-drift velocity is related to v_r; i.e., $\overline{V}_{gj} = (1 - \langle\alpha\rangle)\bar{v}_r$. Hence, by eliminating the pressure gradient from the momentum equations, we obtain for a laminar film,

$$\overline{V}_{gj} = \pm\left\{\frac{16\langle\alpha\rangle}{\rho_g f_i \xi}\left|\frac{\mu_f\langle j_f\rangle}{D} + \frac{\Delta\rho g_z D(1 - \langle\alpha\rangle)^3}{48}\right|\right\}^{1/2}, \tag{57}$$

and for a turbulent film,

$$\overline{V}_{gj} = \pm\left\{\frac{\langle\alpha\rangle(1 - \langle\alpha\rangle)^3 D}{\rho_g f_i \xi}\left|\frac{0.005\rho_f\langle j_f\rangle|\langle j_f\rangle|}{D(1 - \langle\alpha\rangle)^3} + \frac{1}{3}\Delta\rho g_z\right|\right\}^{1/2}. \tag{58}$$

Here the negative root is taken when the term within the absolute signs becomes negative. The drift velocity in the form as expressed by Eqs. 57 and 58 is convenient for use in analyzing steady-state adiabatic or thermal equilibrium flows, since in these cases the value of $\langle j_f \rangle$ can be easily obtained.

The predicted vapor-drift velocity was compared to data from various experiments[43-45] under steady-state conditions, as shown in Fig. I.60. The three sets of data considered constitute about 350 data points for annular and drop-annular flow regimes. Theoretical predictions are within about ±30% of the experimental values over a wide range of vapor drift velocity lying between 20 and 250 cm/s. A quite uniform distribution of the data can be attributed to the uncertainty in the determination of void fraction in the above experiments. We note here that these data include a considerable number of points taken in the drop-annular flow regime at moderate gas flow rates. This indicates that the present vapor-drift-velocity correlation can be used both for ideal annular flows without entrainment as well as for drop-annular flows with moderate to low entrainment. However, as the amount of liquid entrained in the gas core becomes large at high gas flow rates,[42,46] the measured vapor-drift velocity starts to depart considerably from the predicted values and the present analysis overpredicts these values.

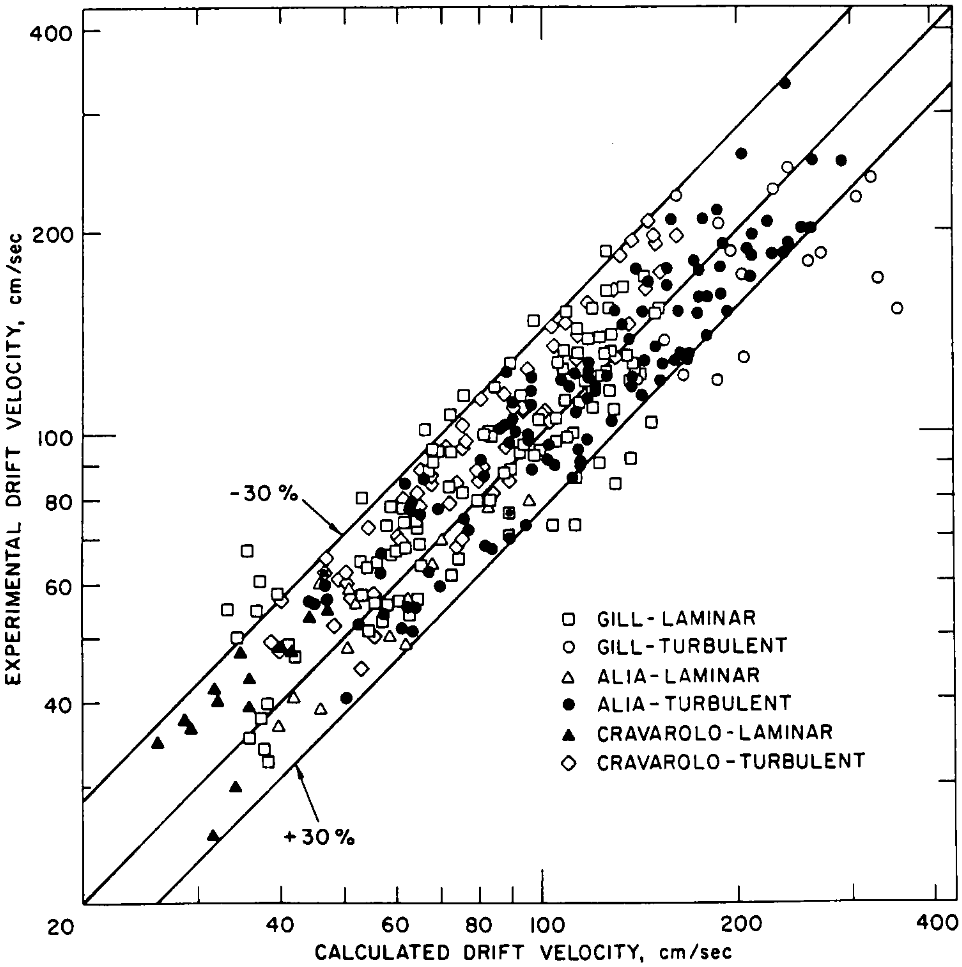

Fig. I.60. Comparison of Annular-flow Correlation to Experimental Data. ANL Neg. No. 900-5768.

The above correlations for the drift velocity in annular two-phase flow can be expressed in terms of the mixture velocity $\overline{v}_m$ rather than of the mean liquid flux $\langle j_f \rangle$, as $\overline{v}_m$ is the natural variable in the general drift-flux model formulation. Such expressions have been developed elsewhere.[41] However, it is also interesting and important to resolve the expressions for $\overline{V}_{gj}$ in terms of the total volumetric flux $\langle j \rangle$, since $\langle j \rangle$ was the variable used to correlate $\overline{V}_{gj}$ in dispersed two-phase flow regimes.

By considering the turbulent film flow regime and using the definition, $\langle j_f \rangle = (1 - \langle \alpha \rangle)\langle j \rangle - \langle \alpha \rangle \overline{V}_{gj}$, we can resolve Eq. 58 for the mean drift velocity $\overline{V}_{gj}$. The result does not have a very simple form. However, for most practical cases, it can be approximated by a linear function of $\langle j \rangle$ given by

$$\overline{V}_{gj} \doteq \frac{1 - \langle \alpha \rangle}{\langle \alpha \rangle + \left[\dfrac{1 + 75(1 - \langle \alpha \rangle)}{\sqrt{\langle \alpha \rangle}} \dfrac{\rho_g}{\rho_f}\right]^{1/2}} \left[\langle j \rangle + \sqrt{\frac{\Delta \rho g_z D(1 - \langle \alpha \rangle)}{0.015 \rho_f}}\right].$$

This expression may be further simplified to

$$\overline{V}_{dj} \doteq \frac{1 - \langle \alpha \rangle}{0.8 + 4\sqrt{\rho_g/\rho_f}} \left[\langle j \rangle + \sqrt{\frac{\Delta \rho g_z D(1 - \langle \alpha \rangle)}{0.015 \rho_f}}\right]. \tag{59}$$

From the comparison of Eq. 59 to Eq. 32, the apparent distribution parameter for annular flow becomes

$$C_0 = 1 + \frac{1 - \langle \alpha \rangle}{0.8 + 4\sqrt{\rho_g/\rho_f}}. \tag{60}$$

This indicates that the apparent C_0 in annular flow should be close to unity.

4. Annular-mist Flow

As the gas velocity increases in the annular flow, the entrainment of liquid from the film to the gas-core flow takes place. Based on the recently developed criteria for an onset of entrainment,[46] the critical gas velocity for a rough turbulent film flow can be given by

$$|j_g| > \frac{\sigma}{\mu_f} \sqrt{\frac{\rho_f}{\rho_g}} \times \begin{cases} N_{\mu f}^{0.8} & \text{for } N_{\mu f} \le \frac{1}{15} \\ 0.1146 & \text{for } N_{\mu f} > \frac{1}{15}, \end{cases} \tag{61}$$

where $N_{\mu f} \equiv \mu_f/[\rho_f \sigma\sqrt{\sigma/g\Delta\rho}]^{1/2}$. However, in general, the vapor flux is much larger than the liquid flux in the annular-mist-flow regime. Then, for a weakly viscous fluid such as water and sodium, the above correlation may be replaced by

$$|j| > \frac{\sigma}{\mu_f}\left(\frac{\rho_f}{\rho_g}\right)^{1/2}\left(\frac{\mu_f^2}{\rho_f\sigma\sqrt{\sigma/g\Delta\rho}}\right)^{0.4}. \tag{62}$$

If Inequality 62 is satisfied, then the droplet entrainment into the gas-core flow should be considered; otherwise the correlation for annular flow, Eq. 59, can be applied.

The correlation for $\overline{V}_{gj}$ in annular mist flows can be readily developed by combining the previous results for dispersed flow and pure annular flow. The fraction of liquid entrained in the gas core from total liquid at any cross section is denoted by E_d and the cross-sectional area averaged void fraction by $\langle\alpha\rangle$. Then the core area fraction is given by

$$\alpha_{core} = 1 - (1 - \langle\alpha\rangle)(1 - E_d), \tag{63}$$

and the mean liquid-droplet fraction in the gas core alone is given by

$$\alpha_{drop} = \frac{(1 - \langle\alpha\rangle)E_d}{1 - (1 - \langle\alpha\rangle(1 - E_d)}. \tag{64}$$

Consequently, α_{core} should be used in the annular-flow correlation, Eq. 59, to obtain the relative motion between the core and the film, whereas α_{drop} should be used in the dispersed-flow correlation to obtain a slip between droplets and gas-core flow.

Denote the gas-core velocity, liquid-drop velocity, and film velocity by v_{gc}, v_{fc}, and v_{ff}, respectively. The total volumetric flux is given by

$$\langle j\rangle = [v_{gc}(1 - \alpha_{drop}) + \alpha_{drop}v_{fc}]\alpha_{core} + v_{ff}(1 - \alpha_{core}). \tag{65}$$

Furthermore by denoting the total volumetric flux in the core based on the core area by j_{core}, we have from the annular correlation, Eq. 59,

$$j_{core} - \langle j\rangle \doteq \frac{(1 - \langle\alpha\rangle)(1 - E_d)}{0.8 + 4\sqrt{\rho_g/\rho_f}}\left[\langle j\rangle + \sqrt{\frac{\Delta\rho g_z D(1 - \langle\alpha\rangle)(1 - E_d)}{0.015\rho_f}}\right]. \tag{66}$$

On the other hand, from the dispersed-flow correlations, it can be shown that for a distorted-droplet or churn-droplet flow regime, the drift velocity can be given approximately by

$$\langle\!\langle v_g \rangle\!\rangle - j_{\mathrm{core}} = \sqrt{2}\left(\frac{\sigma g \Delta\rho}{\rho_g^2}\right)^{1/4} \frac{E_d(1 - \langle\alpha\rangle)}{\langle\alpha\rangle + E_d(1 - \langle\alpha\rangle)}. \tag{67}$$

Here we have used an approximation based on $(1 - \langle\alpha\rangle) \ll 1$. However, depending on the core-gas velocity, the dispersed-flow-drift velocity correlation for much smaller particle should be used. When the droplets are generated by the entrainment of liquid film, the following approximate form is suggested for an undistorted particle regime outside of the Stokes regime:[18]

$$\langle\!\langle v_g \rangle\!\rangle - j_{\mathrm{core}} = 0.5 r_d \left[\frac{(g\Delta\rho)^2}{\mu_g \rho_g}\right]^{1/3} \frac{E_d(1 - \langle\alpha\rangle)}{\langle\alpha\rangle + E_d(1 - \langle\alpha\rangle)}, \tag{68}$$

where the particle radius may be approximated from the Weber-number criteria at the shearing-off of wave crests. Thus,

$$r_d \doteq \frac{6\sigma}{\rho_g}\left(\frac{0.8 + 4\sqrt{\rho_g/\rho_f}}{|\langle j \rangle|}\right)^2. \tag{69}$$

The above second relation applies only when the total volumetric flux is sufficiently high to induce fragmentations of the wave crests. Hence Eq. 68 should be used when

$$|\langle j \rangle| > 1.456\left(\frac{\sigma g \Delta\rho}{\rho_g^2}\right)^{1/4} \left(0.8 + 4\sqrt{\rho_g/\rho_f}\right) \left(\frac{\mu_g^2}{\rho_g \sigma \sqrt{\sigma/g\Delta\rho}}\right)^{-1/12}. \tag{70}$$

Combining the above results we obtain

$$\begin{aligned} \overline{V}_{gj} = {} & \frac{(1 - \langle\alpha\rangle)(1 - E_d)}{0.8 + 4\sqrt{\rho_g/\rho_f}} \left[\langle j \rangle + \sqrt{\frac{\Delta\rho g_z D(1 - \langle\alpha\rangle)(1 - E_d)}{0.015\rho_f}}\right] \\ & + \frac{E_d(1 - \langle\alpha\rangle)}{\langle\alpha\rangle + E_d(1 - \langle\alpha\rangle)} \times \begin{cases} \sqrt{2}\left(\dfrac{\sigma g \Delta\rho}{\rho_g^2}\right)^{1/4} \\ \text{or} \\ \dfrac{3\sigma}{\rho_g}\left[\dfrac{(g\Delta\rho)^2}{\mu_g \rho_g}\right]^{1/3} \left(\dfrac{0.8 + 4\sqrt{\rho_g/\rho_f}}{|\langle j \rangle|}\right)^2, \end{cases} \end{aligned} \tag{71}$$

where the latter expression applies under the condition given by Eq. 70. If the radius of the particle is very small, then the essential contribution to the

relative motion between phases comes from the first term of Eq. 71 and the core flow may be considered as a homogeneous dispersed flow. In such a case, Eq. 71 reduces to

$$\overline{V}_{dj} \doteq \frac{(1 - \langle\alpha\rangle)(1 - E_d)}{0.8 + 4\sqrt{\rho_g/\rho_f}}\left(\langle j\rangle + \sqrt{\frac{\Delta\rho g_z D(1 - \langle\alpha\rangle)(1 - E_d)}{0.015\rho_f}}\right). \tag{72}$$

This expression shows linear decrease of drift velocity in terms of entrained liquid fraction, which can be observed in various experimental data.[44,45]

5. Conclusions

For a dispersed two-phase flow system, the relative motion between phases has been analyzed by considering the drag force, the gravitational force, and the effect of the pressure gradient due to shear stresses and using a similarity hypothesis based on the Reynolds number and drag coefficient. Here the effect of the multiparticle is taken into account by using the mixture viscosity in the Reynolds number. The present model for the relative motion between phases has been developed for general dispersed two-phase flows; therefore its applicability is not limited to particulate flows, but it can also be applied to bubbly and droplet flows. In the case of solid-particle systems, it agrees with experimental data at all Reynolds-number and particle-concentration ranges of practical interest. Furthermore, the present theory can be reduced to the existing theoretical model for a solid-particle system in the Stokes regime by considering the limiting case of small particles. On the other hand, for fluid-particle systems, considering bubble flows in a vertical channel the present model can be essentially reduced to conventional semiempirical correlations. Consequently, the relative motion between phases in dispersed two-phase flows can be predicted by the unified theory for both solid- and fluid-particle systems at all Reynolds-number ranges.

For an annular flow, the constitutive equation for the drift velocity was developed by taking into account the effect of gravity, interfacial shear stress with its dependence on interfacial roughness, and flow regimes in the liquid film. The constitutive equation obtained is cast into two different forms, one useful for analyzing steady-state flows and the other for transient flows. The predicted vapor-drift velocity from this study was compared to about 350 data points from various experiments. Although the data used in the comparison included those taken in the drop-annular flow regimes with moderate entrainment, the theoretical predictions are within ±30% of the measured values. However, when the amount of liquid entrainment was large, the present correlation overpredicts the vapor drift velocity. This trend can easily be explained by a newly developed correlation for an annular dispersed flow regime, which shows an almost linear decrease of drift velocity in terms of entrained liquid mass.

The present constitutive equations for the drift velocity in various two-phase flow regimes have been obtained from the steady-state and adiabatic formulations. The effects of heat transfer and phase changes on the drift velocity were considered as secondary. These effects appear only indirectly through the local variables such as the void fraction and the mixture velocity in the drift constitutive equation. It is a common practice to apply constitutive relationships obtained under steady-state conditions to the transient problems, with an assumption that the parameters entering into a constitutive relationship are local variables and are functions of time. Therefore, the application of the present constitutive equation for the drift velocity to the transient two-phase flow with a phase change will be consistent with the common practice.

However, note that the basic assumption of the drift-flux model is that a strong coupling exists between the motions of two phases. Therefore, certain two-phase problems involving a sudden acceleration of one phase may not be appropriately described by this model. In these cases, inertia terms of each phase should be considered separately, that is, by use of a two-fluid model. However, in many practical engineering problems, the real usefulness of the drift-flux model comes from the fact that even two-phase mixtures that are weakly coupled locally are strongly coupled when considered as a total system. This is because the relatively large axial extent of the systems usually gives sufficient interaction times for the momentum exchange between two phases.

References

1. Thermophysical Properties of Refrigerants, American Society of Heating, Refrigerating, and Air-Conditioning Engineers (1973).
2. N. B. Vargaftik, Tables on the Thermophysical Properties of Liquids and Gases, John Wiley & Sons (1976).
3. D. C. Groeneveld, The Thermal Behavior of a Heated Surface at and beyond Dryout, AECL-4309 (1972).
4. R. W. Bowring, A Simple But Accurate Round Tube, Uniform Heat Flux, Dryout Correlation Over the Pressure Range 0.7-17 MN/m^2, AEEW-R789 (1972).
5. S. Y. Ahmad, Fluid to Fluid Modeling of Critical Heat Flux: A Compensated Distortion Model, Int. J. Heat Mass Transfer 16, 641 (1973).
6. R. A. Smith, Critical Heat Flux in Flow Reversal Transients, Ph.D. thesis, M.E. Dept., MIT (May 1975).
7. O. G. Smith, W. M. Rohrer, Jr., and L. S. Tong, Burnout in Steam-Water Flows with Axially Nonuniform Heat Flux, ASME Paper 65-WA/HT-33 (1965).
8. A. Hassid and R. Rychlicki, An Attempt to Use Steady-State Data for Determining CHF in Transient Conditions, Energia Nucleare 18(6), 333 (1971).

9. G. E. Dix, Freon-Water Modeling of CHF in Round Tubes, ASME Paper 70-HT-26 (1970).

10. J. C. Pureupile, L. S. Tong, and S. W. Gouse, Jr., Refrigerant-Water Scaling of Critical Heat Flux in Round Tubes-Subcooled Forced Convection Boiling, J. Heat Transfer 55 (1973).

11. H. S. Crapo, M. F. Jensen, and K. E. Sackett, Experimental Data Report for Semiscale Mod-1 Tests S-02-9 and S-02-9A (Blowdown Heat Transfer Tests), ANCR-1236 (Jan 1976).

12. H. S. Crapo, M. F. Jensen, and K. E. Sackett, Experimental Data Report for Semiscale Mod-1 Test S-29-2 (Integral Test from Reduced Pressure), ANCR-1328 (Aug 1976).

13. J. C. Leung and R. E. Henry, "Transient Critical Heat Flux," Light-Water-Reactor Safety Research Program: Quarterly Progress Report, July-September 1976, ANL-76-121 (1976).

14. M. N. Hutcherson, Contribution to the Theory of the Two-phase Blowdown Phenomenon, ANL-75-82 (Dec 1975).

15. Y. S. Cha and R. E. Henry, Effects of Dissolved Gas During Blowdown Tests, Trans. Am. Nucl. Soc. 24 (1976).

16. M. Ishii, Thermally-induced Flow Instabilities in Two-phase Mixtures in Thermal Equilibrium, Ph.D. thesis, Georgia Institute of Technology, Georgia (1971).

17. M. Ishii, Thermo-fluid Dynamic Theory of Two-phase Flow, Chapters IX and X, Eyrolles, Paris, Scientific and Medical Publication of France, N. Y. (1975).

18. M. Ishii, "One-dimensional Drift-flux Modeling: One-dimensional Drift Velocity of Dispersed Flow in Confined Channel," Light-Water-Reactor Research Program: Quarterly Progress Report, January-March 1976, ANL-76-49.

19. D. J. Nicklin, J. O. Wilkes, and J. F. Davidson, Two-phase Flow in Vertical Tubes, Trans. Inst. Chem. Eng. 40, 61 (1962).

20. L. G. Neal, An Analysis of Slip in Gas-liquid Flow Applicable to the Bubble and Slug Flow Regimes, Report KR-2, Kjeller Research Establishment, Norway (1963).

21. N. Zuber and J. A. Findley, Average Volumetric Concentration in Two-phase Flow Systems, J. Heat Trans. 87, 453 (1965).

22. S. G. Bankoff, A Variable Density Single-fluid Model for Two-phase Flow with Particular Reference to Steam-water Flow, J. Heat Transfer, Trans. ASME 82, 265 (1960).

23. N. Zuber, F. W. Staub, G. Bijwaard, and P. G. Kroeger, Steady State and Transient Void Fraction in Two-phase Flow Systems, General Electric Co. Report GEAP-5417, Vol. 1 (1967).

24. T. A. Hughes, Steam-Water Mixture Density Studies in a Natural Circulation High Pressure System, Babcock and Wilcox, G. Report No. 5435 (1958).

25. R. J. Thome, Effect of a Transverse Magnetic Field on Vertical Two-phase Flow through a Rectangular Channel, ANL-6854 (Mar 1964).

26. G. E. Smissaert, Two-component Two-phase Flow Parameters for Low Circulation Rates, ANL-6755 (July 1963).

27. M. Petrick, A Study of Vapor Carryunder and Associated Problems, ANL-6581 (July 1962).

28. F. Bergonzoli and F. J. Halfen, Heat Transfer and Void Formation during Forced Circulation Boiling of Organic Coolants, NAA-SR-8906, Atomics International (1964).

29. W. T. Hancox and W. B. Nicoll, Prediction of Time-dependent Diabatic Two-phase Water Flows, Prog. Heat Mass Transfer 6, 119 (1972).

30. J. Nikuradse, Gesetzmäsigkeit der turbulenten strömung in glatten Rohren, Forsch. Arb. Ing.-Wes. 356 (1932).

31. G. W. Maurer, A Method of Predicting Steady State Boiling Vapour Fractions in Reactor Coolant Channels, WAPD-BT-19 (1956).

32. G. B. Wallis, D. A. Steen, S. N. Brenner, and T. M. Turner, Joint U. S.-Eurotom Research and Development Program, Quarterly Progress Report, January, Dartmouth College (1964).

33. S. C. Rose and P. Griffith, Flow Properties of Bubbly Mixtures, ASME Paper 65-HT-8 (1965).

34. N. Adorni, G. Peterlongo, R. Ravetta, and F. A. Tacconi, Large Scale Experiments on Heat Transfer and Hydrodynamics with Steam-Water Mixtures, CISE Report R-91, Italy (1964).

35. S. Z. Rouhani and K. M. Becker, Measurement of Void Fractions for Flow of Boiling Heavy Water in a Vertical Round Duct, AE-106, Aktiebolaget Atomenergi, Sweden (1963).

36. K. Schwartz, Investigation of Distribution of Density, Water and Steam Velocity and of the Pressure Drop in Vertical Horizontal Tubes, VDI-Forschungsh. 20(B), 445 (1954).

37. C. C. St. Pierre, Frequency-response Analysis of Steam Voids to Sinusoidal Power Modulation in a Thin-walled Boiling Water Coolant Channel, ANL-7041 (May 1965).

38. J. F. Marchaterre, The Effect of Pressure on Boiling Density in Multiple Rectangular Channels, ANL-5522 (Feb 1956).

39. J. L. L. Baker, Flow-regime Transitions at Elevated Pressures in Vertical Two-phase Flow, ANL-7093 (Sept 1965).

40. D. T. Dumitrescu, Stomung an einer Luftblase in senkrechten Rohr, Z. Ang. Math. Mech. 23, 139 (1943).

41. M. Ishii, T. C. Chawla, and N. Zuber, Constitutive Equation for Vapor Drift Velocity in Two-phase Annular Flow, AIChE J. 22, 283 (1976).

42. G. B. Wallis, One-dimensional Two-Phase Flow, McGraw-Hill, N. Y. (1969).

43. L. E. Gill and G. F. Hewitt, Further Data on the Upwards Annular Flow of Air-Water Mixtures, UKAEA Report AERE-R3935 (1962).

44. P. Alia, L. Cravarolo, A. Hassid, and E. Pedrocchi, Liquid Volume Fraction in Adiabatic Two-phase Vertical Upflow-Round Conduit, CISE Report-105, Italy (1965).

45. L. Cravarolo, A. Giorgini, A. Hassid, and E. Pedrocchi, A Device for the Measurement of Shear Stress on the Wall of a Conduit; Its Application in the Mean Density Determination in Two-phase Flow; Shear Stress Data in Two-Phase Adiabatic Vertical Flow, CISE Report-82, Italy (1964).

46. M. Ishii and M. A. Grolmes, Inception Criteria for Droplet Entrainment in Two-Phase Concurrent Film Flow, AIChE J. 21, 308 (1975).

II. TRANSIENT FUEL RESPONSE AND FISSION-PRODUCT RELEASE PROGRAM

Responsible Group Leaders:
L. A. Neimark and M. C. Billone, MSD

Coordinated by:
L. R. Kelman, MSD

A physically realistic description of fuel swelling and fission-product release is needed to aid in predicting the behavior of fuel rods and fission products under certain hypothetical Light-Water Reactor (LWR) accident conditions. To satisfy the near term need, a comprehensive computer-base model, the Steady State and Transient Gas-release and Swelling Subroutine (SST-GRASS) code, is being developed at Argonne National Laboratory (ANL). This model is being incorporated into the Fuel-Rod Analysis Program (FRAP) code being developed by EG&G Idaho, Inc., at the Idaho National Engineering Laboratory (INEL). The analytical effort is supported by a data base and correlations developed from characterization of irradiated LWR fuel and from out-of-reactor transient heating tests on irradiated commercial LWR fuel under a range of thermal conditions. The experimental results will also serve as input to NRC-sponsored programs that are developing a radiological source term for hypothetical accidents. In the near term, emphasis in the experimental program is being placed on Pressurized-Water Reactor (PWR) fuel thermal conditions that are applicable to anticipated hypothetical power-cooling-mismatch (PCM) accidents. Later experimental efforts will turn to conditions typical of other types of hypothetical accidents. The program is also developing information on fission-gas release during steady-state and load-following operations.

J. Rest and M. C. Billone attended the Fuel Behavior Program Review Group and FRAP User Briefing on November 2, 1976, at Silver Spring, Maryland, and gave a progress report on GRASS and a presentation of LWR-LIFE.

Recent significant analytical and experimental advances and the status of the program at the end of this quarter are summarized below.

1. Sensitivity analyses with SST-GRASS have shown that thermal stress-induced separations at grain boundaries weakened by fission-product concentration may be necessary to account for fission-gas release during transient DEH test conditions and during steady-state conditions at high burnup.

2. We are working with EG&G to interface GRASS with FRAP and to perform FRAP-GRASS sensitivity analyses for LOCA and RIA conditions to provide input to the experimental DEH programs.

3. Existing information on the behavior of volatile fission products during steady-state and transient conditions have been assessed, and models for the diffusion of the volatiles to grain boundaries have been developed.

4. Preliminary correlations of fission-gas release with test conditions have been made from PCM-like tests of high-burnup Robinson fuel. Tests run to date include heating rates of ~400, 200, 80, and 25°C/s to central melting and several tests of 25°C/s below melting. A systematic series of 25°C/s tests is being run to, and short of, melting under as closely identical conditions as current capability permits to improve reproducibility and correlations.

5. A PCM-like test of a lower-burnup Robinson fuel pellet (about half the burnup used in the other tests) was run at ~25°C/s to central melting. The fission gas is being analyzed, and the fuel is being characterized.

6. A plan was developed with EG&G[1] and the near-term activities were approved by NRC-RSR[2] for cross-checking direct-electrical-heating (DEH) test results with results of the Power Burst Facility (PBF) irradiation-effect series to account for observed differences. Fuel has been prepared by EG&G, and arrangements have been made to ship it to ANL-East early in January 1977.

A. Modeling of Fuel-fission-product Behavior (J. Rest, MSD)

1. Development of Volatile-fission-product Behavior Code

The calculation of the behavior of volatile fission products (VFP's) is complicated by the fact that the VFP's can react chemically to form compounds. For example, the VFP's cesium, tellurium, and iodine can react chemically within the UO_2 to form compounds such as cesium iodide, cesium telluride, cesium molibdate, and cesium uranate. Cesium iodide, cesium telluride, and cesium molibdate are relatively stable and, under the proper conditions, can nucleate into bubbles. At higher temperatures, all these compounds can disassociate into atomic form.

The complexity of the problem is enhanced by the lack of adequate data for the diffusivities of the atomic species, the diffusivities of the various compounds, and the rates at which the compounds are formed. One approach to modeling the behavior of VFP's is to ignore the formation of the compounds and to model the behavior of the atomic species by standard diffusional techniques. However, an oversimplification of the problem has the disadvantages of inflexibility as new data become available and rigidity in analysis. It therefore seems advantageous, at the outset, to develop a model capable of describing the behavior of the VFP's realistically and then to add available information to the model. With this approach, sensitivity analyses can be performed to determine key factors influencing VFP behavior, even though various physical properties are lacking. The results of the sensitivity analyses can then be used as a criterion to establish the relative importance of obtaining physical-property data.

The formation of the VFP compounds can be assumed to take place preferentially on the grain boundaries where there is a relatively high

concentration of the atomic species. Thus, the theory of atomic diffusion can be used to calculate the behavior of the VFP's within the grains with reasonable accuracy. Code calculations will be compared with the results of in-reactor irradiations under load-following conditions as well as with the results of the DEH experiments. Therefore the equation to be solved for the concentration $N_i(r,t)$ of the VFP's within the grains (i = I, Cs, Te, etc.) is

$$\frac{\partial N_i(r,t)}{\partial t} = D_i^L \nabla^2 N_i(r,t) + \beta_i - \lambda_i N_i(r,t) \tag{1}$$

with the boundary conditions for Eq. 1 given by

$$\left.\begin{aligned} N_i(a,t) &= C_i(t) \\ &\text{and} \\ N_i(r,0) &= N_i^0 \end{aligned}\right\}, \tag{2}$$

where $C_i(t)$ and N_i^0 are the VFP concentration on the grain boundaries and the initial concentration in the lattice, respectively, and a is the radius of the grain. In Eq. 1, D_i^L, β_i, and λ_i are the VFP diffusivity in the lattice, the production rate, and the decay constant, respectively.

In keeping with the spirit of the GRASS calculational procedure, the solution to Eq. 1 is best expressed as the sum of the solutions of two separate problems: the solution of

$$\frac{\partial N_i(r,t)}{\partial t} = D_i^L \nabla^2 N_i(r,t) + \beta_i - \lambda_i N_i(r,t), \tag{3}$$

with the boundary conditions

$$N_i(a,t) = N_i(r,0) = 0;$$

and the solution of

$$\frac{\partial N_i(r,t)}{\partial t} = D_L^i \nabla^2 N_i(r,t) - \lambda_i N_i(r,t), \tag{4}$$

with the boundary conditions

$$\left.\begin{aligned} N_i(a,t) &= Ci \\ &\text{and} \\ N_i(r,t_0) &= N_i^0 \end{aligned}\right\}.$$

Equation 3 will be valid for constant β_i from $t = 0$ to $t = t_0$; at $t = t_0$, β_i changes to β_i', and from $t = t_0$ to $t - t_1$ the solution is the sum of Eqs. 3 and 4 with t replaced by t', where $t' = t - t_0$ and N_i^0 is the concentration in the lattice of the VFP at $t = t_0$. For the times between $t = t_1$ and $t = t_2$, when the production rate is β_i'', the solution is obtained in an analogous fashion. The approximation $N_i(a, t) = 0$ for the first time interval is quite good, since the concentration of VFP's on the grain boundaries so early in life (i.e., startup) is very small. Under transient DEH test conditions, the solution for the diffusion in the lattice of the VFP's is obtained from Eq. 4 with t replaced by h, the code time increment; N_i^0 and C_i are computed as a function of time.

The solution of Eq. 3 can be obtained using Fourier series.[3] Thus,

$$N_i(r,t) = \frac{\beta_i}{\lambda_i r}\left[r - \frac{a \sinh\left(r\sqrt{\lambda_i/D_i^L}\right)}{\sinh\left(a\sqrt{\lambda_i D_i^L}\right)} + \frac{2\lambda_i a^3 \exp(-\lambda_i t)}{D_i^L \pi} \sum_{n=1}^{\infty} \frac{(-1)^n \sin(n\pi r/a)\exp(-n^2\pi^2 D_i^L t/a^2)}{n(n^2\pi^2 + \lambda_i a^2/D_i^L)}\right] . \tag{5}$$

The rate of release to the grain boundaries is found from the concentration gradient at the outer surface,

$$R_i = -\frac{3D_i^L}{a}\left[\frac{\partial N_i(r,t)}{\partial r}\right]_{r=a} . \tag{6}$$

Thus, from Eqs. 5 and 6,

$$R = 3\left(\frac{1}{\sqrt{\mu_i}}\coth\sqrt{\mu_i} - \frac{1}{\mu_i}\right) - b \exp(-\mu_i \tau_i) \sum_{n=1}^{\infty} \frac{\exp(-n^2\pi^2\tau_i)}{n^2\pi^2 + \mu_i} ,$$

where the dimensionless parameters $\mu_i \tau_i$ are defined by

$$\left.\begin{aligned} \mu_i &= \lambda_i a^2/D_i^L \\ &\text{and} \\ \tau_i &= D_i^L t/a^2 \end{aligned}\right\} . \tag{7}$$

In an analogous manner, the solution to Eq. 4 is found to be

$$N_i(r,t) = \frac{-2aN_i^0}{r\pi}\sum_{n=1}^{\infty}\frac{(-1)^n}{n}\exp\left[-(n^2\pi^2D_i^L/a^2+\lambda_i)t\right]\sin\frac{n\pi r}{a}$$

$$+\frac{2D_i^LC_i\pi}{ra}\sum_{n=1}^{\infty}(-1)^n n\sin(n\pi r/a)\left[\frac{1-\exp[-(n^2\pi^2D_i^L/a^2+\lambda_i)t]}{n^2\pi^2D_i^L/a^2+\lambda_i}\right]. \tag{8}$$

The release rate, R_i, is obtained from Eqs. 6 and 8:

$$R_i = \frac{6\lambda_iN_i}{\mu_i}\sum_{n=1}^{\infty}\exp\left[-(n^2\pi^2/\mu_i+1)\lambda_it\right]$$

$$-\frac{6\lambda_i^2C_i\pi^2}{\mu_i^2}\sum_{n=1}^{\infty}n^2\left\{\frac{1-\exp[-n^2\pi^2/\mu_i+1)\lambda_it]}{\lambda_i(1+n^2\pi^2/\mu_i)}\right\}+3C_i\lambda_i/\mu_i. \tag{9}$$

The next step in the calculation of the behavior of the VFP's is to set up equations describing the rate of formation of VFP compounds on the grain boundaries, and subsequent VFP diffusion along the boundaries to the grain edges. Equations describing the volatization of the compounds at increased temperatures will also be included.

This work will continue at a slow rate, due to priorities set by the NRC.

2. Transient Fission-gas Release

Scanning-electron-microscope (SEM) examinations (see ANL-76-87, p. 22) of DEH-tested fuel have revealed the development of sinuous channels on the grain faces after a saturation density of grain-boundary fission gas has been attained. These face channels link up and extend to the grain-edge channels, thus enhancing the release of the gas from the grains. Models that characterize this phenomenon have been developed and included in GRASS this quarter.

The GRASS model for grain-boundary saturation by fission-gas bubbles is based on the fact that the area of grain boundary occupied by fission-gas bubbles is nearly independent of the bubble-size distribution (i.e., the bubble surface area is conserved after bubble coalescence). If the gas is assumed to occupy equal, close-packed, touching bubbles, then the maximum areal coverage per unit area of grain boundary is $A^* = 0.907$. Since the bubble size does not affect the atom areal density, the areal coverage by the fission gas is approximately equal to the coverage by a single bubble,

of radius R_{max}, which is formed by the coalescence of all the gas on the grain face. Assuming that the bubble surface area is conserved after bubble coalescence leads directly to an expression for R_{max} in terms of the total quantity of gas on the boundary; i.e.,

$$R_{max} = R_A\sqrt{N}, \tag{10}$$

where R_A is the atomic radius and N is the total number of gas atoms on the grain face. The condition for grain-boundary saturation by fission gas is then given by

$$\pi R^2_{max} = \frac{4}{3}\pi a^3 A^* \frac{AGBY}{14}, \tag{11}$$

where AGBY is the grain boundary area per unit volume, and an approximate tetrakaidecahedral (14-sided) lattice geometry has been assumed. Combining Eqs. 10 and 11 leads to an expression for N^A_{sat}, the minimum number of gas atoms per unit area of grain boundary required for saturation:

$$N^A_{sat} = \frac{A^*}{14\pi R^2_A} = \frac{0.0206}{R^2_A}. \tag{12}$$

Equivalently, the minimum number of 500-Å-dia (5×10^{-5}-mm-dia) bubbles per unit area of grain boundary required for saturation is

$$N^{500}_{sat} = \frac{0.0206}{R^2_{500}} = 3.3 \times 10^9 \text{ bubbles/cm}^2. \tag{13}$$

This result is in excellent agreement with the measured 500-Å (5×10^{-5}-mm) grain-boundary bubble-saturation density of $2.2\text{-}4.3 \times 10^9/\text{cm}^2$ (see ANL-76-87, p. 23).

SST-GRASS was used to simulate the steady-state irradiation as well as some of the transient DEH tests of the H. B. Robinson fuel. The predicated pre- and posttest bubble-size distributions are in qualitative agreement with experimental observations. Under DEH test conditions, the observed channel formation on grain boundaries was predicted; no channel formation was observed and none was predicted for the steady-state irradiation.

3. Steady-state Sensitivity Analyses

At the request of the NRC, the SST-GRASS code was used for the analysis of the burnup dependence of fission-gas release from LWR fuel rods with the specific objective of identifying possible fuel/fission-gas behavioral mechanisms that could lead to excessive gas release at high burnup.

Figure II.1 shows SST-GRASS results for fractional fission-gas release versus burnup for a hypothetical irradiation in the H. B. Robinson reactor. Figure II.1 shows predicted fractional fission-gas release (cumulative) versus burnup for two different fuel-temperature histories during a 7-kW/ft (23-kW/m) irradiation. The solid lines depict the "normal" SST-GRASS centerline temperature history and fractional fission-gas release; the broken lines show the predicted results for an SST-GRASS run in which no variation in the fuel-cladding gap conductance was allowed. For the "normal" temperature history, the fuel centerline temperature decreases during irradiation due to gap closure (fuel swelling and cladding creep-down); the fractional fission-gas release climbs rapidly to a maximum and then gradually declines for the duration of the irradiation. This fall-off in the fractional gas release is due, in part, to the densification of the UO_2; as the UO_2 densifies, the volume fraction of interlinked porosity (and thus the number of available paths from the interior to the exterior of the fuel) decreases.

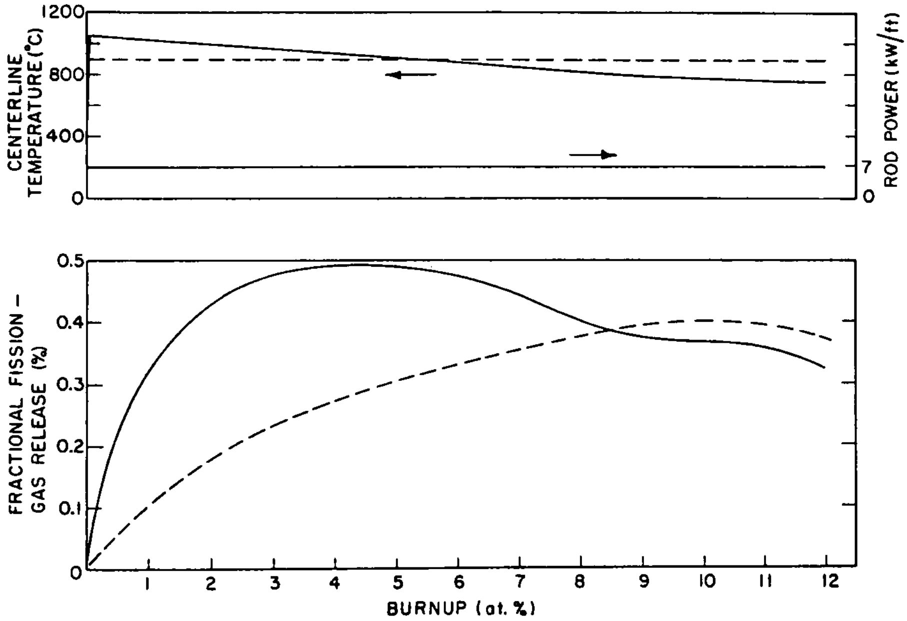

Fig. II.1. SST-GRASS-calculated Fractional Fission-gas Release vs Burnup for an Irradiation at 7 kW/ft (23 kW/m). The broken curves are the results assuming an "abnormal" temperature history where no variation in the fuel-cladding gap conductance was allowed. Conversion factor: 1 kW/ft = 3.281 kW/m.

For the temperature history having no variation in the fuel-cladding gap conductance, the fractional fission-gas release gradually increases to a maximum at high burnup before starting a slow decline. The decrease in the fractional gas release at high burnup for these cases is due more to fuel densification than to the gradual decline in fuel temperatures caused by an increasing UO_2 thermal conductivity with decreasing porosity. Thus, there appears to be both a temperature and a burnup dependence of the fractional fission-gas release from this LWR fuel rod.

In 1969, Bellamy and Rich[4] presented evidence that, for fuel rods with centerline temperatures less than 1630°C, a large increase in gas release can occur at burnups above 3 at. %. Below 3 at. % burnup, the fission-gas release is compatible with diffusional release and "knockout" models. The marked increase in gas release above 3 at. % was believed to arise, in part, from the interconnection of grain-boundary gas bubbles and, in part, from the fracture under thermal stress of grain boundaries weakened by gas bubbles.

In the range of SST-calculated power levels, fuel temperatures, grain sizes, and densities for the irradiation depicted in Fig. II.1, the grain-boundary saturation condition described by Eq. 12 was never achieved. No evidence for grain-face channel formation in H. B. Robinson fuel irradiated to 3 at. % burnup has been detected. However, grain-boundary channel formation has been observed in fuel specimens that have undergone DEH transient testing (see ANL-76-87, pp. 22-24). Thus, although this mechanism of gas release might not be important for steady-state irradiations, during transient conditions it may play a major role in the rapid release of gas from the grain faces.

The other possibility for an enhanced release of fission gas at high burnups indicated by Bellamy and Rich is the fracture under thermal stress of grain boundaries weakened by gas bubbles; the gas on the boundaries and in the interconnected porosity along the grain edges would be vented through such a fracture, or series of fractures, to the fuel surface. Whereas Bellamy and Rich observed mainly transgranular cracks in fuel specimens irradiated at less than 3 at. % burnup, at higher burnups the grain-boundary strength was reduced to such an extent that thermal-stress cracking became intergranular rather than transgranular. This type of fuel fracturing has been observed on an accelerated scale in fuel specimens subjected to DEH transient tests (see ANL-76-49, pp. 29-30).

A preliminary GRASS model describing the burst release of fission gas due to fuel fracturing was developed last quarter (see ANL-76-121, p. 63). The input to this model is the number of cracks occurring during a time interval in a particular fuel annulus. The LIFE-III cracking model used in the SST code currently supplies this information for steady-state irradiations. This cracking model is not sophisticated enough to predict the tears and separations that might result in fuel in which thermal stress is experienced and in which grain-boundary weakening by fission-product deposition has occurred. Such a cracking model, consisting of a detailed stress analysis, would require a realistic treatment of fission-product behavior (e.g., GRASS). During a power decrease, GRASS calculates the rate at which fission gas vents to the fuel surface when it is located in a closed network of interconnected porosity, initially not connected to fuel surfaces, that intercepts a crack.

Figure II.2 shows SST-GRASS results for the "normal" irradiations of Fig. II.1 with the addition of several reactor cycles occurring during the

irradiation. Various constants in the GRASS burst-release model are uncertain; therefore the fractional gas-release results in Fig. II.2 are not quantitative predictions. However, they represent an initial qualitative description of the dependence of fission-gas release on fuel fracturing. The results indicate that fuel fracturing can lead to enhanced gas release at high burnup.

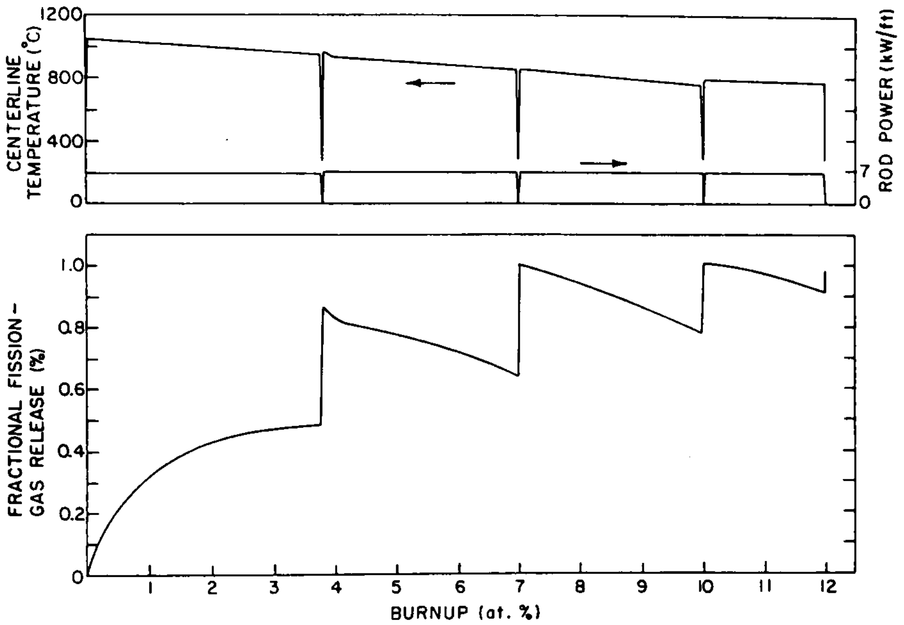

Fig. II.2. SST-GRASS-calculated Fractional Fission-gas Release vs Burnup for an Irradiation at 7 kW/ft (23 kW/m) with Power Cycling. Conversion factor: 1 kW/ft = 3.281 kW/m.

In conclusion, a rapid increase in the fission-gas release rate at high burnup can be qualitatively understood in terms of the thermal-stress-induced separation of grain boundaries weakened by fission-product deposition. Analytical models describing this type of fuel fracturing currently do not exist. Such models, consisting of a detailed stress analysis, would require a sophisticated treatment of fission-product behavior (e.g., GRASS).

4. FRAP-GRASS Development

Personnel from ANL aided EG&G in interfacing GRASS with FRAP-T for execution on the new EG&G CDC 7600 computer. The GRASS-code format required modification, and a moderate number of changes to the program were required. The resulting FRAP-GRASS code system was executed successfully on the CDC 7600.

B. Experimental Program (L. R. Kelman and S. M. Gehl, MSD)

In this section, DEH transient tests of irradiated H. B. Robinson fuel that have been run to date are summarized and compared with the originally planned initial series of transient tests (see ANL-76-15, pp. 43-45). Also

discussed are the results of DEH transient tests run this quarter and developments and status of the DEH/PBF cross-check program.

1. Transient Heating Tests (L. R. Kelman, M. G. Seitz, S. M. Gehl, and D. R. Pepalis, MSD)

The conditions for the 14 successfully completed DEH transient tests that have yielded useful fission-gas-release and fuel-characterization information are tabulated in Table II.1 along with anticipated tests for equivalent conditions from the initial DEH transient-test plan (see ANL-76-15, p. 45, Table II.1). Results from the first few tests confirmed the need for running well-controlled tests to central melting for all heating rates. Also, more tests were run short of melting at the slowest heating rate than were originally anticipated. High-burnup fuel has been tested at 25, 80, 200, and 430°C/s to central melting, and several tests have been run short of central melting (interrupted tests) at 25°C/s. Also, lower-burnup fuel has been tested to central melting at 25°C/s.

TABLE II.1. Summary of DEH Transient Tests Run to Date Using Robinson Fuel and Tests Originally Anticipated in the Initial Plan

	DEH Tests to Date					Minimum Number of Tests in Initial DEH Test Plan			
	High Burnup				Low Burnup	High Burnup			Low Burnup
$T_{℄}$ Ramp Rates (°C/s)	25	80	200	430	25	20	200	500	200
Condition at Start of Ramp							1		
50% Time to Center Melting	1								
60% Time to Center Melting	1						1		
80% Time to Center Melting	2					1	2	1	4
Incipient Center Melting	3	1	4	1	1	1	2	1	1
Fuel Failure							1		
Total Tests	7	1	4	1	1	2	7	2	5

The emphasis for running most of this first series of tests was shifted from a ramp rate of 200 to 25°C/s for two reasons. The conditions for the slower-heating-rate tests were easier to control, a big advantage during this early learning period. And the first PBF transient test of irradiated fuel by EG&G, IE-1,[5] was being run at 25°C/s, so we chose to heat at the same rate to facilitate the comparison of fission-gas release from electrically heated and neutronically heated fuel.

The number of variables in these tests made it difficult to make definitive correlations; qualitative correlations of the fraction of fission gas released with heating rate and time of transient for some of the test results were reported last quarter (see ANL-76-121, Figs. II.2 and II.3). To improve these and other correlations and to improve the usefulness of the data to analytical

LIST OF FIGURES

No. Title

III.21. Maximum Rupture Circumferential Strain as a Function of Initial Internal Pressure for Axially Constrained and Unconstrained Cladding in Steam at a Heating Rate of 115°C/s . . . . .

III.22. Low- and High-magnification Scanning-electron Micrographs of a Zircaloy-4 Cladding Tube That Show Surface Irregularities Formed by β-phase Grain-boundary Sliding. . . . .

III.23. Micrograph of the Cross Section in the Ballooned Region of a Zircaloy-4 Tube Ruptured at 1050°C in Vacuum at a Heating Rate of 115°C/s That Shows OD and ID Irregularities Formed by Grain-boundary Sliding . . . .

III.24. Typical Cross Section of a Zircaloy-4 Tube That Burst at a Temperature in the β-phase Region in a Steam Environment . .

III.25. Magnified Cross Section of the Specimen in Fig. III.24 That Shows (A) Symmetry of the Cusp at the OD Surface, the Length L_N between Cracks in the Oxide, and Thinning of the Tube Wall Opposite the Cusp and (B) the Rupture Area . . . . . .

III.26. Optical Micrograph That Shows a β-phase Grain Boundary Located at the Moving Front of a Cusp Similar to That in Fig. III.25A . . . .

III.27. Cross Section of a Zircaloy-4 Tube Oxidized in Steam for 48 s at 1154°C without Internal Pressure and Ruptured at This Temperature in 0.25 s. . . . .

III.28. Scanning-electron Micrograph of the Fracture Surface of the Specimen Described in Fig. III.27 . . . .

III.29. Schematic Representation of the Deformation and Rupture Sequence for Zircaloy Cladding in a Steam Environment at Temperatures $\gtrsim$1000°C . . . .

III.30. Resistivity-vs-Temperature Curves for a Zircaloy-4 Specimen with 0.425 wt % Oxygen Obtained at Constant Heating and Cooling Rates through the $\alpha + \beta$ Phase Region . . . .

III.31. Comparison of the Time-Temperature-Transformation Curves from the Quenching and Metallographic Studies of Östberg with Resistometric Data Obtained for Zircaloy-2 . . . .

III.32. Time-Temperature-Transformation Diagram for As-received Zircaloy-4 . . . .

III.33. Martensitic Structure of As-received Zircaloy-4 after Cooling through the $\beta \rightarrow \alpha'$ Transformation at ~10,000°C/s from 1000°C .

modeling, better knowledge and control of test conditions were required. Therefore a systematic series of PCM-like tests is being run to, and short of, melting under as closely identical test conditions as our current capability permits. The first group of this series of tests is being run at a heating rate of 25°C/s. The number of tests needed at higher heating rates will be determined when the results of the low-heating-rate tests are known. This series of tests should result in improved reproducibility between tests and should permit more quantitative correlations of fission-product release with time of transient, temperature achieved, heating rate, burnup, and other fuel and test conditions.

Not enough data are available from this series of tests to justify reporting detailed results at this time. Since not enough fuel was left from the F-7 Robinson rod that has been used to date, rod G-6 is being used for this test series. Gamma-scan results for rod G-6 have been reported (see ANL-76-49, p. 28), and a chemical analysis is being made for total retained fission gas by the method described in ANL-76-87 (p. 32). The technique for recovering DEH specimens has been found to work as well for rod G-6 as it has for rod F-7.

Tests 26 and 27 were designed to be run to central melting at a heating rate of 25°C/s. Difficulties in the measurement of the fuel surface temperature in both tests revealed deficiencies in our thermocouple and optical-pyrometer techniques. Improvements have since been made in the technique for attaching the thermocouple bead to the fuel surface and in the electrical circuit for the readout from the optical pyrometer.

The temperature-measurement difficulties during these tests resulted in questionable temperature data and nonstandard preheating of the specimens before running the thermal transients. The data were inadequate to permit calculation of the temperature profile or the central temperature. However, released fission gas was collected and analyzed, and all other aspects of the tests worked well. The metallographic examinations are not completed so the extent of central melting is not yet known.

The specimen for Test 27 was inadvertently preheated for 8-9 min at a temperature that appeared to be hot enough to have caused significant movement of fission gases before the planned transient. The specimen for Test 26 was also overheated before the transient, but to a lower temperature and for a much shorter time. In both of these tests, the same amount of krypton was released as was released from Test 21, which had been heated to central melting at 25°C/s (see ANL-76-87, p. 16). However, considerably less xenon was released in Test 27 than in Test 21, and only half as much xenon was released in Test 26 as in Test 27. These results appear to be consistent with the apparent greater mobility of krypton than xenon that was discussed last quarter (see ANL-77-121, p. 71), but the observed differences in xenon release are yet to be explained.

DEH Test 25 was run to central melting at 25°C/s on a specimen from fuel rod F-7 that had about half the burnup of the previously DEH-tested high-burnup specimens from this rod. Surface temperatures of the fuel at the beginning of the test were not obtained because of thermocouple difficulties. The amount of released xenon and krypton and their ratio are about what would be expected based on qualitative comparison with the released fission gas from tests of high-burnup fuel. Quantitative comparisons are being made.

2. DEH/PBF Cross-check (S. M. Gehl and L. R. Kelman, MSD)

At the request of NRC-RSR (ANL-76-121, p. 48), ANL and EG&G proposed a joint program for cross-checking the behavior of LWR fuel and the release of fission gas observed in the EG&G in-reactor transient tests with that observed in the ANL out-of-reactor transient tests.[1] The first transient tests by nuclear heating of experimental fuel rods in the PBF IE-1 test[5] have been reported as showing apparent low fission-gas release[6] and little intergranular separation.[7] These results do not agree with the high gas release and extensive grain-boundary separation observed in our DEH-simulated transient tests of commercial fuel (see ANL-76-87, p. 20, and ANL-77-121, p. 72). An understanding of these diverse observations is important to the development of models for the transient behavior of LWR fuel rods and to the planning of experiments in PBF.

Near-term and follow-on activities were proposed. The near-term activities, which have been approved by NRC/RSR,[2] are intended to determine, with a minimum of effort, the reasons for the differences in behavior of the fuel and fission gases in the PBF and DEH transient tests. Follow-on activities were also proposed in anticipation of the possibility that convincing comparisons cannot be made using the fuel and test conditions that have been selected for the near-term activities. The proposed follow-on activities would also develop more quantitative information to benefit both the cross-check effort and the on-going fission-gas release programs at ANL and EG&G.

To understand the differences in the behavior of fuel and fission products between tests that use nuclear and electrical heating, the cross-check program proposes to perform DEH transient tests under thermal conditions that are comparable to those used in the PBF using the same fuel as that tested in the PBF. In addition to temperature ramp rate, the radial profiles of temperature and stress, which may influence transient fuel behavior and fission-gas release, should be duplicated in the PBF and DEH cross-check tests. The PBF IE-1 test was run under hypothetical PCM-accident conditions at a heating rate of 25°C/s. A 12.5%-enriched experimental fuel was used, identified as Saxton Load Follower (SLF) fuel,[8] to achieve the necessary power input in the PBF transient test.

The same heating rate and similar thermal gradients have been achieved in the DEH transient tests in which the maximum fission-gas release

and grain-boundary separation have been observed. The fuel used in the DEH tests is from 2.55%-enriched commercial PWR fuel rods from the H. B. Robinson reactor. This enrichment is too low to permit achievement of the desired thermal conditions if transient-tested in the PBF. As a result, the Robinson fuel is not suitable for the cross-check tests.

Although the desired temperature ramp rates and radial profiles can be attained for SLF fuel under both nuclear and electrical heating conditions, two additional considerations may affect transient fuel behavior and gas release. First, the SLF fuel was irradiated at a higher linear power rating than the Robinson fuel and, therefore, is expected to have less retained fission gas. Second, fuel rods are tested in the PBF, whereas only bare fuel pellets have been DEH-tested to date, resulting in a lack of radial constraint in the latter.

The near-term effort will be implemented at ANL-East using irradiated SLF fuel from the PBF program. The amount of retained fission gas will be determined in sibling and PBF-tested SLF fuel. If useful DEH specimens cannot be obtained from the sibling SLF fuel rods using existing techniques, modified techniques will be developed. DEH tests will be run on the sibling SLF fuel using the slow heating rate (25°C/s) and other experimental conditions that resulted in high gas release from Robinson fuel. The released fission gas will be analyzed, and the PBF- and DEH-tested fuel will be examined for grain-boundary separation and fissuring and for fission-gas bubble location and interlinkage. This course of action is considered a minimum effort to resolve the observed differences between PBF- and DEH-test results.

The sibling SLF fuel will be considered unsuitable for this cross-check program if useful DEH test specimens cannot be obtained from the pins. In that event, it will be necessary to use a fuel that meets this criterion and is enriched enough to provide the necessary transient power in the PBF. The low-burnup, low-power MAPI (Mitsubishi Atomic Power Industries, Inc.) fuel pins,[8] which may be included in the PBF transient-test program, have been considered. Our experience indicates that useful DEH fuel specimens can be recovered from MAPI fuel pins by the method developed for Robinson fuel pins. However, the 5.7% enrichment may not be high enough to achieve the necessary fuel thermal conditions in the PBF.

The use of another type of fuel in the near-term cross-check program will extend the scope of the on-going PCM-like DEH test series (see Sec. B.1 above), thereby helping to verify the validity of the DEH input to the GRASS code. GRASS gas-release and swelling calculations, in conjunction with the FRAP codes, will be used to aid in the interpretation of DEH and PBF experimental results and will serve as a link between the two programs. In addition, the improved data base generated in the cross-check program will be used to verify the code, further develop the model, and better establish the credibility of the analyses for actual LWR-accident conditions.

EG&G is preparing fuel samples for shipment to ANL-East early in January 1977 as follows: (1) two sibling SLF fuel rods, (2) two MAPI fuel rods, and (3) sections from the bottom and from above and below the nucleate and film-boiling boundary of the central sections of two SLF fuel rods from the IE-1 PBF test. Cut-up diagrams, radiographs, and photographs of this fuel have been received from EG&G.[9]

References

1. J. G. Crocker, EG&G Idaho, Inc., private communication to P. E. Litteneker, ERDA-ID (Oct 28, 1976).
2. W. V. Johnston, NRC, Silver Spring, MD, private communication (Dec 10, 1976).
3. R. V. Churchill, Fourier Series and Boundary Value Problems, McGraw-Hill Book Company, Inc., New York, pp. 102-4 (1941).
4. R. G. Bellamy and J. B. Rich, Grain-Boundary Gas Release and Swelling in High Burn-up Uranium Dioxide, J. Nucl, Mater. 33, 64-76 (1969).
5. EG&G Idaho, Inc., Quarterly Technical Progress Report on Water Reactor Safety Programs Sponsored by the Nuclear Regulatory Commission's Division of Reactor Safety Research, April-June 1976, TREE-NUREG-1004, p.45.
6. W. J. Quapp and R. K. McCardell, EG&G Idaho, Inc., Behavior of Zircaloy Clad UO_2 Fuel Rods during Film Boiling in a PWR Environment, presented at the OECD-CSNI Specialists Meeting on the Behavior of Water Reactor Fuel Elements under Accident Conditions, Spatind, Norway (Sept 1976).
7. W. J. Quapp, EG&G Idaho, Inc., private communication (Dec 1976).
8. Aerojet Nuclear Company, Characteristics of UO_2-Zircaloy Fuel Rod Materials from Saxton Reactor for Use in Power Burst Facility, ANCR-NUREG-1321 (Sept 1976).
9. W. J. Quapp, EG&G Idaho, Inc., private communication to L. R. Kelman, ANL (Dec 6, 1976).

III. MECHANICAL PROPERTIES OF ZIRCALOY CONTAINING OXYGEN

H. M. Chung, A. M. Garde, and T. F. Kassner, MSD

A. Summary

Uniaxial and biaxial mechanical-property data on Zircaloy-4 are being obtained over a wide range of temperature and strain rate to establish a more quantitative cladding-embrittlement criterion applicable to postulated loss-of-coolant-accident (LOCA) situations in light-water reactors (LWR's). The mechanical-property information will be incorporated into fuel-element modeling codes that will provide a quantitative basis for evaluating cladding deformation over a wide range of LOCA and power-coolant-mismatch (PCM) conditions.

The effect of cooling rate through the $\beta \rightarrow \alpha'$ transformation on the uniaxial tensile properties of as-received Zircaloy-4 has been investigated at temperatures between 25 and 800°C. Specimens were heated to 1000°C and quenched or cooled at several rates between ~0.1 and 250°C/s to produce different microstructures in the material, i.e., basketweave, parallel plate, and lenticular. In general, the ultimate tensile and 0.2% yield strengths increase with an increase in cooling rate, whereas the uniform and total strains are somewhat higher at a cooling rate of ~10°C/s (basketweave structure) than at the extremes of the cooling rate range for the different test temperatures. The total and uniform strains also exhibit a maximum at ~200°C for all the cooling rates investigated. The effect of oxygen redistribution on the tensile properties at 400°C was investigated for material that was oxidized to a total oxygen content of ~4 wt % at 1000 and 1100°C and cooled through the $\beta \rightarrow \alpha'$ transformation at different rates.

Additional information has been obtained on the diametral expansion and rupture characteristics of axially constrained and unconstrained Zircaloy-4 cladding in a steam environment. Measurements of the maximum circumferential strain for axially constrained cladding at a heating rate of 55°C/s indicate that the circumferential expansion is slightly higher in steam than in vacuo for rupture temperatures below ~800°C, but smaller at higher temperatures.

The relationship between maximum circumferential strain and burst temperature for unconstrained cladding has been determined at a heating rate of 115°C/s in steam. For burst temperatures between ~800 and 1300°C, the circumferential strain for unconstrained cladding was approximately a factor of two greater than for the constrained case. The dependence of the burst temperature on the initial internal pressure was virtually identical for the constrained and unconstrained cladding in the steam environment.

Regions of the cladding wall that experienced localized thinning during ballooning deformation in steam at high temperatures have been examined

metallographically. The observations indicate that most of the circumferential expansion occurs in these regions, which are associated with a crack in the $ZrO_2 + \alpha$ layers at the site of a β-phase grain boundary. Fracture of the cladding occurs by intergranular tearing of the β-grain boundary.

Resistivity data on as-received Zircaloy-4 and homogeneous Zircaloy-oxygen alloys, obtained at linear heating and cooling through the $\alpha + \beta$ phase region, are being used to construct time-temperature-transformation (TTT) diagrams for the materials. The TTT diagram for as-received Zircaloy-4 with 0.14 wt % oxygen has been established by this method. A correlation of the cooling rate through the $\beta \rightarrow \alpha'$ transformation with the microstructure has also been obtained. This information will be useful in establishing microstructures in mechanical-test specimens that are representative of those in Zircaloy fuel cladding after an LOCA reflood.

B. Effect of Microstructure and Oxygen Concentration on the Uniaxial Tensile Properties of Zircaloy-4

1. Scanning-electron-microscopy Investigation of As-received Zircaloy-4 Specimens Deformed at 850°C

To supplement the previously reported work[1] on the mechanism of superplastic deformation in Zircaloy at 850°C, surfaces of deformed tensile specimens were examined by scanning-electron microscopy. Figure III.1 is a micrograph of the surface (thickness direction) of a Zircaloy-4 specimen deformed at the strain rate of $3.3 \times 10^{-1}\ s^{-1}$ at 850°C. The broad slip lines within the grain imply that transgranular deformation occurred via dislocation slip at this strain rate. The absence of a large offset at the grain boundary separating the two grains indicates that grain-boundary sliding is not important in stage-III deformation.[1]

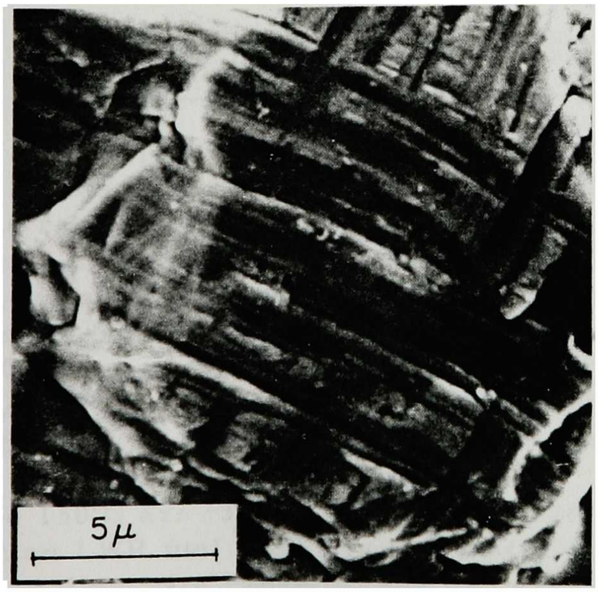

Fig. III.1

Slip Lines on the Surface of a Zircaloy-4 Specimen Deformed at 850°C, $\dot{\varepsilon} = 3.3 \times 10^{-1}\ s^{-1}$. Neg. No. MSD-63846.

A surface microstructure for a specimen deformed at a strain rate of 3.3 x 10^{-6} s^{-1}, in the stage-II region, is shown in Fig. III.2. In this case, step formation at the grain boundary is significant, which indicates the importance of grain-boundary sliding. The fine crystalline faceting within the grains is due to thermal etching of the surface during the long test time in a vacuum environment at high temperature.

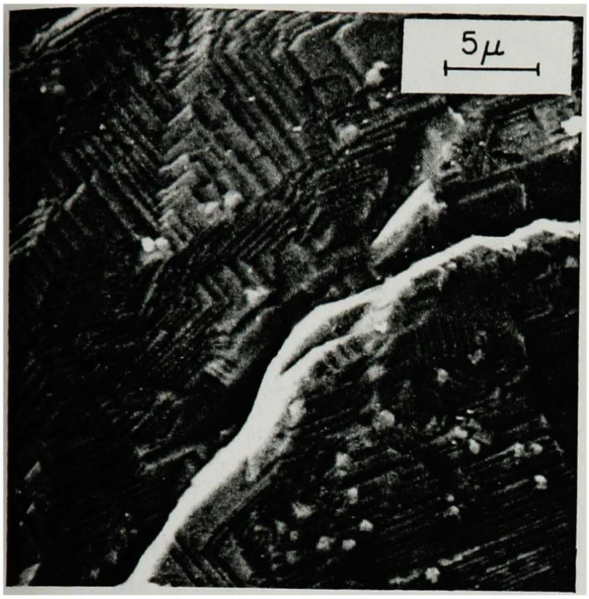

Fig. III.2

Facets due to Thermal Etching of the Surface of a Zircaloy-4 Specimen Deformed at 850°C, $\dot{\varepsilon}$ = 3.3 x 10^{-6} s^{-1}. Neg. No. MSD-63845.

Faceting was also observed on samples exposed to a vacuum at 850°C without any deformation. Note the multiplicity of the crystalline planes brought out by thermal etching; i.e., the steps in Fig. III.2 are sharper and finer than the slip lines shown in Fig. III.1. The absence of slip lines in Fig. III.2 implies that, at this low strain rate, intercrystalline deformation due to dislocation slip is not important. The observed grain-boundary sliding is accommodated by diffusion creep.

The microstructural observations from specimens deformed at the two strain rates at 850°C are consistent with earlier conclusions[1] that grain-boundary sliding accommodated by diffusion creep is important in the stage-II region and that transgranular deformation due to dislocation motion occurs during stage-III deformation.

2. Effect of Cooling Rate through the $\beta \rightarrow \alpha'$ Transformation on the Tensile Properties of As-received Zircaloy-4

In Ref. 2, it was shown that the mechanical properties of transformed β-phase Zircaloy are dependent on the cooling rate through the two-phase region. In laboratory experiments, different microstructures can be produced in the material by varying the cooling rate over a wide range. For example, when a Zircaloy tube is electrically heated to ~1000°C in a beaker of water and the power is switched off, a cooling rate of ~170°C/s through the ~980 to 805°C temperature range was obtained from the response of 0.25-mm Chromel/Alumel thermocouples that were spark-welded to the cladding. A typical cooling curve obtained from the emf-time response of a Visicorder is shown in Fig. III.3. The cooling rates for temperature ranges of ~650 to 500 and 500 to 150°C are ~300 and 800°C/s, respectively. On the basis of stored energy in an LWR fuel rod and the heat-transfer conditions during reflood, the expected cooling-rate range for the fuel cladding following a hypothetical LOCA is 1-5°C/s[3,4] at temperatures in the $\alpha + \beta$ phase region.

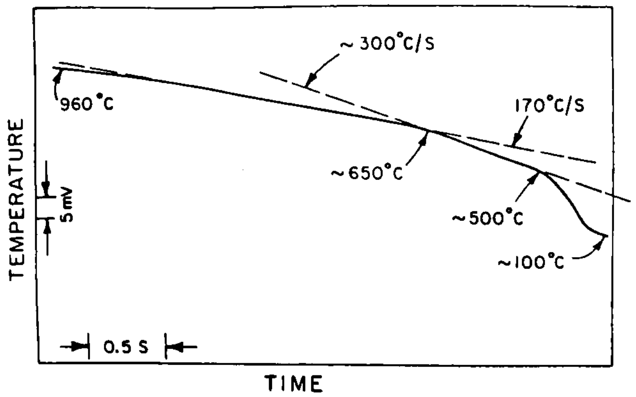

Fig. III.3. Temperature–Time Curve for a Resistance-heated Zircaloy-4 Tube Cooled from 1030°C in Water. Neg. No. MSD-63841.

Figures III.4-III.7 show the cooling-rate dependence of the 0.2% yield stress, ultimate tensile strength (UTS), uniform strain, and total strain, respectively, at several temperatures between 25 and 800°C. The 15-μm grain-size Zircaloy-4 specimens with 0.11 wt % oxygen have a width-to-thickness ratio (w/t) of 5.

The transformed β structure was obtained by heating the as-received equiaxed homogeneous α-Zircaloy to a temperature within the β-phase field (1000°C) and then cooling the specimen through the two-phase region (805-980°C) at the designated cooling rate. Cooling rates of <3°C/s could be achieved in the Instron furnace, prior to mechanical testing. The microstructures associated with the faster cooling rates (>3°C/s) were produced by annealing and quenching in another furnace, and the specimens were reheated to the mechanical-test temperature in the Instron furnace. The microstructural morphology obtained at the different cooling rates is described in Sec. III.D.2.

The results show that, as the cooling rate increases, both the yield stress (Fig. III.4) and the UTS (Fig. III.5) increase. Two factors responsible for the somewhat higher strength for the material transformed at faster cooling rates are the finer structure and less oxygen (and other alloying element) redistribution. Considerable oxygen redistribution occurs[5] at the slower cooling rates (<1°C/s), so that the central portions of α' plates become enriched in oxygen and the boundary region between two adjacent α' plates is depleted in oxygen. The structure obtained at the cooling rate of 250°C/s is quite fine compared with the lenticular structure produced at a cooling rate of 0.09°C/s.

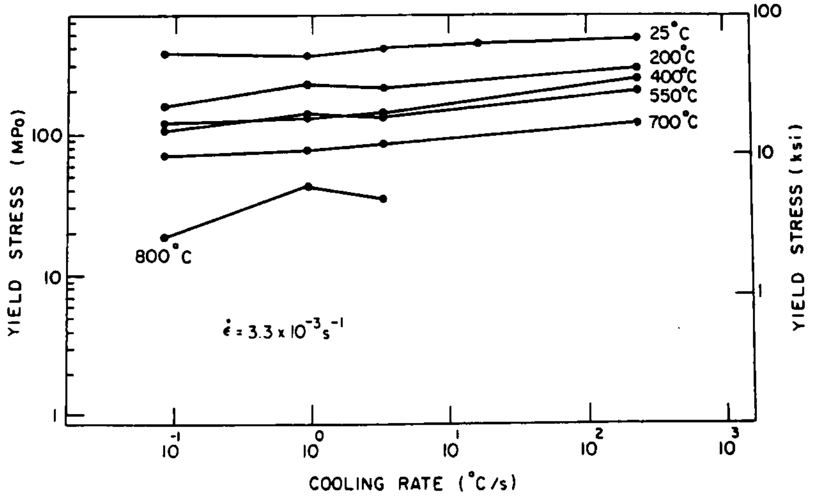

Fig. III.4

Effect of Cooling Rate on the Yield Stress of Transformed β-phase Zircaloy-4 at Several Temperatures. Neg. No. MSD-63835.

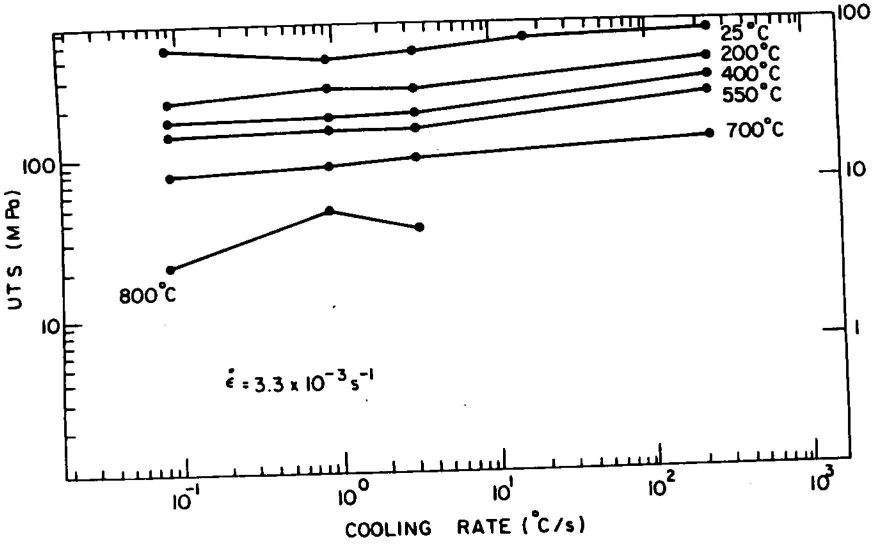

Fig. III.5. Influence of Cooling Rate on the UTS of Transformed β-phase Zircaloy-4 at Several Temperatures. Neg. No. MSD-63847.

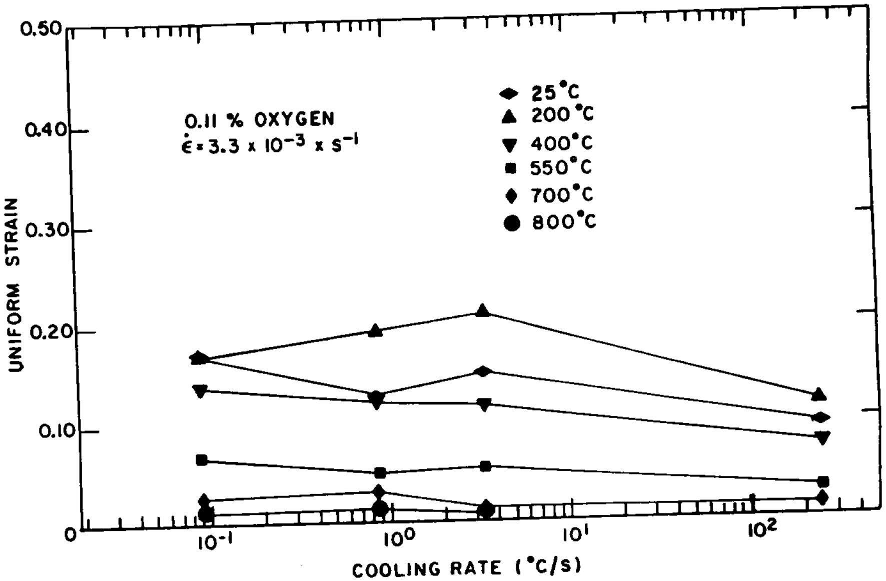

Fig. III.6. Cooling-rate Dependence of Uniform Strain of Transformed β-phase Zircaloy-4 at Several Temperatures. Neg. No. MSD-63842.

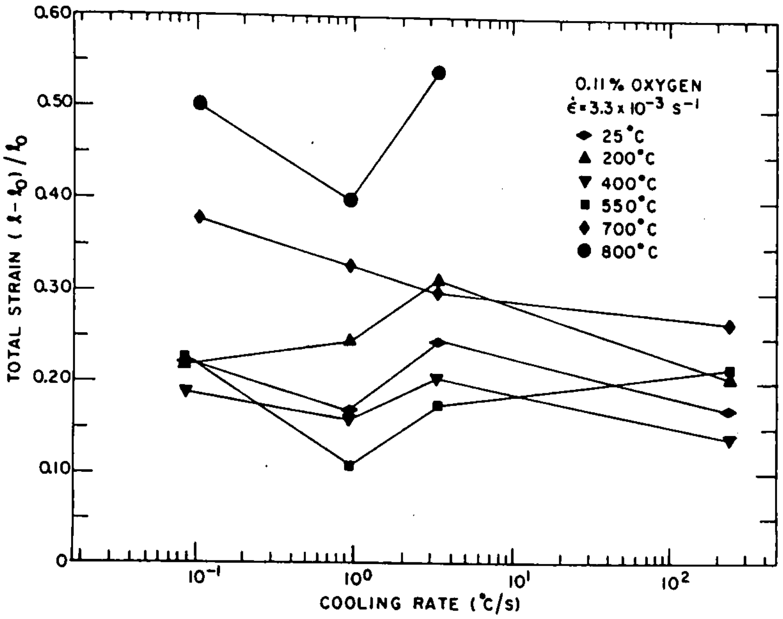

Fig. III.7. Total Strain as a Function of Cooling Rate for Transformed β-phase Zircaloy-4 at Several Temperatures. Neg. No. MSD-63844.

The data in Figs. III.6 and III.7 show that the intermediate basketweave/parallel-plate structure formed at a cooling rate of 3°C/s exhibits a higher uniform and total strain. The uniform strain of the basketweave structure (Fig. III.6) is larger at 200°C than at 25 and 400°C. This is probably due to the higher work-hardening rate associated with dynamic strain aging at 200°C. We can conclude from the mechanical-property data in Figs. III.4-III.7 that the basketweave structure exhibits both good strength and good ductility.

The temperature dependence of the uniform and total strain is shown in Figs. III.8 and III.9, respectively, for specimens cooled at different rates through the phase transformation. The peak in the uniform strain at 200°C (Fig. III.8) is associated with dynamic strain aging. As the temperature increases, the uniform strain decreases rapidly as a result of the decrease in work-hardening rate and the larger extent of dynamic recovery at higher temperatures. Dynamic strain aging results in a minimum in the total strain at temperatures between 400 and 550°C.

3. Effect of Oxygen Concentration and Cooling Rate through the $\beta \rightarrow \alpha'$ Transformation on the Tensile Properties of Zircaloy

To investigate the effect of oxygen concentration and microstructure produced by cooling through the $\beta \rightarrow \alpha'$ phase transformation, several tensile specimens were oxidized in oxygen at reduced pressure to an average oxygen concentration of 4.0 and 4.4 wt % at 1100 and 1000°C, respectively. Since the oxygen-charging furnace did not have a quenching facility, the composite specimens were cooled at ~0.15°C/s through the phase transformation, which resulted in a coarse lenticular structure in the central α' region of the

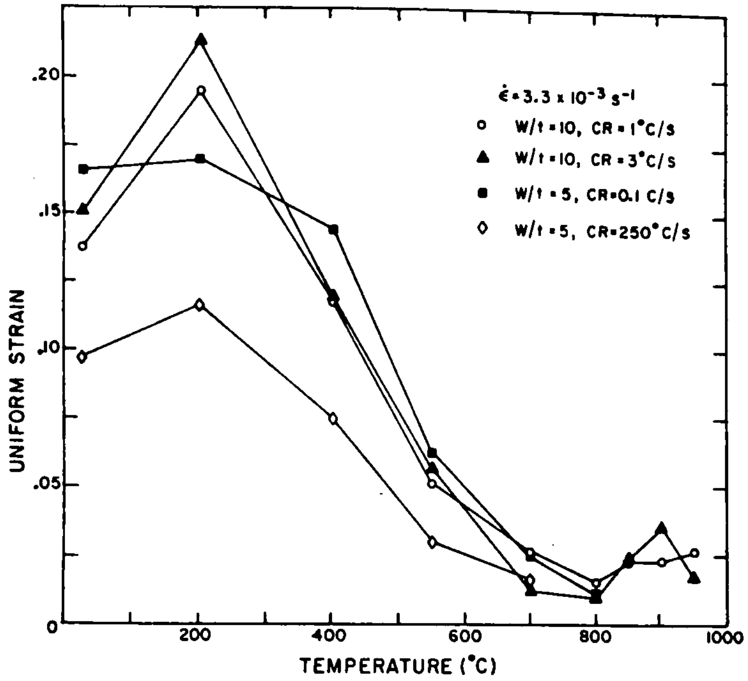

Fig. III.8. Uniform Strain vs Temperature for Transformed β-phase Zircaloy-4 at Various Cooling Rates. Neg. No. MSD-63843.

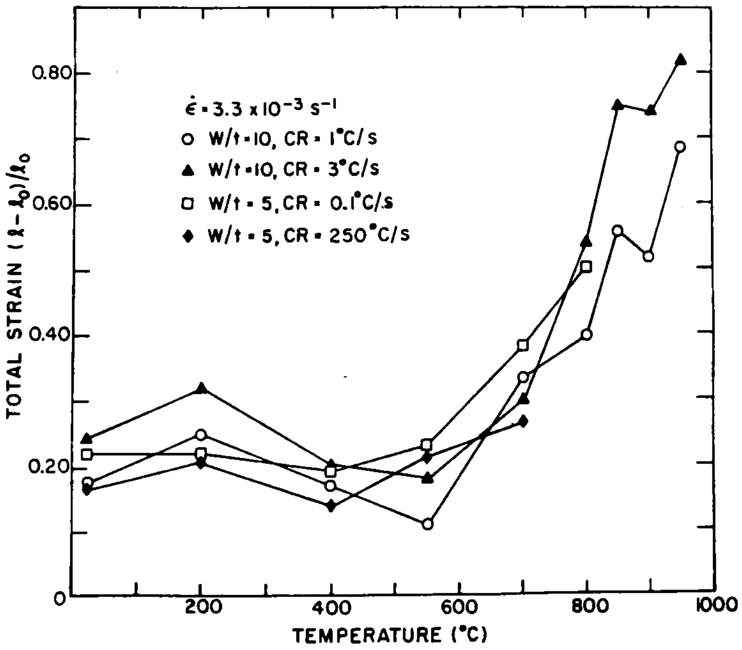

Fig. III.9. Total Strain as a Function of Temperature for Transformed β-phase Zircaloy-4 at Various Cooling Rates. Neg. No. MSD-63838.

specimens. To obtain microstructures representative of other cooling rates through the phase transformation, specimens were placed in another furnace, rapidly heated into the β-phase field, and quenched or cooled to room temperature at different rates. Because of this oxygen-charging method, the microstructure and oxygen distributions in the specimens, particularly at the 250°C/s cooling rate, are not solely dependent on the final cooling rate through the phase transformation.

The strength and ductility of the material with 4.0 wt % oxygen, in Figs. III.10 and III.11, respectively, are quite low, particularly at the 0.09°C/s cooling rate. Oxygen penetration into the material at the 1100°C charging temperature and the significant amount of oxygen redistribution that occurred during slow cooling through the phase transformation cause a degradation in the properties. As the cooling rate increases, both the strength and ductility increase; however, the total strain is quite small (<0.02) at all cooling rates.

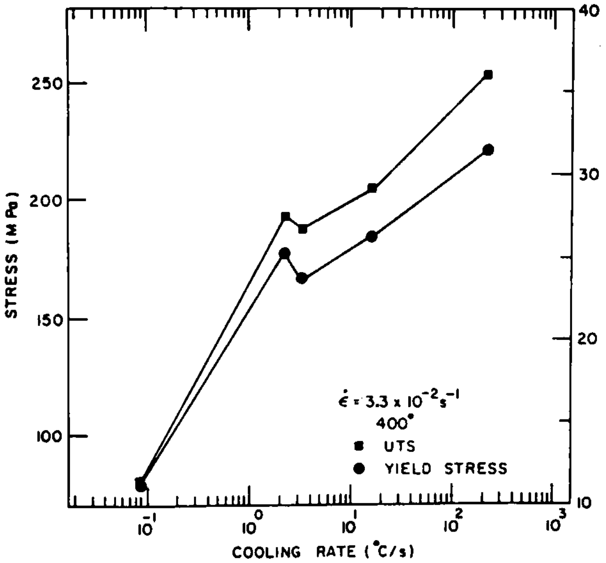

Fig. III.10. Dependence of Yield Stress and UTS on Cooling Rate for Composite Zircaloy-4 Specimens with 4.0 wt % Oxygen. Neg. No. MSD-63837.

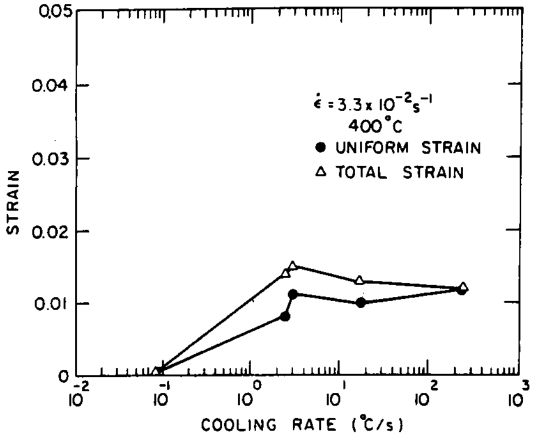

Fig. III.11. Uniform and Total Strain as a Function of Cooling Rate for Composite Zircaloy-4 Specimens with 4.0 wt % Oxygen. Neg. No. MSD-63836.

The yield stress and UTS of the specimens with 4.4 wt % oxygen, in Fig. III.12, are not strongly dependent on the cooling rate. The ductility data in Fig. III.13 show a peak at a cooling rate of ~17°C/s. Despite the somewhat higher total oxygen concentration (4.4 wt %) in these specimens, the ductility is significantly higher than for the composite material with 4.0 wt % oxygen. This observation implies that the time-temperature history is an important variable with regard to the mechanical properties. For specimens with 4.4 wt % oxygen, the oxidation temperature was 1000°C, and, consequently, oxygen diffusion into the central β (or two-phase) region occurred to a lesser extent than in the material with 4.0 wt % oxygen, for which the oxidation temperature was 1100°C.

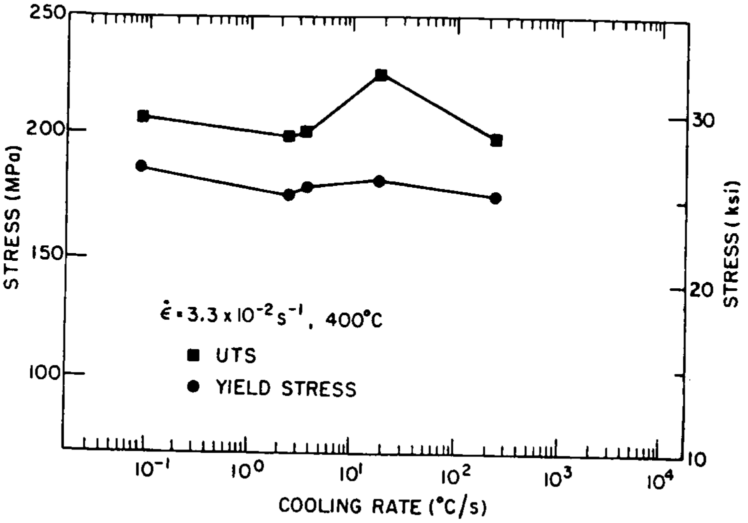

Fig. III.12. Effect of Cooling Rate on the Yield Stress and UTS of Composite Zircaloy-4 Specimens with 4.4 wt % Oxygen. Neg. No. MSD-63839.

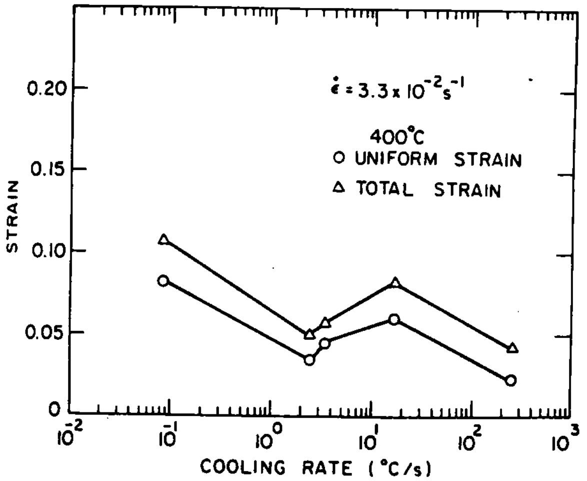

Fig. III.13

Influence of Cooling Rate on the Uniform and Total Strains of Composite Zircaloy-4 Specimens with 4.4 wt % Oxygen. Neg. No. MSD-63840.

C. Biaxial Deformation and Rupture Characteristics of Zircaloy-4 Cladding in Steam

1. Rupture Characteristics of Axially Constrained Cladding at a Heating Rate of 55°C/s

The biaxial deformation and rupture behavior of axially constrained Zircaloy-4 cladding has been investigated further at a heating rate of 55°C/s. A better definition of the effect of steam oxidation on the relationship between maximum circumferential strain and burst temperature is shown in Fig. III.14 for rupture temperatures between 700 and 850°C. The circumferential expansion is slightly higher in a steam environment than in vacuo for rupture temperatures below ~800°C, but smaller at higher temperatures. Figure III.15 shows the maximum circumferential strain as a function of the initial internal

pressure for a heating rate of 55°C/s in steam and vacuum environments. For a heating rate of 115°C, Fig. III.16 shows similar results, which have been modified from the curve reported in Ref. 6 by the inclusion of additional data[1] for rupture temperatures between 700 and 850°C.

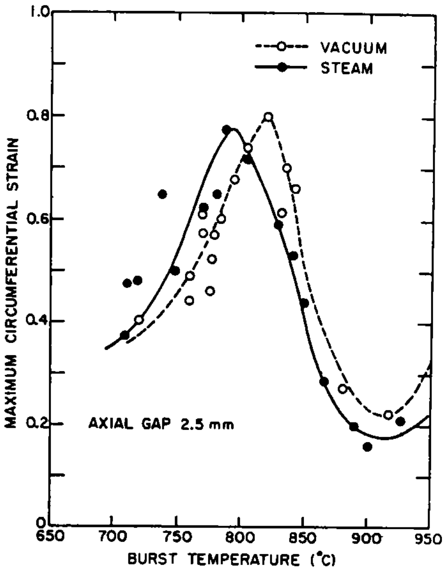

Fig. III.14

Maximum Circumferential Strain vs Burst Temperature for Axially Constrained Zircaloy-4 Cladding at a Heating Rate of 55°C/s in Steam and Vacuum Environments. ANL Neg. No. 306-77-20.

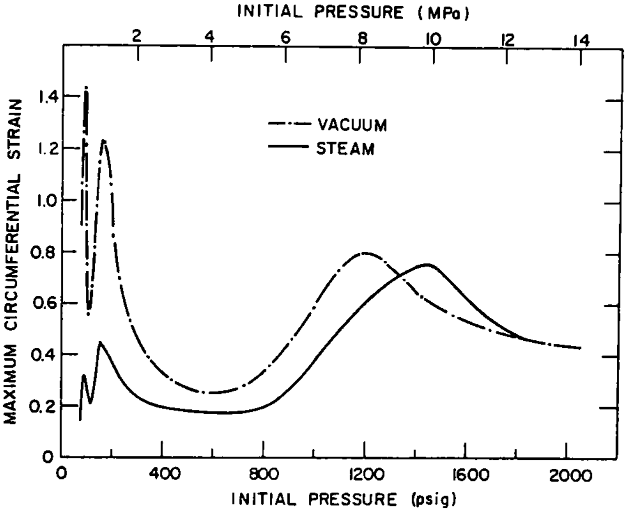

Fig. III.15

Maximum Rupture Circumferential Strain as a Function of Initial Internal Pressure for Axially Constrained Zircaloy-4 Cladding in Steam and Vacuum Environments at a Heating Rate of 55°C/s. ANL Neg. No. 306-76-152 Rev. 1.

Figure III.17 shows the effects of initial internal pressure and heating rate on the maximum circumferential strain for axially constrained cladding (2.5-mm axial gap) in a vacuum environment. This diagram was modified to include an additional small strain maximum for internal pressures near 9.7 MPa and for heating rates ≳90°C/s. Information concerning this strain maximum, which occurs at a burst temperature of ~790°C under severe axial constraint, was reported in Ref. 1. A revised plot of the circumferential expansion as a function of internal pressure and heating rate in a steam environment is shown in Fig. III.18, which includes more recent data at the 55°C/s heating rate.

2. Rupture Characteristics of Unconstrained Cladding at a Heating Rate of 115°C/s

Large differences were observed in the amount of circumferential expansion for constrained and unconstrained cladding in vacuum at a heating rate of 115°C/s, particularly for burst temperatures ≲850°C.[6] Figure III.19 shows a similar comparison for cladding ruptured in steam at this heating rate. Axial constraint results in a larger decrease in the circumferential strain in steam than in vacuo for rupture temperatures in the β-phase region, i.e., >980°C.

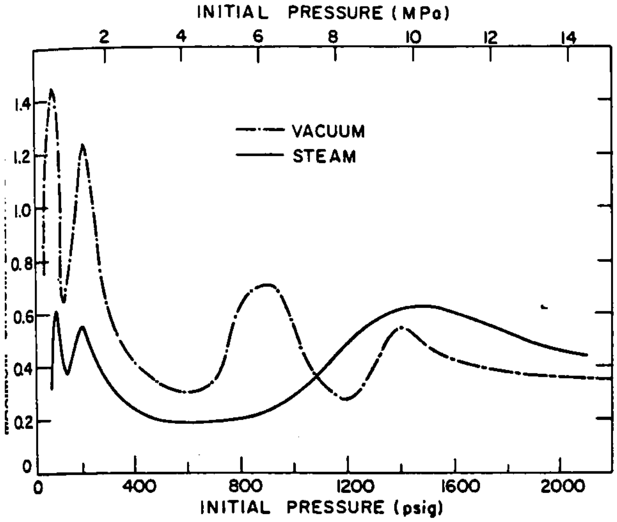

Fig. III.16. Maximum Rupture Circumferential Strain as a Function of Initial Internal Pressure for Axially Constrained Zircaloy-4 Cladding in Steam and Vacuum Environments at a Heating Rate of 115°C/s. ANL Neg. No. 306-76-156 Rev. 1.

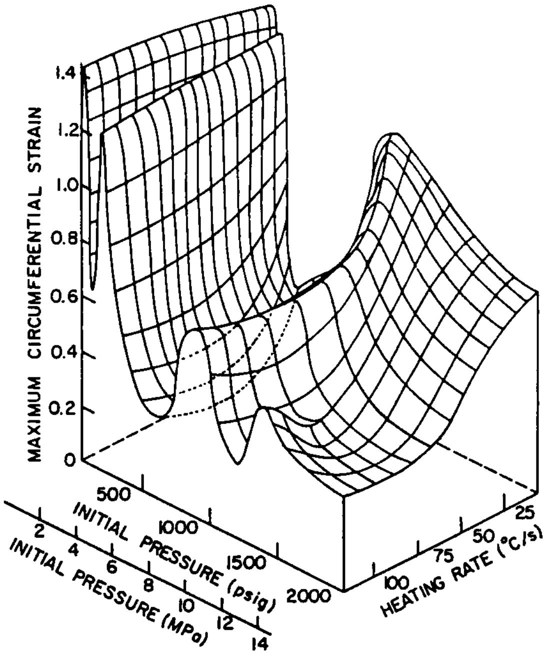

Fig. III.17. Effect of Initial Internal Pressure and Heating Rate on the Maximum Circumferential Strain for Axially Constrained Zircaloy-4 Cladding Burst In Vacuo. ANL Neg. No. 306-76-129 Rev. 2.

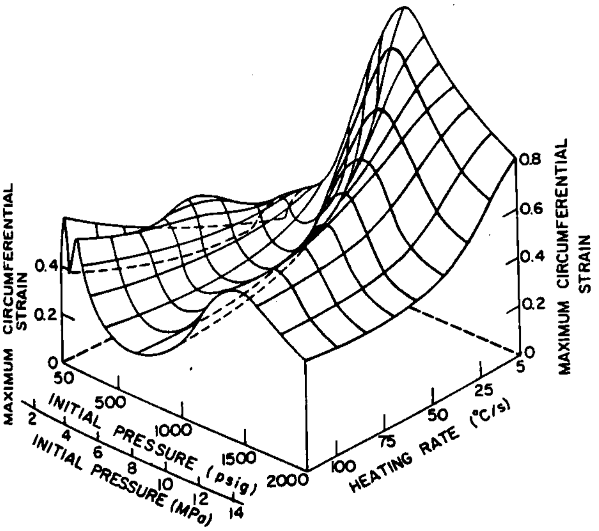

Fig. III.18. Effect of Initial Internal Pressure and Heating Rate on the Maximum Circumferential Strain for Axially Constrained Zircaloy-4 Cladding Burst in a Steam Environment. ANL Neg. No. 306-76-151 Rev. 1.

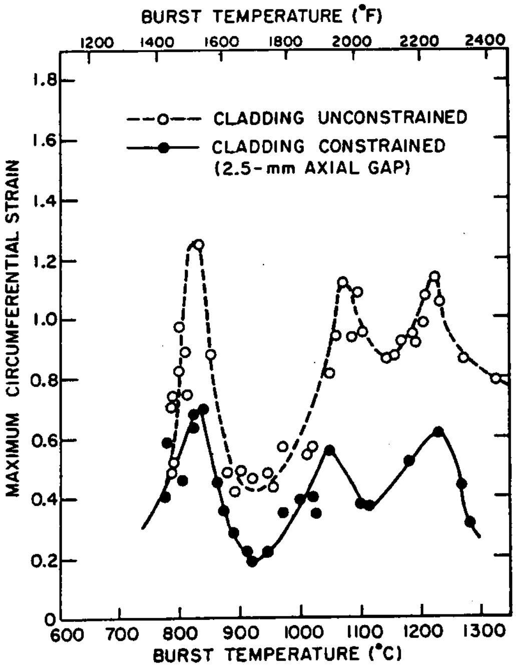

Fig. III.19. Maximum Circumferential Strain vs Burst Temperature for Axially Constrained and Unconstrained Cladding at a Heating Rate of 115°C/s in a Steam Environment. ANL Neg. No. 306-77-23.

Figure III.20 shows the relationship between initial internal pressure and the burst temperature for unconstrained and constrained cladding at a heating rate of 115°C/s. Similar behavior was reported for rupture tests in vacuo.[6] Strengthening of the cladding due to oxidation in steam is significant only at high temperatures, i.e., ≳1150°C.

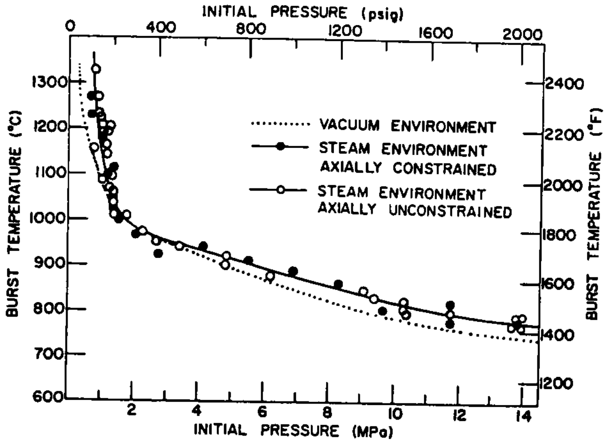

Fig. III.20

Burst Temperature as a Function of Initial Internal Pressure for Axially Constrained Zircaloy-4 Cladding in Steam and Vacuum and for Axially Unconstrained Cladding in Steam at a Heating Rate of 115°C/s. ANL Neg. No. 306-76-127 Rev.2.

Figure III.21 shows the maximum circumferential strain as a function of initial internal pressure for axially constrained and unconstrained cladding in steam at the high heating rate. The large difference in the circumferential expansion at ~9.6 MPa (1400 psi) is due to the deformation anisotropy of the α-phase material with the texture that resulted from fabrication of the tube.

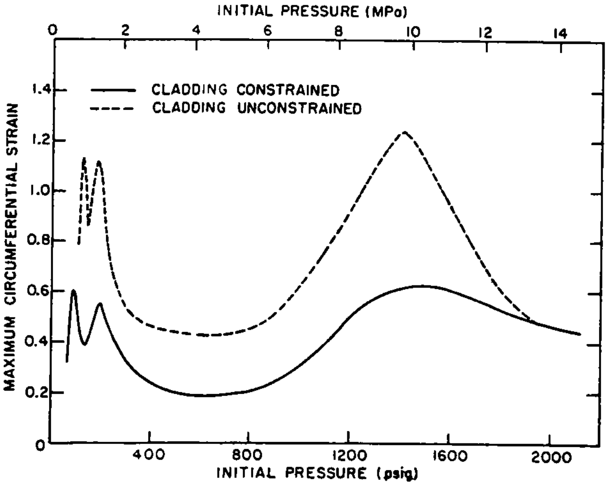

Fig. III.21

Maximum Rupture Circumferential Strain as a Function of Initial Internal Pressure for Axially Constrained and Unconstrained Cladding in Steam at a Heating Rate of 115°C/s. ANL Neg. No. 306-77-24.

3. Microstructural Evaluation of Localized Thinning of the Cladding Wall after Ballooning Deformation in Steam at High Temperatures

As reported in Ref.6, the deformation behavior of Zircaloy cladding in steam is quite different from that in vacuo above ~1000°C. The "orange-peel" surface appearance of cladding ruptured in vacuo above ~1000°C is no longer evident in a steam environment.

The average size of the "orange-peel" surface irregularities, also present on the inside surface of the tube, is comparable to the grain size of the β-phase cladding. When the cladding is deformed with a small internal pressure ($\leq$0.5 MPa), rupture occurs at a high temperature after a relatively long heating period. In this situation, β-phase grain growth is significant, and, hence, the "orange-peel" surface irregularities are much larger. Figure III.22 shows scanning-electron micrographs of the surface of a tube heated to 1255°C at 115°C/s, deformed for 38 s under an internal pressure of 0.29 MPa to a circumferential strain of 0.26, and cooled to room temperature without rupture occurring. Grain-boundary sliding in the β-phase material is evident from the micrographs.

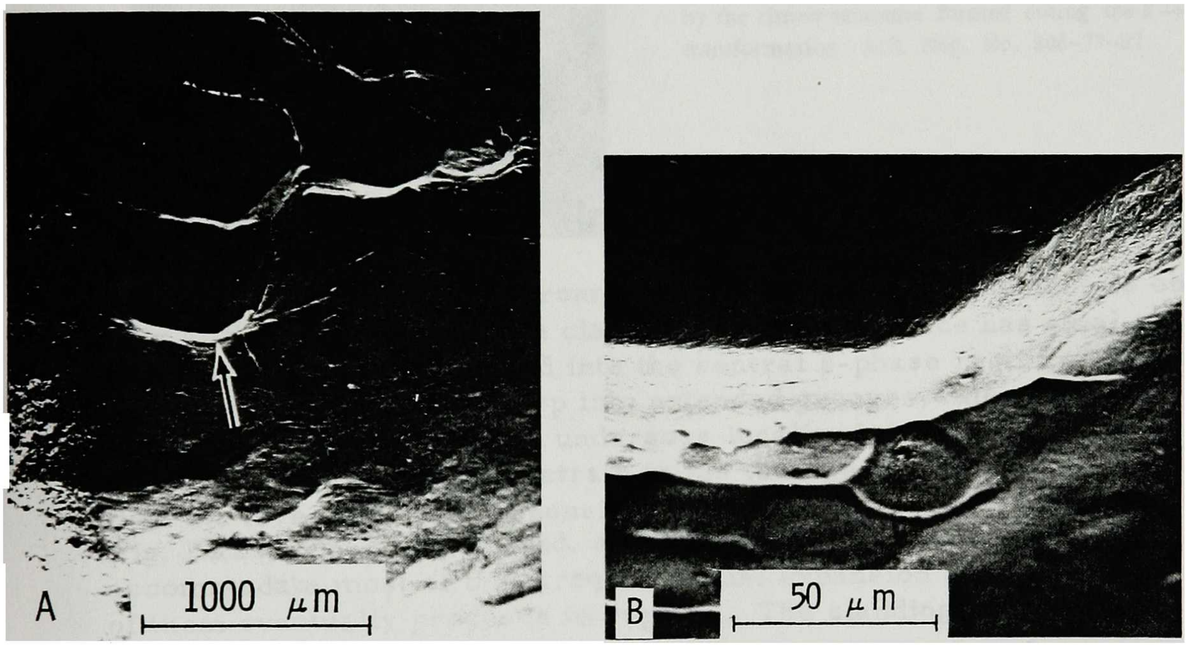

Fig. III.22. Low- and High-magnification Scanning-electron Micrographs of a Zircaloy-4 Cladding Tube That Show Surface Irregularities Formed by β-phase Grain-boundary Sliding. The tube was deformed in vacuum at 1255°C for 38 s under an internal pressure of 0.29 MPa to a Circumferential strain of 0.26. ANL Neg. No. 306-76-133.

The cross section of another tube, which ruptured at 1050°C at a heating rate of 115°C/s (maximum circumferential strain 1.25), is shown in Fig. III.23. Both the inside-diameter (ID) and outside-diameter (OD) surfaces show irregularities that result in the "orange-peel" appearance. In this specimen, the rim-α structure was formed at the grain boundaries of the previous β phase, and, thus, the β-phase grain structure can be clearly identified. As indicated by the arrows in Fig. III.23, the troughs of the surface irregularities coincide with β-phase grain boundaries. This indicates that grain-boundary sliding is the mechanism responsible for the "orange-peel" surface appearance.

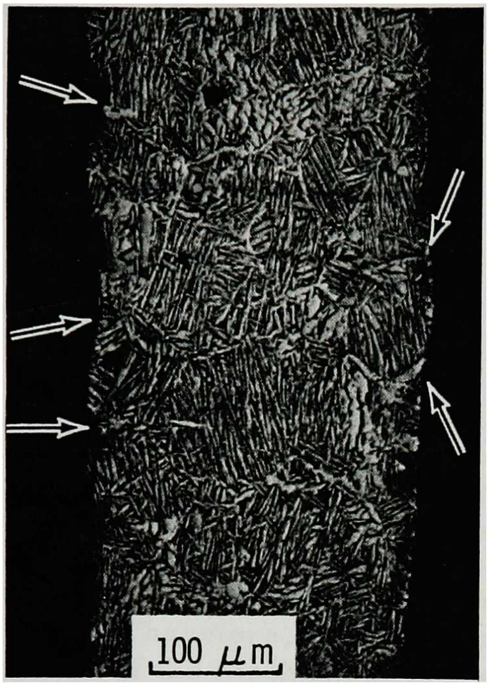

Fig. III.23

Micrograph of the Cross Section in the Ballooned Region of a Zircaloy-4 Tube Ruptured at 1050°C in Vacuum at a Heating Rate of 115°C/s That Shows OD and ID Irregularities Formed by Grain-boundary Sliding. Arrows indicate troughs at the surface, which are responsible for the "orange-peel" effect. The underlying β-phase grain boundaries are made evident by the rim-α structure formed during the $\beta \rightarrow \alpha'$ transformation. ANL Neg. No. 306-77-37.

In a steam environment, the "orange-peel" surface is observed only at the ID surface of the cladding. The OD surface has axial cracks in the oxide, and the cracks extend into the central β-phase region of the tube wall. Whenever the cracks develop into extended grooves,[6] the material at the ID surface opposite the cracks undergoes localized thinning or necking. These regions of localized radial strain in the tube wall (e.g., Fig. III.24) are larger than the irregularities responsible for the "orange-peel" appearance shown in Fig. III.23. The well-defined, smoothly shaped grooves on the OD surface accommodate most of the circumferential expansion of the cladding, and one of them eventually proceeds to rupture. The cladding cross section in

Fig. III.24

Typical Cross Section of a Zircaloy-4 Tube That Burst at a Temperature in the β-phase Region in a Steam Environment. The ID surface shows large irregularities, but the OD surface is relatively smooth with small grooves initiated by oxide cracking. ANL Neg. No. 306-77-28.

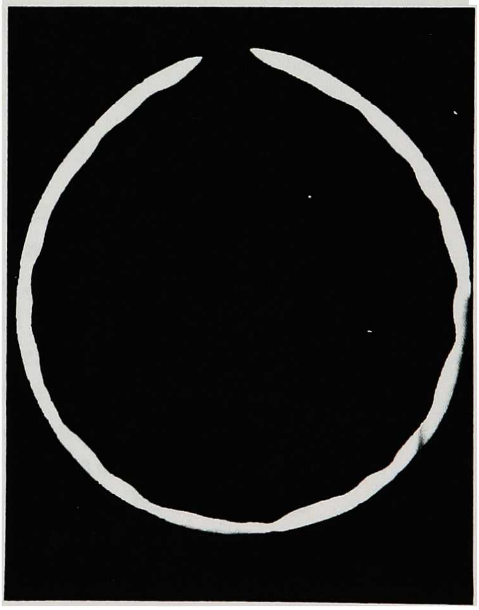

Fig. III.24 contains 51 such grooves, and an enlarged micrograph of one groove is shown in Fig. III.25. If we define the distance between two adjacent axial cracks in the oxide layer as L_N (Fig. III.25), the circumferential strain ϵ_θ^{ox} at which initial cracking of the oxide occurs can be calculated from the equation

$$\epsilon_\theta^{ox} = \frac{\sum_{N=1}^{N=N_{ox}} L_N}{\pi D_0} - 1, \qquad (1)$$

where N_{ox} is the total number of axial cracks around the circumference and D_0 is the initial cladding diameter. The circumferential strain at rupture from the cross section in Fig. III.24 is 0.21. The value of ϵ_θ^{ox} for this specimen, obtained from Eq. 1 and measurements of the L_N values from micrographs similar to Fig. III.25, is 0.025. Since this quantity is quite small, i.e., ~10% of the strain at failure, most of the circumferential expansion occurs in the groove regions. Therefore, the mechanism of β-phase deformation in steam can be explained if the mechanism of groove development is understood.

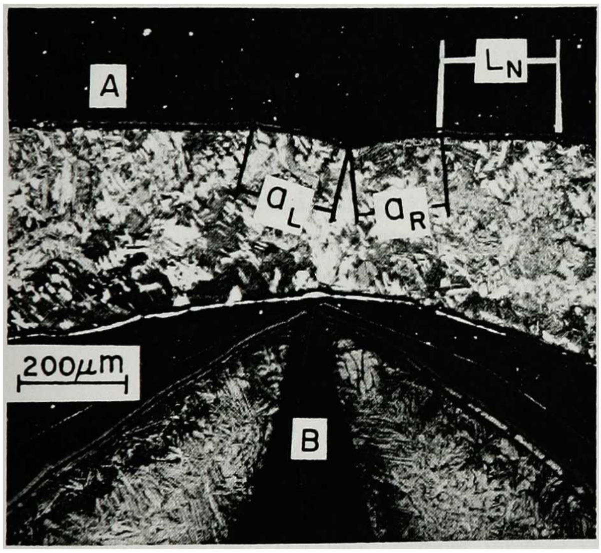

Fig. III.25

Magnified Cross Section of the Specimen in Fig. III.24 That Shows (A) Symmetry of the Cusp at the OD Surface, the Length L_N between Cracks in the Oxide, and Thinning of the Tube Wall Opposite the Cusp and (B) the Rupture Area. ANL Neg. No. 306-77-39.

Tearing is a frequently favored failure mechanism when small unbroken areas remain behind the main crack front as in Fig. III.25A. The left and right sides of the well-defined cusp are the same length, i.e., $a_L = a_R$ in Fig. III.25A, and the fracture tip is also symmetrical (Fig. III.25B). The thicknesses of the oxide and α layers at both sides of a groove decrease as the cusp is approached, which indicates that the exposure time to steam was identical for the both sides of the cusp. On the basis of these observations, it is believed that a groove advances by slow tearing of the β-phase material at the location of a crack in the oxide and α layers. A β-phase grain boundary is frequently observed at the location of the cusp of an advancing groove, e.g., Fig. III.26 for a cladding tube that ruptured at 1280°C.

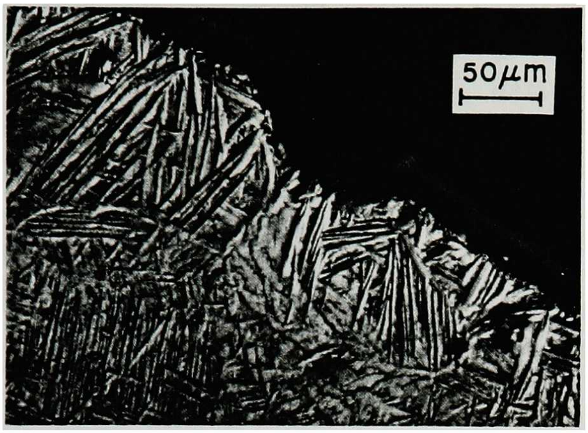

Fig. III.26

Optical Micrograph That shows a β-phase Grain Boundary Located at the Moving Front of a Cusp Similar to That in Fig. III.25A. The observation suggests that the groove advances by β-phase grain-boundary tearing. ANL Neg. No. 306-77-31.

It is not clear why a grain boundary is the preferential path for tearing. Apparently a β-phase grain boundary is weak and susceptible either to separation or to sliding. One possible explanation is that a crack in the oxide and α layers above the underlying grain boundary provides a perferential route for oxygen diffusion. Thus, stress and enhanced diffusion along the β-phase grain boundary can weaken the area and induce an intergranular tear.

According to this hypothesis, and intergranular tear will not be favored if the strain rate is rapid and less time is allowed for oxygen diffusion. Figure III.27 shows the cross section of a Zircaloy tube that was oxidized in steam for 48 s at 1154°C, without internal pressurization, and ruptured at this temperature in 0.25 s. During high-strain-rate deformation and rupture, a well-defined cusp similar to that in Fig. III.25 was not observed; i.e, the crack opening is rough and irregularly shaped. Similar observations have been reported by Bradhurst and Heuer^7 for Zircaloy-2 cladding rapidly deformed in steam at 1060°C.

Fig. III.27

Cross Section of a Zircaloy-4 Tube Oxidized in Steam for 48 s at 1154°C without Internal Pressure and Ruptured at This Temperature in 0.25 s. Irregular local deformation occurs at the OD surface as a result of the high strain rate. The pattern is in contrast to the smooth cusp that forms at low strain rates (e.g., Fig. III.25A). ANL Neg. No. 306-77-29.

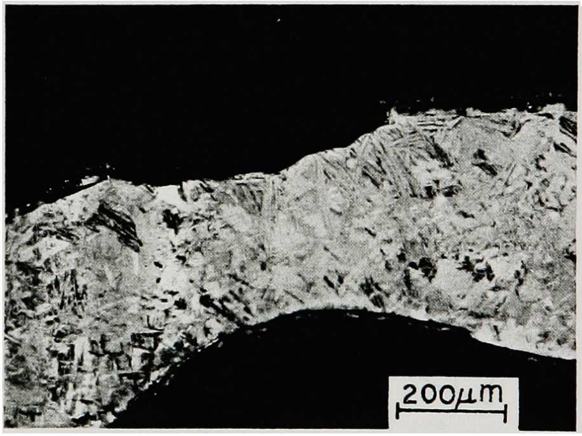

Figure III.28 is a scanning-electron micrograph of the fracture surface of the specimen described in Fig. III.27. The ZrO_2, stabilized α, and transformed β phases are clearly visible. The transformed β cross section is irregular, as is indicated by Fig. III.27. However, a detailed examination

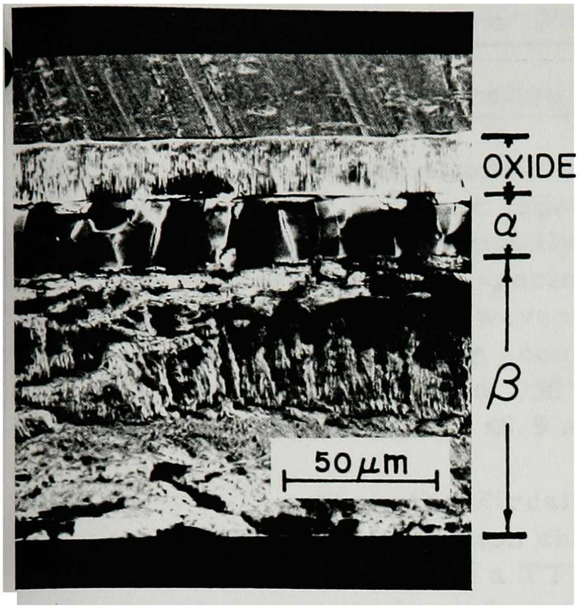

Fig. III.28

Scanning-electron Micrograph of the Fracture Surface of the Specimen Described in Fig. III.27. Intergranular fracture of the stabilized α phase and an irregular fracture surface of the β phase are evident. ANL Neg. No 306-77-27.

of the transformed β fracture surface is hampered because of the rapid oxidation of the β phase at high temperature. The stabilized α layer clearly shows an intergranular fracture at this temperature. Although no evidence was actually obtained for the fracture behavior of the α layer during transient deformation and rupture, intergranular failure is expected because of the brittle nature of the layer.

On the basis of the above observations and hypothesis, a deformation and rupture mechanism for Zircaloy cladding at temperatures ≳1000°C in steam is shown schematically in Fig. III.29. Actual micrographs that correspond to Figs. III.29E and III.29H are shown in Figs. III.25A and III.25B, respectively. Figure III.29H is the final microstructure expected after ID oxidation and the β →α' phase transformation during cooling.

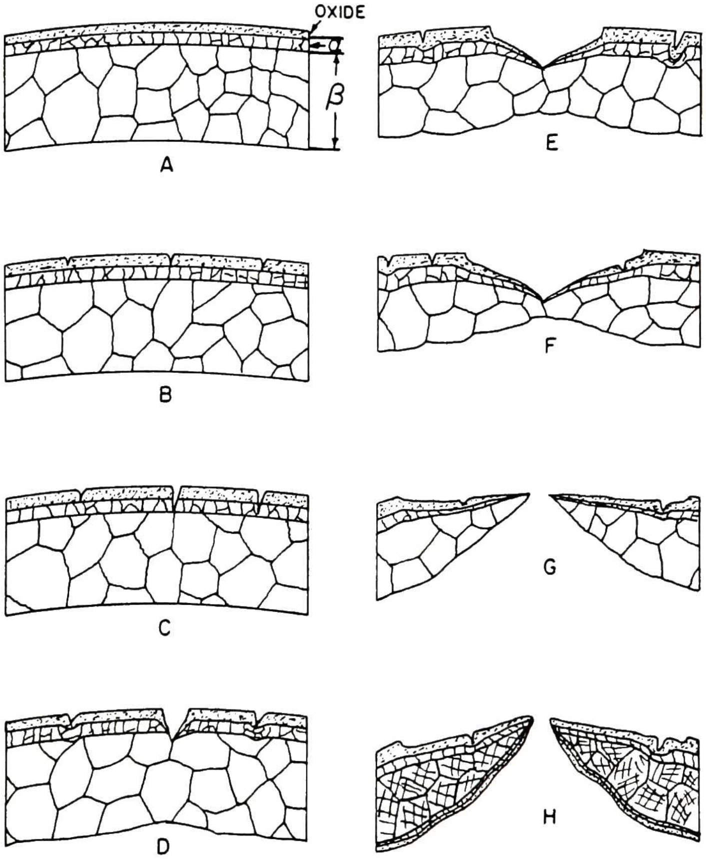

Fig. III.29

Schematic Representation of the Deformation and Rupture Sequence for Zircaloy Cladding in a Steam Environment at Temperatures ≳1000°C. Figure III.29H illustrates the cross section after cooling through the β → α' transformation. ANL Neg. No. 306-77-25.

D. Kinetics of the $\beta \rightarrow \alpha'$ Phase Transformation in Zircaloy-4

1. Transformation Kinetics of Zircaloy-4

Information on the kinetics of the isothermal $\beta \rightarrow \alpha'$ transformation in Zircaloy-2 has been reported by Östberg[8] in the form of a TTT diagram. The TTT diagram is usually determined form metallographic evaluations of the phases present in specimens quenched from different temperatures in the two-phase region. However, because the $\beta \rightarrow \alpha'$ transformation is so rapid, it is difficult to obtain an accurate boundary for the TTT diagram at temperatures between ~800 and 950°C; i.e., the nose of the C-curve in this range lies within a time scale of $\lesssim$0.5 s.

Since the Zircaloy-4 used in the present investigation is expected to exhibit transformation characteristics similar to those of Zircaloy-2, it is desirable to construct a TTT diagram for Zircaloy-4 based on a method that enables quantitative information to be obtained between ~800 and 950°C. Furthermore, a correlation of cooling rate with $\beta \rightarrow \alpha'$ transformation microstructure of Zircaloy-4 will be useful in the analysis of the mechanical properties of fuel cladding during the reflood stage after an LOCA.

A resistometric technique for studying the $\alpha \rightleftarrows \beta$ transformation was reported in Ref. 5. Figure III.30 shows resistivity curves for Zircaloy-4 containing 0.425 wt % oxygen that were obtained by heating and cooling the

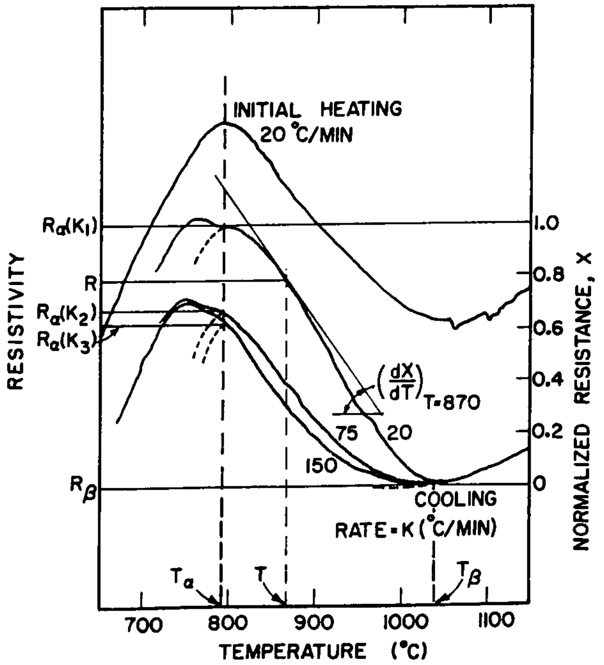

Fig. III.30

Resistivity-vs-Temperature Curves for a Zircaloy-4 Specimen with 0.425 wt % Oxygen Obtained at Constant Heating and Cooling Rates through the $\alpha + \beta$ Phase Region. The normalized resistance parameter X and its slope (dX/dT) at 870°C are also illustrated. ANL Neg. No. 306-77-21.

specimen through the $\alpha \rightleftarrows \beta$ transformation range. Since linear heating and cooling rates were used in the experiments, the specimen temperature T during cooling can be obtained from the relation

$$T = T_\beta - Kt, \tag{2}$$

where T_β is the temperature at the start of the $\beta \rightarrow \alpha$ transformation, K is the cooling rate, and t is the time. The resistivity R of the specimen during cooling at a constant rate can be expressed by

$$R = R^0_\beta\left[1 + \gamma_\beta(T - T_\beta)\right]f_\beta + R^0_\alpha\left[1 + \gamma_\alpha(T - T_\alpha)\right]f_\alpha, \tag{3}$$

where

f_α = fraction of α-phase material,

f_β = fraction of β-phase material,

T_α = temperature at termination of the $\beta \rightarrow \alpha$ transformation,

R^0_α = resistivity of material at T_α when the transformation occurs under a quasi-equilibrium slow-cooling condition,

R^0_β = resistivity at T_β,

γ_α = temperature coefficient of α resistivity, i.e., $\frac{d}{dT}\left[\frac{R}{R_0(T = 25°C)} - 1\right]$,

γ_β = temperature coefficient of β resistivity,

and

$$f_\alpha + f_\beta = 1. \tag{4}$$

From the pseudobinary Zircaloy-oxygen phase diagram, the absolute value of the quantities $T - T_\beta$ and $T - T_\alpha$ is $\lesssim$300°C for alloys with up to 0.6 wt % oxygen. For pure zirconium, the values of γ_α and γ_β are $\sim 3.5 \times 10^{-4}$ and 2.5×10^{-4}°C^{-1}, respectively, for temperatures $\gtrsim$800°C, and they decrease with an increase in oxygen content in the material.[9] Therefore, as an approximation we can write

$$R \simeq R^0_\beta f_\beta + R^0_\alpha f_\alpha, \tag{5}$$

and

$$f_\alpha \simeq X\frac{R_\alpha(K) - R^0_\beta}{R^0_\alpha - R^0_\beta}, \tag{6}$$

where

$$X \equiv \frac{R - R^0_\beta}{R_\alpha(K) - R^0_\beta} \tag{7}$$

and $R_\alpha(K)$ is the resistivity at T_α when the material is cooled at a rate K. In Eq. 7, X is the "normalized resistance change." The inflection points and small bumps at $T < T_\alpha$ in Fig. III.30 are caused by the second-phase precipitates.[6] After differentiation of Eqs. 2 and 6, we obtain

$$\dot{f}_\alpha \equiv \frac{df_\alpha}{dt} = -K\left(\frac{R_\alpha(K) - R^0_\beta}{R^0_\alpha - R^0_\beta}\right)\left(\frac{dX}{dT}\right). \tag{8}$$

Therefore, for a β → α transformation at a constant cooling rate K, the relative transformation rate at two temperatures T_1 and T_2 can be expressed by

$$\frac{\left.\dot{f}_\alpha\right)_{T_1}}{\left.\dot{f}_\alpha\right)_{T_2}} = \frac{\left(\frac{dX}{dT}\right)_{T_1.}}{\left(\frac{dX}{dT}\right)_{T_2}} \tag{9}$$

Figure III.31 compares a plot of $(dX/dT)^{-1}$ versus temperature for as-received Zircaloy-2 with portions of the TTT diagram obtained metallographically by Östberg.[8] On the basis of this comparison, a better extrapolation of the curve in the ~800-950°C range is possible. A similar plot of $(dX/dT)^{-1}$ versus temperature was obtained from resistivity measurements on as-received Zircaloy-4. The time scale, at a given temperature, for the TTT diagram of Zircaloy-4 was determined from

$$\frac{t_{\text{Zircaloy-4}}}{t_{\text{Zircaloy-2}}} = \frac{\left(\frac{dX}{dT}\right)^{-1}_{\text{Zircaloy-4}}}{\left(\frac{dX}{dT}\right)^{-1}_{\text{Zircaloy-2}}}, \tag{10}$$

where $t_{\text{Zircaloy-2}}$ was obtained from the extrapolated results in Fig. III.31. Figure III.32 shows the diagram for Zircaloy-4, together with several dashed cooling curves that will be discussed in connection with transformation microstructures.

2. Correlation of Cooling Rate with the Microstructure of Transformed α' Phase

The β → α' transformation microstructure is dependent on the cooling rate but, in general, can be correlated with a range of cooling rates.

Table III.1 shows a classification of Zircaloy-4 microstructures that correspond to the different cooling-rate curves on the TTT diagram in Fig. III.32, and the microstructures are shown in Figs. III.33-III.39. According to the TTT diagram, a martensitic structure, characterized by the long needle-shape features in Fig. III.33, will result when the material is cooled sufficiently fast to avoid the nose of the C-curve, i.e., an oil or water quench from a temperature in the β-phase region.

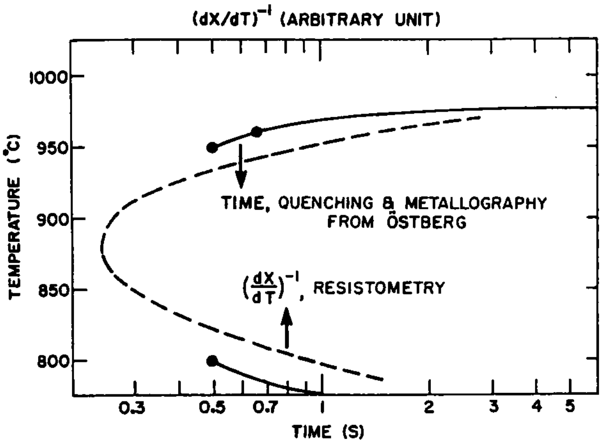

Fig. III.31

Comparison of the Time-Temperature-Transformation Curves from the Quenching and Metallographic Studies of Östberg[8] with Resistometric Data Obtained for Zircaloy-2. ANL Neg. No. 306-77-26.

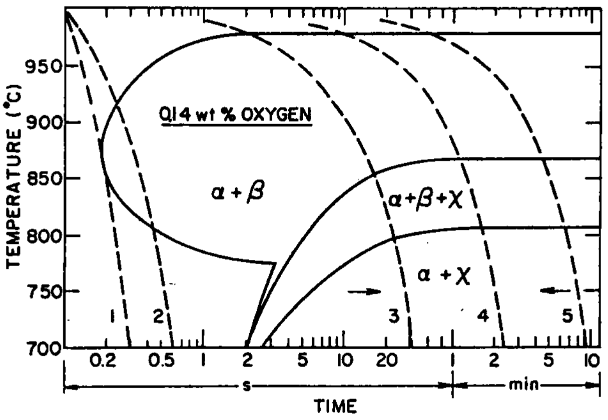

Fig. III.32

Time-Temperature-Transformation Diagram for As-received Zircaloy-4. The dashed curves 1-5 on the diagram correspond to cooling rates of ~1500, 600, 10, 2, and 0.5°C/s, respectively. ANL Neg. No. 306-77-22.

TABLE III.1. Correlation of Cooling Rate with the β → α' Transformation Structure of Zircaloy-4

Cooling[a] Rate K, °C/s	Microstructure Type
≳1500	Martensitic
1500-600	Intermediate Martensitic/Basketweave
600-10	Basketweave
10-2	Intermediate Basketweave/Parallel Plate
2-0.5	Parallel Plate
≲0.5	Lenticular
b	Rim α

[a] Cooling rate from a temperature of 1000°C.

[b] The rim-α structure forms only for a limited cooling rate, e.g., ~10°C/s from 1000°C.

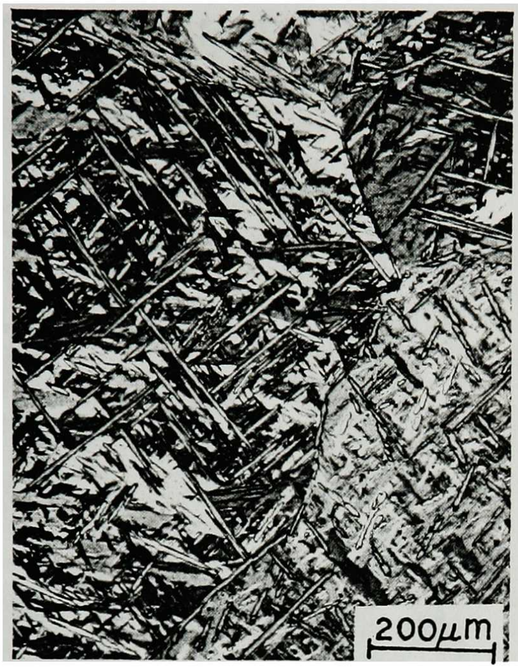

Fig. III.33

Martensitic Structure of As-received Zircaloy-4 after Cooling through the $\beta \rightarrow \alpha'$ Transformation at ~10,000°C/s (Oil quench) from 1000°C. Etched. Polarized light. ANL Neg. No. 306-77-34.

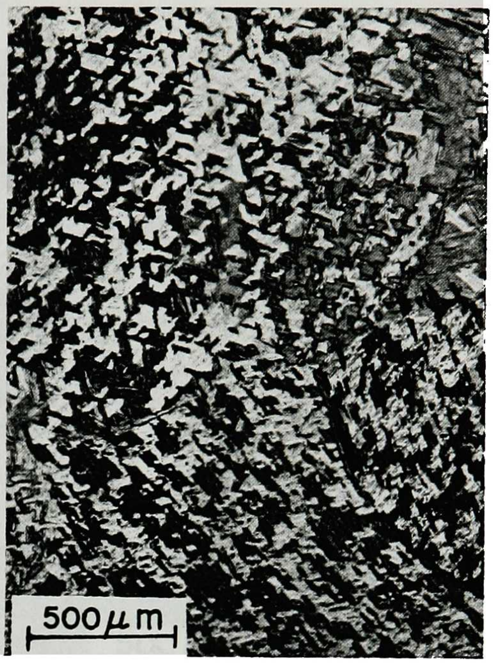

Fig. III.34

Intermediate Martensitic/Basketweave Structure of As-received Zircaloy-4 after Cooling through the $\beta \rightarrow \alpha'$ Transformation at ~1000°C/s from 1000°C. Etched. Polarized light. ANL Neg. No. 306-77-33.

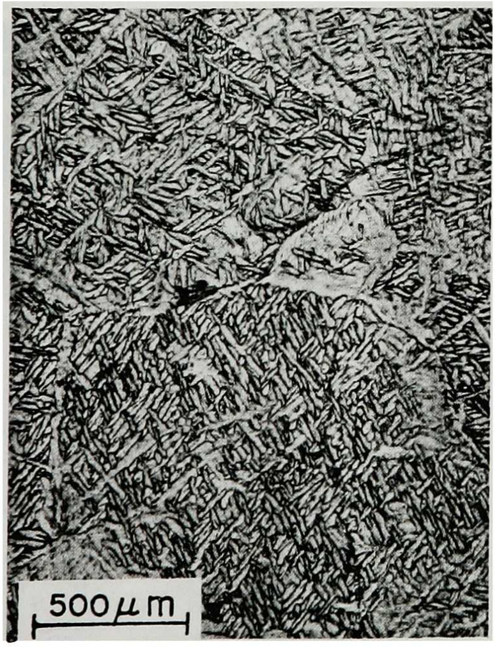

Fig. III.35

Basketweave Structure of As-received Zircaloy-4 after Cooling through the $\beta \rightarrow \alpha'$ Transformation at ~500°C/s from 1000°C. Etched. Polarized light. ANL Neg. No. 306-77-36.

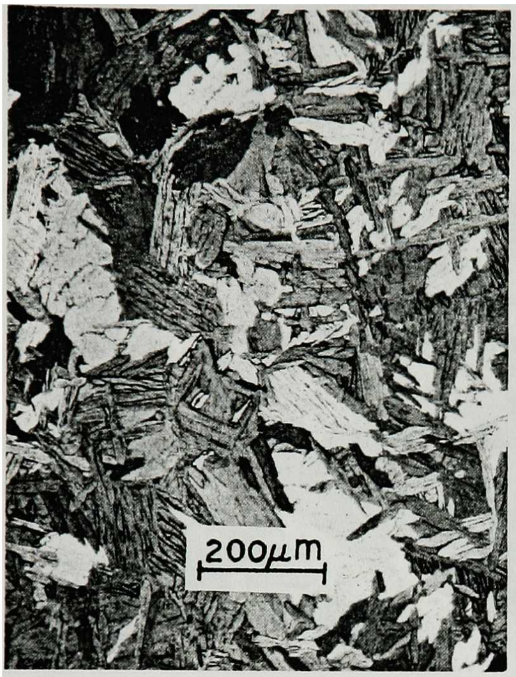

Fig. III.36

Intermediate Basketweave/Parallel-plate Structure of As-received Zircaloy-4 after Cooling through the β → α' Transformation at 3.3°C/s from 1000°C. Etched and anodized. Polarized light. ANL Neg. No. 306-77-32.

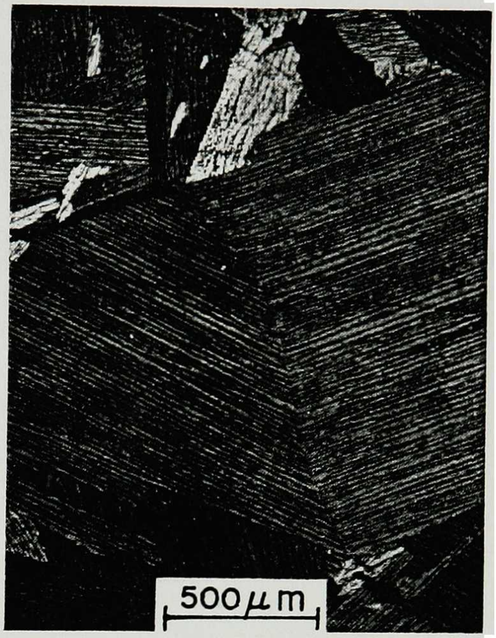

Fig. III.37

Parallel-plate Structure of As-received Zircaloy-4 after Cooling through the β → α' Transformation at 1.8°C/s from 1250°C. Etched. Polarized light. ANL Neg. No. 306-77-35.

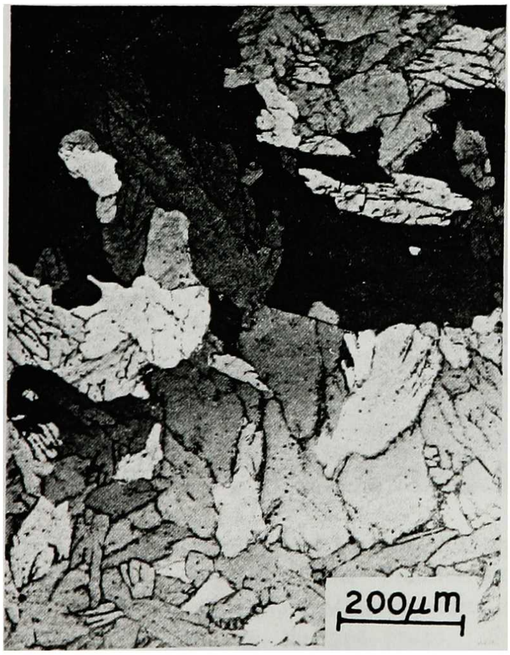

Fig. III.38

Microstructure of As-received Zircaloy-4 after Cooling through β → α' Transformation at 0.1°C/s from 1000°C. Note the large elongated grains. Etched and anodized. Polarized light. ANL Neg. No. 306-77-38.

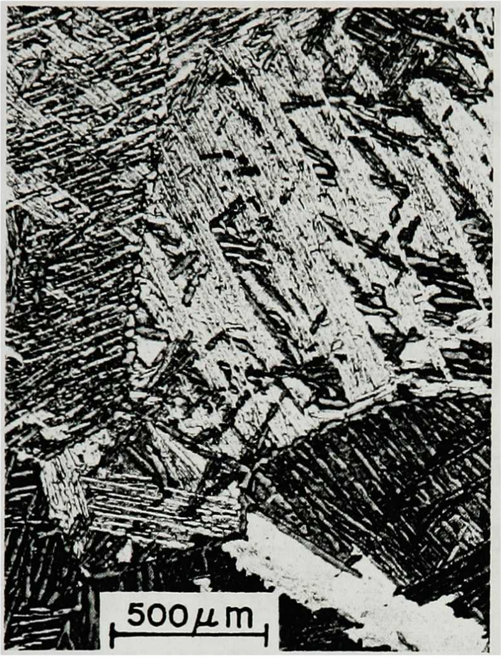

Fig. III.39

Rim-α Structure at the Previous β-grain Boundaries of As-received Zircaloy-4 Formed during Cooling through the β → α' Transformation. Etched. Polarized light. ANL Neg. No. 306-77-30.

When a specimen is oxidized, homogenized, and oil- or water-quenched, the martensitic structure is obtained only for oxygen concentrations ≲0.6 wt %; at higher oxygen contents, an intermediate basketweave/parallel-plate structure is formed. The martensitic and intermediate structures for specimens with 0.446 and 1.15 wt % oxygen are shown in Fig. III.40. It is unclear why the martensitic structure is not observed for specimens with high oxygen contents. One possibility is that the interstitial oxygen atoms may decrease the martensite start M_s temperature to below room temperature.

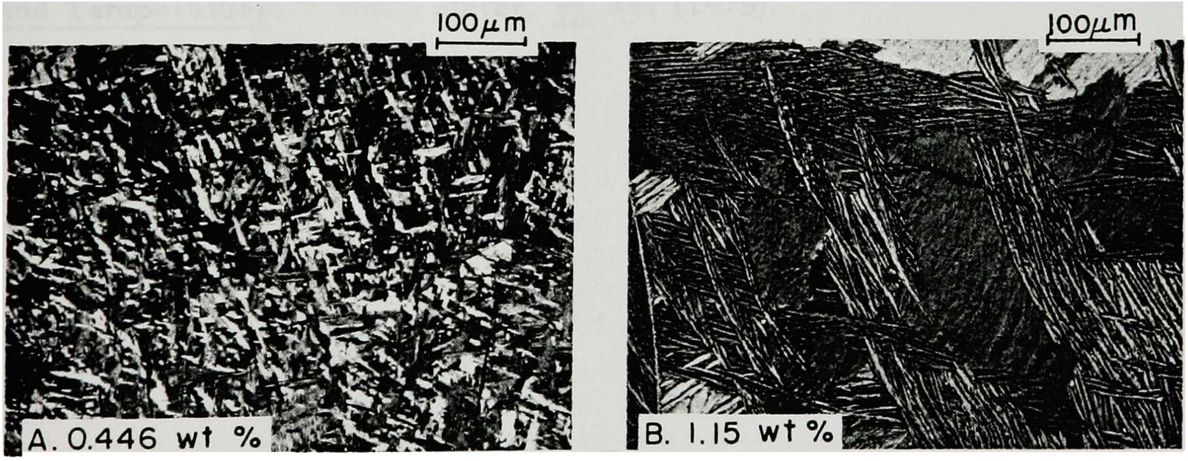

Fig. III.40. Micrographs of Zircaloy-4/Oxygen Alloys with 0.446 and 1.15 wt % Oxygen after Cooling through the β → α' Transformation (Oil quench) That Illustrate the Martensitic and Parallel-plate Microstructures, Respectively. Etched and anodized. Polarized light. ANL Neg. No. 306-77-40.

References

1. Light-water-reactor Safety Research Program: Quarterly Progress Report, July-September 1976, Sec. III, "Mechanical Properties of Zircaloy Containing Oxygen," ANL-76-121.
2. Light-water-reactor Safety Research Program: Quarterly Progress Report, January-March 1976, Sec. III, "Mechanical Properties of Zircaloy Containing Oxygen," ANL-76-49.
3. R. H. Meservey and R. Herzel, Brittle Behavior of Zircaloy in an Emergency Core Cooling Environment, IN-1389, Idaho Nuclear Corporation (Sept 1970).
4. G. J. Scatena, Fuel Cladding Embrittlement During a Loss-of-coolant Accident, NEDO-10674, General Electric Company, San Jose, CA (Oct 1972).
5. Light-water-reactor Safety Research Program: Quarterly Progress Report, April-June 1975, Sec. III, "Mechanical Properties of Zircaloy Containing Oxygen," ANL-75-58.
6. Light-water-reactor Safety Research Program: Quarterly Progress Report, April-June 1976, Sec. III,"Mechanical Properties of Zircaloy Containing Oxygen," ANL-76-87.
7. D. H. Bradhurst and P. M. Heuer, The Effect of Deformation on the High Temperature Steam Oxidation of Zircaloy-2, J. Nucl. Mater. 55, 311 (1975).
8. G. Östberg, Metallographic Study of Isothermal Transformation of Beta Phase in Zircaloy-2, Jernkontorets Ann. 145, 119 (1963).
9. G. Hörz, M. Hammel, and H. Kanbach, Electrical Resistivity of β-Zirconium-Oxygen Solid Solutions as a Function of Oxygen Concentration and Temperature, J. Nucl. Mater. 55, 291 (1975).

IV. STEAM-EXPLOSION STUDIES

Responsible Section Manager:
R. E. Henry, RAS

A. Vapor Explosions at Elevated Temperatures (R. E. Henry and L. M. McUmber, RAS)

Large-scale vapor explosions have been demonstrated to occur in a free-contacting mode when the interface temperature, upon contact between two liquid masses, equals or exceeds the temperature required for spontaneous nucleation.[1,2] A model has been proposed that relates this spontaneous nucleation criterion to the thermal-boundary-layer development within the cold liquid. This resulting model then describes the energy-transfer process that results in explosive vapor formation.[3] Such considerations also demonstrate that when the interface temperature upon contact approaches the thermodynamic critical point of the liquid, the nucleation rate becomes so overwhelming that all intimate liquid-liquid contacts are terminated as a result of bubble coalescence on a 100-Å-size (1 x 10^{-8} m) scale in microsecond intervals or less.

As a result, all such systems would then remain in stable film boiling, and the vaporization process would take place over several seconds. This is of considerable importance when considering the possible configurations following a postulated core meltdown in a light-water reactor, since the interface temperatures upon contact between fuel and water are at least three times the critical temperature of water and the interface temperature between steel and water, assuming no chemical interaction between the two, also falls into the same category.

To test whether such mechanisms are indeed relevant for contact temperatures above the critical point, the apparatus shown in Fig. IV.1 was fabricated and instrumented. In this apparatus, the high-temperature liquid, mineral oil, was contained in the reaction vessel and this vessel was instrumented with piezoelectric pressure and force transducers as well as thermocouples to measure the bulk temperature. An argon-gas bubbler was also included to ensure that no significant stratification occurred within the oil. The cold liquid, Freon-22, was contained in a suspended cup directly over the reaction vessel.

This entire system was then encompassed in an outer shroud of sufficient volume so that vaporization from film boiling would not provide significant increases in the ambient pressure. This outer shroud was also maintained under an inert environment so that the oil could be heated to high temperatures without undergoing any chemical change.

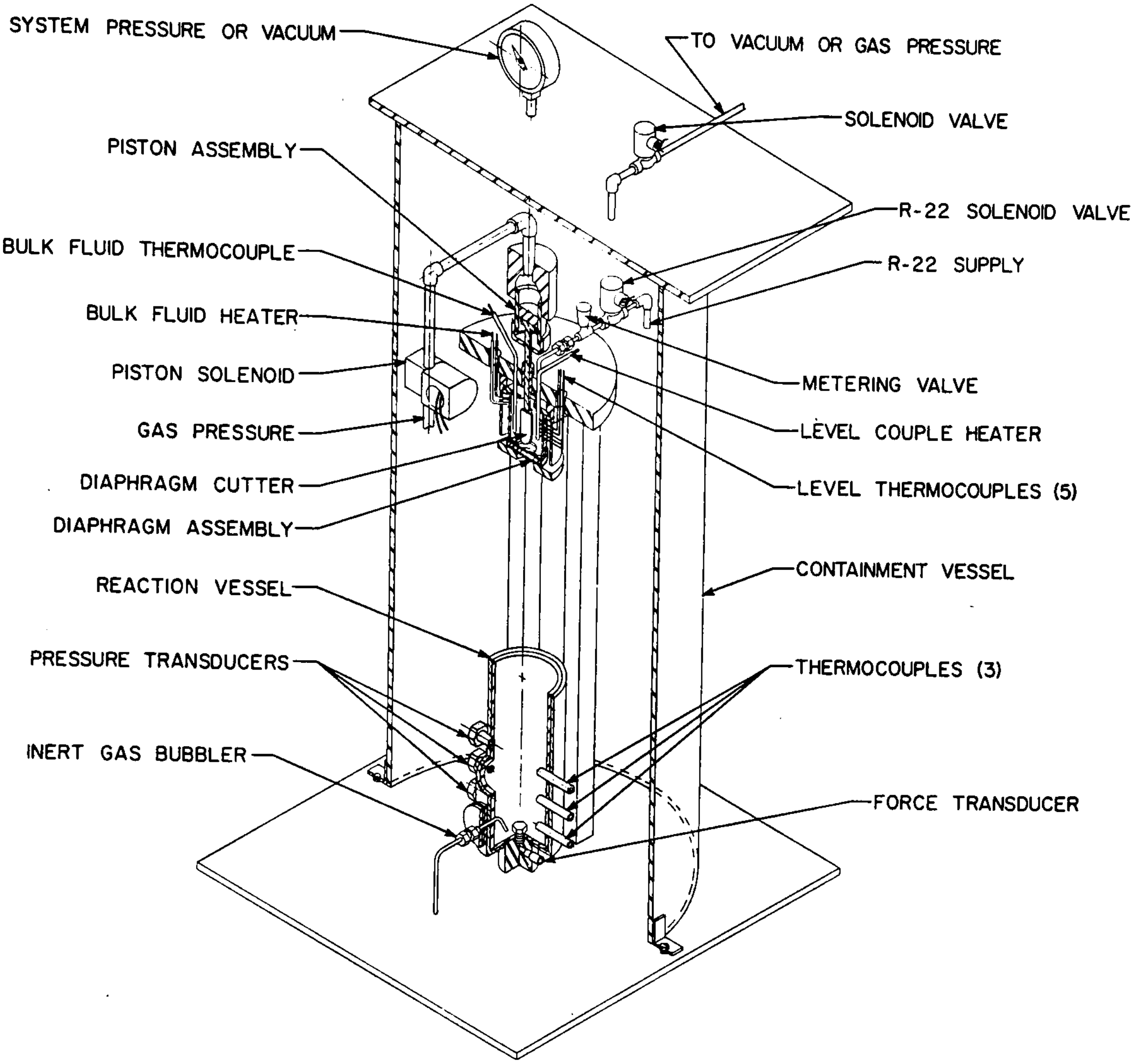
SYSTEM PRESSURE OR VACUUM
TO VACUUM OR GAS PRESSURE
SOLENOID VALVE
PISTON ASSEMBLY
R-22 SOLENOID VALVE
BULK FLUID THERMOCOUPLE
R-22 SUPPLY
BULK FLUID HEATER
PISTON SOLENOID
METERING VALVE
GAS PRESSURE
LEVEL COUPLE HEATER
DIAPHRAGM CUTTER
LEVEL THERMOCOUPLES (5)
DIAPHRAGM ASSEMBLY
CONTAINMENT VESSEL
REACTION VESSEL
PRESSURE TRANSDUCERS
THERMOCOUPLES (3)
INERT GAS BUBBLER
FORCE TRANSDUCER

Fig. IV.1. Large-scale Vapor Explosions in a Contained Volume. ANL Neg. No. 900-77-69.

The experiments were conducted by filling the vessel full of oil and heating it to the required temperature level. At this point, the Freon was added to the cup at local saturated conditions, and when this filling process was complete, the diaphragm-cutter assembly was actuated and the Freon was allowed to fall directly into the mineral oil.

Ambient pressures slightly above atmospheric (0.10 MPa) have been demonstrated to terminate the explosive character of this type system. An ambient pressure of 0.05 MPa was therefore chosen since the total rise in the ambient pressure after vaporizing all the Freon only amounts to an overall increase of 0.03 MPa. Therefore, the ambient pressure before, and the equilibrium pressure after, these experiments were always less than 0.10 MPa. Consequently, the increase in ambient pressure would not have been sufficient to prevent the onset of explosive interaction.

The principal variable in these experiments was initial temperature of the oil, and it was varied in the preliminary experiments discussed herein, from 180 to 240°C. At about 205°C, the interface temperature upon contact between the Freon and the oil as evaluated by

$$T_i = \frac{T_H + \sqrt{\dfrac{k_c \rho_c c_c}{k_H \rho_H c_H}}\, T_c}{1 + \sqrt{\dfrac{k_c \rho_c c_c}{k_H \rho_H c_H}}} \tag{1}$$

was equal to the thermodynamic critical point of Freon-22, which is 96°C. (In Eq. 1, c = specific heat, k = thermal conductivity, T = temperature, and ρ = density, and the subscripts c, H, and i refer to cold, hot, and interface, respectively.)

The results of these experiments are illustrated in Fig. IV.2, which shows the maximum measured interaction pressures as a function of the initial oil temperature. It is evident that very energetic interactions were observed in the range of 180-205°C oil temperature and that, for temperatures above this value, no explosive interactions were observed.

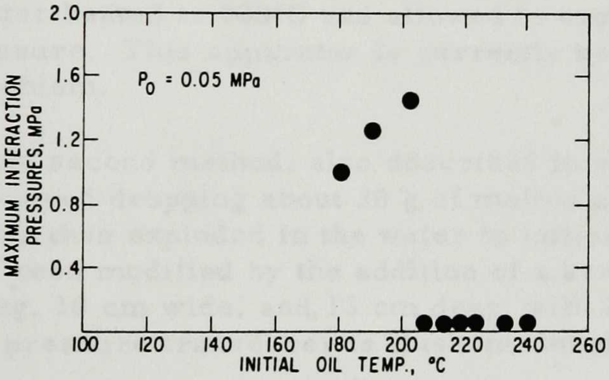

Fig. IV.2

High-temperature Experimental Data on Freon-22 and Mineral Oil

These preliminary results in a well-wetted system, with no significant potential for chemical interaction, provide considerable insight into the type of nucleation process one might expect between fuel and water. In addition, they provide an interesting and needed insight into the nucleation process itself.

B. Combined Physical-Chemical Explosions (D. R. Armstrong and N. E. Parker, RAS)

The study of combined physical-chemical explosions in an aluminum/water system has been progressing on the basis of developing methods of producing combined explosions using small quantities of at least one of the interacting materials as a means of limiting the destructive potential of the experiments. Two ways of producing small-scale physical explosions have been developed and were described in ANL-76-87.

The first method inserts a glass sphere containing water into a pool of molten aluminum in a cylindrical container. The aluminum is then compressed by the impact of a falling weight, and the water is dispersed by an exploding wire. The original system used a length of Type 304 stainless steel pipe as the crucible for containing the molten aluminum. With the molten aluminum directly in contact with the crucible, the stainless steel dissolution is so rapid that the average lifetime of a crucible is less than 1 hr. Since this is about the heat-up time for an experiment, the success rate for these experiments is less than 50%. The first attempt at a fix will be the installation of quartz liners in the crucible.

While waiting for the delivery of the liners, a run was made using the original equipment. One gram of water at 20°C inserted into 900 g of aluminum at 880°C exploded and transmitted 250 J of energy to the impacting weight. This is 8.3% of the maximum energy that could be absorbed by the impact weight in this apparatus. For this run, a rough indication of the energy in the aluminum dispersed by the explosion was obtained by measuring the expansion velocity of the cloud of aluminum particles released when the impact weight cleared the end of the crucible. The mass of aluminum dispersed was estimated from the positions of the impact weight at the time of the explosion and when it reimpacted on the aluminum. The energy in the dispersed aluminum was 1125 J, and the total measured output energy in this experiment was 1375 J, or 25% of the theoretical maximum energy that could be obtained from 1 g of water heated to 880°C and allowed to expand isothermally to 1 atm final pressure. This apparatus is currently being modified to eliminate a major problem.

The second method, also described in earlier reports (ANL-76-87 and -121), involved dropping about 30 g of molten aluminum into a tank of water. A wire was then exploded in the water to initiate the explosion. This experiment has been modified by the addition of a heavy-wall stainless steel tank, 15 cm long, 10 cm wide, and 13 cm deep, with 2.5-cm-thick Lucite side windows. A pressure transducer is flush-mounted in one end wall of the tank.

Two runs have been made with this apparatus. In both cases 28 g of molten aluminum were dropped into 1.3 ℓ of water at 28°C. A time delay was set so that the aluminum was pooled on the bottom of the tank at the time of the initiating wire explosion. The two events were similar in appearance. Within a single frame of the high-speed motion pictures (5000 frames/s), the entire aluminum mass had started to expand. This corresponds to a minimum propagation velocity of 200 m/s.

Film measurements of the water velocity during the first millisecond of the event gave an energy estimate of 18 J and a minimum peak pressure estimate of 0.5 MPa. This was also the minimum estimated peak pressure from the force-transducer record. However, both of these pressure measurements had response times of about 1 ms and thus would integrate over that time period and average out a pressure pulse of shorter duration.

The reason for this emphasis on secondary pressure measurements was that no clear indication of a pressure resulting from the aluminum-water interaction was shown on the pressure-transducer record. This could have been due to either of two limitations on the pressure measurement. First, the minimum amplitude that could be resolved was 2 MPa, so that any pressure less than this would be missed. Second, the experimental setup placed the aluminum between the exploding wire and the transducer, so that pressures from the interaction and the wire could reach the transducer simultaneously. The recording equipment was limited to an 80-kHz response, which could not resolve the details of the wire pressure alone and certainly would miss the addition of the interaction pressure.

Since all the data from this experiment are simply a measure of the instrumentation limits, a number of modifications are being made. A second pressure transducer will be installed in the opposite end wall of the tank, and more sensitive transducers will be used. The pressure-recording system is being modified to provide 250-kHz response, and equipment is being assembled to allow photography at 200,000 frames/s.

References

1. R. E. Henry et al., "Large Scale Vapor Explosions," Proc. Fast Reactor Safety Meeting, Beverly Hills, CA, CONF-740401, P2, 922 (Apr 1974)
2. R. E. Henry, H. K. Fauske, and L. M. McUmber, "Vapor Explosions in Subcooled Freon," Proc. Third Specialists Meeting on Sodium/Fuel Interactions in Fast Reactors, PNCN 251 76-12, Tokyo, Japan, 231 (Mar 1976).
3. R. E. Henry and H. K. Fauske, "Energetics of Vapor Explosions," ASME Paper No. 75-HT-66, National Heat Transfer Conf., San Francisco, CA (1975).